N°d'ordre NNT : xxx

**THESE de DOCTORAT DE L'UNIVERSITE DE LYON**
opérée au sein de
**l'Université Claude Bernard Lyon 1**

**Ecole Doctorale** N° ED 205
**Ecole Doctorale Interdisciplinaire Sciences-Santé (EDISS)**

**Spécialité de doctorat** : Recherche clinique et innovation technologique
**Discipline**: Instrumentation et physique expérimentale

Soutenue publiquement le 18/12/2020, par :

**Hamza RAKI**

---

# MEMS-based reconfigurable endoluminal MRI coils

---

Devant le jury composé de :

| | |
|---|---|
| **FERRIGNO, Rosaria**<br>Professeure, Université Lyon 1, Lyon | **Présidente** |
| **AMADON, Alexis**<br>Ingénieur de recherche, CEA-Saclay, Gif-Sur-Yvette | **Rapporteur** |
| **POIRIER-QUINOT, Marie**<br>Professeure, Université Paris-Saclay, Orsay | **Rapporteure** |
| **SAINT-JALMES, Hervé**<br>Professeure des Universités, Praticien Hospitalier, Université Rennes 1, Rennes | **Rapporteur** |
| **PERRIER, Anne-Laure**<br>Maitre de conférences, Université Savoie Mont Blanc, Bourget-Du-Lac | **Examinatrice** |
| **BEUF, Olivier**<br>Directeur de recherche, CNRS, Lyon | **Directeur de thèse** |
| **TSE VE KOON, Kevin**<br>Maitre de conférences, Université Lyon 1, Lyon | **Co-directeur** |
| **ROBB, Fraser**<br>Chief Technology Leader for the MRI coils Division, GE Healthcare, Aurora (USA) | **Examinateur** |
| **Souchay, Henri**<br>Clinical Research Manager for France, GE Healthcare, Buc | **Invité** |

# Université Claude Bernard – LYON 1

| | |
|---|---|
| Administrateur provisoire de l'Université | M. Frédéric FLEURY |
| Président du Conseil Académique | M. Hamda BEN HADID |
| Vice-Président du Conseil d'Administration | M. Didier REVEL |
| Vice-Président du Conseil des Etudes et de la Vie Universitaire | M. Philippe CHEVALLIER |
| Vice-Président de la Commission de Recherche | M. Jean-François MORNEX |
| Directeur Général des Services | M. Pierre ROLLAND |

## COMPOSANTES SANTE

| | |
|---|---|
| Département de Formation et Centre de Recherche en Biologie Humaine | Directrice : Mme Anne-Marie SCHOTT |
| Faculté d'Odontologie | Doyenne : Mme Dominique SEUX |
| Faculté de Médecine et Maïeutique Lyon Sud - Charles Mérieux | Doyenne : Mme Carole BURILLON |
| Faculté de Médecine Lyon-Est | Doyen : M. Gilles RODE |
| Institut des Sciences et Techniques de la Réadaptation (ISTR) | Directeur : M. Xavier PERROT |
| Institut des Sciences Pharmaceutiques et Biologiques (ISBP) | Directrice : Mme Christine VINCIGUERRA |

## COMPOSANTES & DEPARTEMENTS DE SCIENCES & TECHNOLOGIE

| | |
|---|---|
| Département Génie Electrique et des Procédés (GEP) | Directrice : Mme Rosaria FERRIGNO |
| Département Informatique | Directeur : M. Behzad SHARIAT |
| Département Mécanique | Directeur M. Marc BUFFAT |
| Ecole Supérieure de Chimie, Physique, Electronique (CPE Lyon) | Directeur : Gérard PIGNAULT |
| Institut de Science Financière et d'Assurances (ISFA) | Directeur : M. Nicolas LEBOISNE |
| Institut National du Professorat et de l'Education | Administrateur Provisoire : M. Pierre CHAREYRON |
| Institut Universitaire de Technologie de Lyon 1 | Directeur : M. Christophe VITON |
| Observatoire de Lyon | Directrice : Mme Isabelle DANIEL |
| Polytechnique Lyon | Directeur : Emmanuel PERRIN |
| UFR Biosciences | Administratrice provisoire : Mme Kathrin GIESELER |
| UFR des Sciences et Techniques des Activités Physiques et Sportives (STAPS) | Directeur : M. Yannick VANPOULLE |
| UFR Faculté des Sciences | Directeur : M. Bruno ANDRIOLETTI |

# Thanks

*Thanks to my God for helping me to achieve this thesis.*

*Thanks for all Jury members for accepting to evaluate this thesis work as rapporteur or examiner and for giving time for the evaluation of this thesis manuscript.*

*Thanks for the follow-up of my supervisors (CREATIS & GE Healthcare): thesis following, periodic meeting, important advices, careful corrections,*

*A special thanks to my thesis director Olivier Beuf for the excellent thesis supervision and direction at all levels*

*A special Thanks to Kevin Tse Ve Koon who played a role very important in this thesis as a co-supervisor*

*Many thanks to Olivier & Kevin in particular for the work at nights, in the Edouard Heriot hospital of Lyon, often from 7 PM until 2 am …*

*A special thanks to Robb Fraser (GE Healthcare) for all helps in particular about MEMS technology and GE equipment, documentations, contacts, …*

*A special thanks to Henri Souchay (GE Healthcare) for all helps in the thesis, for Making me in contact with specialists of GE, advices,*

*Thanks to my parents and family members (my grandparents, my mother, my father, my sister and my wife, brothers, …) whose encourage and support me during the period of thesis.*

*Thanks to all my friends of laboratory (PhD students & permanents) for the excellent moments and time during this thesis.*

# ملخص

سرطان القولون والمستقيم هو ثالث أكثر أنواع السرطانات المميتة. مع التشخيص المبكر ، يكون معدل البقاء على قيد الحياة حوالي 90٪. التصوير بالرنين المغناطيسي الداخلي يعتبر حلاً جذابًا لتحقيق دقة عالية في المناطق العميقة والرقيقة في جسم الإنسان مثل طبقات جدار القولون. يمكن أن يسمح بتحليل جدار القولون وتحديد خصائصه لتقييم مرحلة سرطان القولون والمستقيم بالاشتراك مع التنظير الداخلي البصري. هدف الأطروحة هو استخدام تقنية المامس لتطوير جهاز خاص لجدار القولون. في هذا السياق ، تم تنفيذ التطورات الآلية والمحاكاة الكهرومغناطيسية. وفقًا لذلك ، ركزنا على MR المامس كعناصر فصل نشطة على أداء الملف وجودة الصورة. في المحور الأول للأطروحة على جدوى وتحسين استخدام الواقع ، يعد إلغاء تنشيط الملف داخل اللمعة أثناء إرسال التردد اللاسلكي أمرًا إلزاميًا لتجنب مشكلات سلامة المريض يعتمدان على MEMS (حرق الترددات اللاسلكية) وتدهور جودة الصورة. لهذا الغرض ، تم بناء نموذجين أوليين لملف مفاتيح في تكوينات تسلسلية ومتوازية ، وتم تمييزهما (على مقاعد تجريبية وفي ظروف التصوير في نظام التصوير الثنائي التقليدية. تظهر النتائج على مقاعد البدلاء وعلى PIN ومقارنته بدائرة (T بالرنين المغناطيسي السريري 1.5 كانت MEMS الصور أن الخصائص (عامل الجودة ، وكفاءة الفصل والسرعة ، ونسبة الإشارة إلى الضوضاء) لملفات وحتى أفضل من ملف المصفوفة الخارجية التجارية في منطقة الاهتمام ، PIN قابلة للمقارنة مع ملف الصمام الثنائي النشط للملفات داخل اللمعة. يتعلق المحور الثاني من الأطروحة بالملاحة MEMS وبالتالي التحقق من كفاءة فصل إلى اختلافات B0 المطلوبة للملف داخل القولون حيث تؤدي اتجاهات حلقة الملف فيما يتعلق بالمجال المغناطيسي الرئيسي MEMS كبيرة في حساسية الملف من حيث الكثافة وتوحيد التوزيع الذي يغير جودة الصورة. الهدف هو استخدام مفاتيح لتعديل تصميم هندسة الملف وفقًا لاتجاه الملف. لهذا الغرض ، تم تحديد أشكال هندسية مختلفة لحلقة الملف اللولبية ثم تم تقييم توزيعات حساسية الصورة (الشدة والانتظام) لتوجهات .FEKO ومحاكاتها على البرنامج الكهرومغناطيسي مختلفة. نتيجة لذلك ، تم تحديد الأشكال الهندسية التكميلية ليتم دمجها فيما بينها من أجل تصميم واقتراح ملف التصوير القابل لإعادة التشكيل مع تقليل التبعية بين حساسية الملف وتوجيهه فيما يتعلق MEMS بالرنين المغناطيسي القائم على لتصميم ملفات داخل اللمعة أحادية القناة للتصوير بالرنين MEMS في الختام ، أظهرنا اهتمام تقنية التبديل .B0 Endoluminal ملفات) swiM RE-Coils :مخصصة لفحوصات القولون البشري و / أو المستقيم RF المغناطيسي MEMS) قابلة لإعادة التشكيل باستخدام مفاتيح).

**الكلمات الأساسية**: لفائف التصوير بالرنين المغناطيسي الداخلية ، الترددات الراديوية ، حساسية الملف ، المحاكاة الكهرومغناطيسية ، الهندسة القابلة لإعادة التشكيل

# Abstract

Colorectal cancer is the thirdest most mortal cancer. With an early diagnosis, the survival rate is about 90%. Endoluminal magnetic resonance imaging is an attractive solution to achieve locally high spatial resolution in deep and thin regions in the human body such as colon wall layers. It could allow colon wall analysis and characterization to assess the colorectal cancer stage in combination with optical endoscopy. The global goal of the thesis is to investigate the use of MEMS (Micro Electro Mechanical System) switch technology to design one-channel endoluminal MRI RF coils for MR image analysis of colon wall. In this context, instrumental developments and electromagnetic simulations were carried out. Accordingly, we focused for the first axis of the thesis on the feasibility and improvements of using MEMS as active decoupling elements on coil-performances and image quality. Indeed, deactivating the endoluminal coil during the RF transmission is mandatory to avoid patient safety issues (RF burn) and image quality degradation. For this purpose, two MEMS coil prototypes based on switches in serial and parallel configurations were built, characterized (on experimental benches and in imaging conditions in a clinical 1.5 T MRI system) and compared to conventional PIN diode circuit. Results on bench and on images show that characteristics (quality factor, decoupling efficiency and speed, and Signal-to-Noise Ratio) of MEMS coils were comparable to the PIN diode coil and even better than a commercial external array coil in the region of interest, thus validating the efficiency of MEMS active decoupling for endoluminal coils. The second axis of the thesis is related to the required coil navigation within the colon where coil-loop orientations with respect to the main magnetic field $B_0$ lead to significant coil-sensitivity variations in terms of intensity and distribution uniformity altering the image quality. The objective is to use MEMS switches to modify the coil-geometry design according to the coil-orientation. For this purpose, different endoluminal coil-loop geometries were defined and simulated on electromagnetic software FEKO. Image sensitivity distributions (intensities and uniformities) were then evaluated for different orientations. As a result, complementary geometries have been identified to be combined between them in order to design and propose a reconfigurable MEMS-based MRI endoluminal coil with a reduced dependency between coil-sensitivity and its orientation with respect to $B_0$. In conclusion, we demonstrated the interest of MEMS switch technology for designing one-channel MRI RF endoluminal coils dedicated to the human colon and/or rectum examinations: swiM RE-Coils (Reconfigurable Endoluminal Coils using switches MEMS).

**Key words:** MRI endoluminal coils, radiofrequency, MEMS switches, active decoupling, coil-orientation, coil-sensitivity, electromagnetic simulation, reconfigurable geometry.

# Résumé

Le cancer colorectal est le troisième cancer le plus mortel. Avec un diagnostic précoce, le taux de survie est pourtant d'environ 90%. L'imagerie par résonance magnétique endoluminale (IRM basé sur l'utilisation des capteurs endoluminaux ou encore internes) est une solution attractive permettant de fournir une haute résolution spatiale locale notamment pour imager les couches profondes et fines du côlon humain. Elle pourrait permettre l'analyse et la caractérisation de la paroi du colon pour évaluer le stade du cancer colorectal en combinaison avec l'endoscopie optique. L'objectif général de cette thèse est d'explorer l'exploitation de la technologie de micro-commutateurs (MEMS) afin de concevoir des capteurs endoluminaux radiofréquences utilisés en IRM clinique pour l'analyse de la paroi du côlon. Dans ce contexte, des développements instrumentaux et des simulations électromagnétiques ont été effectués. Le premier axe est consacré à l'évaluation des MEMS en tant que dispositif de découplage actif et l'impact sur les performances des capteurs et la qualité de l'image RMN. En effet, la désactivation du capteur endoluminal lors de la transmission RF est nécessaire pour éviter la dégradation de la qualité de l'image et les problèmes de sécurité pour les patients liés à la concentration RF locale. A cet effet, deux prototypes de capteurs MEMS fondés sur deux configurations de découplage en série et parallèle ont été fabriqués, caractérisés (sur des bancs de tests expérimentaux et sur un imageur clinique de 1.5 T) et comparés au circuit conventionnel utilisant une diode PIN. Les résultats montrent que les caractéristiques (facteur de qualité, efficacité et vitesse de découplage et rapport signal sur bruit) des capteurs MEMS sont comparables au capteur de référence et toujours supérieur à une antenne externe commercial en réseau dans la région d'intérêt, validant ainsi l'efficacité du découplage actif MEMS pour les capteurs endoluminaux. Le deuxième axe de cette thèse est lié à la nécessité de prévoir de considérer la navigation endoluminale du capteur le long du côlon. Cette navigation induit des variations d'orientation du capteur par rapport au champ magnétique statique $B_0$ entrainant des variations importantes de sensibilité de détection en intensité et en distribution du signal altérant significativement la qualité de l'image. L'objectif est d'utiliser les micro-commutateurs MEMS pour modifier la géométrie du capteur en fonction de son orientation. A cet effet, différentes géométries de boucles de capteurs endoluminaux ont été définies et simulées à l'aide du logiciel de simulation électromagnétique FEKO. Les distributions de sensibilité des images (intensités et uniformités) ont été ensuite évaluées pour différentes orientations. En termes de résultats, des géométries complémentaires ont été identifiées et combinées entre elles dans le but de concevoir et proposer un capteur endoluminal reconfigurable fondé sur la technologie MEMS et ayant une dépendance réduite entre la sensibilité du capteur et son orientation par rapport $B_0$. En conclusion, nous avons démontré le principe de l'intérêt de l'utilisation de la technologie de commutateurs MEMS pour concevoir des capteurs endoluminaux dédiées aux examens du côlon et/ou rectum humain : swiM RE-Coils (capteurs endoluminaux reconfigurables par des micro-commutateurs).

**Mots clés :** capteurs endoluminaux IRM, radiofréquence, micro-commutateurs, découplage actif, orientation du capteur, sensibilité, simulation électromagnétique, géométrie reconfigurable.

# Contents

# Abbreviations

| | |
|---|---|
| $\mathbf{B_0}$ | Static magnetic field |
| $\mathbf{B_1}$ ($\mathbf{B_{1xy}}$) | Induction field in transverse (xy) plane |
| CM | Common Mode |
| CRC | Colorectal Cancer |
| Cm | Matching capacitor |
| Ct | Tuning capacitor |
| DDL-OC | Diagonal Double Layer – Opposite Current |
| DDT-OC | Diagonal Double Turn – Opposite Current |
| DDL-SC | Diagonal Double Layer – Same Current |
| DDT-SC | Diagonal Double Turn – Same Current |
| DM | Differential Mode |
| DNA | Deoxyribonucleic Acid |
| DSL | Diagonal Single Loop |
| **E** | Electrical field |
| EM | Electromagnetic |
| EMF | Electromotive force |
| FID | Free Induction Decay |
| $F_0$ | Coil resonance frequency |
| $F_L$ | Larmor frequency |
| FR4 | Flame Resistance 4 |
| $^1H$ | Hydrogen (or Proton) nucleus |
| $H_1$ ($H_{1xy}$) | Magnetic field in transverse (xy) plane |
| $H_2O$ | Water |
| IBD | Inflammatory Bowel Diseases |
| MEMS | Micro Electro-Mechanical System |
| MRI | Magnetic Resonance Imaging |
| $M_{xy}$ | Transverse static macroscopic magnetization |
| $M_z$ | Longitudinal static macroscopic magnetization |
| $M_0$ | Static macroscopic magnetization magnitude |
| NaCl | Sodium chloride |
| NMR | Nuclear Magnetic Resonance |
| PIN | Positive Intrinsic Negative |
| *p*MEMS | Parallel MEMS |
| *p*$MEMS_{WG}$ | Parallel MEMS based on Waveform Generator |
| REC | Rectangular Endoluminal Coil |
| RDL-OC | Rectangular Double Layer – Opposite Current |
| RDT-OC | Rectangular Double Turn – Opposite Current |
| RDL-SC | Rectangular Double Layer – Same Current |
| RDT-SC | Rectangular Double Turn – Same Current |
| $R_{coil}$ | Coil resistance |
| $R_{el}$ | Electrical resistance |
| $R_m$ | Magnetic resistance |
| $R_{Noise}$ | Total loss resistance |
| $R_{phantom}$ | Phantom resistance |
| $R_{sample}$ | Sample resistance |
| RF | Radio Frequency |
| Rx coil | Receiver coil |
| *s*MEMS | Serial MEMS |
| *s*$MEMS_{WG}$ | Serial MEMS based on Waveform Generator |
| SNR | Signal-to-Noise Ratio |

| | |
|---|---|
| pSNR | Proportional Signal-to-Noise Ratio |
| $S_{11}$ | Reflection coefficient |
| $S_{21}$ | Transmission coefficient |
| swiM RE-Coil | Switches based on MEMS for Reconfigurable Endoluminal Coil |
| TE | Echo Time |
| TEM | Transverse Electro-Magnetic |
| TR | Repetition Time |
| Tx coil | Transmitter coil |
| VNA | Vector Network Analyzer |
| WG | Waveform Generator |
| $\omega_0$ | Coil resonance pulsation |
| $\omega_L$ | Nuclear precession pulsation |
| $\mu_0$ | Free space permeability |
| $\gamma$ | Gyromagnetic ratio |
| $\theta$ | Flip angle |
| $\tau$ | Pulse duration |

# Manuscript introduction

# Manuscript introduction

Nowadays an increasing number of people suffer from digestive health problems particularly inflammatory bowel diseases which mainly appear as ulcerative colitis and Crohn's diseases. They affect both colon and rectum with a risk to evolve into a colorectal cancer (CRC) which is one of the most common cancers. Worldwide, it is the second and the third most frequent cancer for women and men and accounts for 8.5% of all cancer deaths. The treatment of CRC at early stages allows a 5-year survival rate higher than 90% in contrast to late stages where this rate is less than 10%. This is why it is important to develop new imaging tools able to provide an accurate diagnosis for early stages.

Magnetic Resonance Imaging (MRI) is a common modality used for medical diagnosis of most human body organs in general and of abdominal and gut diseases in particular; providing a better tissue contrast and differentiation between tissues than other imaging techniques. The Nuclear Magnetic Resonance (NMR) images are able to provide medical doctors with anatomical, structural, functional and metabolic information.

This is mainly due to several developments in the field of MRI such as the increase of the static magnetic field strength to improve the SNR, the development of fast imaging sequences to reduce the acquisition time, the increase in the number of receiver channels in the MRI systems and the use of arrays of external receiver coils based on combinations of small surface radiofrequency (RF) loops to improve significantly the SNR.

Unfortunately, all these developments are still insufficient for bowel and colon wall imaging. Analysis of the deep and thin colon wall layers in view of assessing and staging of colorectal cancer is still very much challenging.

For this purpose, early works have demonstrated the feasibility and the value of receiver endoluminal coils (REC). One main advantage in the context of colon imaging is the high local SNR very close to the region of interest (colon wall layers). The gain in local SNR enables drastically decreased voxel size, a high spatial resolution and thus visualization of different layers of the colon wall.

Despite the fact that endoluminal MR imaging allows specific examination, which is not possible with other technologies, it suffers from several limitations.

A first major issue is the total safety of the patient for which no compromise can be tolerated. Strong local SAR increase can be induced by transmitter RF coil due to the presence of cables from receiver coils. Several teams worldwide including CREATIS as well as MR scanner manufacturers have worked in this field in order to make safe MR examinations. One original solution proposed by CREATIS is a fully optical-based analog signal transmission as a potential alternative to ensure total patient security respecting the international standards (IEC-60601).

A second issue is the acceptance by the patient of such endoluminal coil without excessive discomfort. The limitation of the coil diameter strongly improves this matter.

It should be pointed out that the use of a small surface coil-loop is not only a solution for the patient comfort but also for obtaining a higher local sensitivity. However, this gain in sensitivity is accompanied by its rapid decrease with the distance. Fortunately, we are

only concerned with short distances; less than 1 cm (targeted colon wall areas) which therefore minimizes the negative impact of this rapid decrease and makes endoluminal imaging a credible solution during the receive phase.

During the transmission phase however, RF receiver-coils and in particular endoluminal coils consisting of small surface coil-loops have to be swapped with the whole-body RF transmitter-coil in order to ensure a good transmitted RF pulse uniformity. In fact, both coils must be decoupled during the transmission phase in order to avoid any mutual induction and the subsequent non-uniform $B_1$ magnetic field in the vicinity of the receiver loop coil. Therefore, a decoupling circuit is mandatory to avoid uncontrolled and spatially dependent image contrast. To this end, PIN diodes are the most popular components used as RF switches in a majority of clinical systems.

Finally, another difficult problematic is related to the required coil navigation within the colon. The consequence is that the coil-loop suffers from sensitivity-map variations as a function of coil-orientation with respect to the main magnetic field ($B_0$). In fact, a maximum of coil-sensitivity is ensured only when the coil-axis is aligned with $B_0$. Departure from this optimal condition induces changes in coil-sensitivity maps and thus both intensity values and radial distribution uniformity (shape) are altered by this coil-orientation inducing significant image quality degradations. Within this context, the general question raised is: How could we design a coil to improve the early diagnosis before being affecting by the colorectal cancer or detecting this cancer at early stage?

To answer this question, one idea is the development of new one-channel reconfigurable endoluminal coil able:

- To be coupled and decoupled during receive and transmit phases, respectively.
- To adapt its coil geometry according of its orientation with respect to the static magnetic field $B_0$ to ensure a suitable sensitivity.

One way of achieving this objective is the use of an efficient MR switch able to act as decoupling element as well as to control and manage the conducting path and thus create several possibilities of loop-designs without removing the REC from human body. A few years ago, RF Micro Electro-Mechanical System (MEMS) switches (MM7100, Menlo Microsystems, Inc., Irvine, CA, USA) were introduced by GE Healthcare to act as MR compatible switches with a high electrical isolation and were successfully used for external array coils.
In view of the new possibilities brought by MEMS technology for MR coil designs, endoluminal MR imaging using RECs could also benefit from the use of MEMS switches to reconfigure the geometry-design while also ensure the active decoupling.

In this project, coil prototypes and simulated RF loop designs using MEMS technology were proposed based on specifications provided by an experimented radiologist. So, this thesis manuscript consists of four main chapters: Chapter 1 describes the global clinical and scientific contexts of this project. It provides some basis of the NMR phenomena from signal to image. Then, a theoretical presentation of different types of RF coils describing quality and limitations of each one is made. Hence, electromagnetic simulations basis are presented. And finally, a brief description of MEMS technology used in this project is done.

The second chapter is dedicated to the experimental developments related to bench and images experiments of the MEMS active decoupling context. In this work, we shall focus on studying the feasibility of using MEMS switches on endoluminal coils and then on using MEMS as active decoupling circuits. This is an interesting question considering the small size of the REC-loop and therefore its resulting small electrical resistance with respect to that of the MEMS. For that purpose, two one-channel endoluminal coil prototypes with different configurations of active decoupling circuits using MEMS placed in series or parallel to the coil-loop were designed and built. They were then characterized with dedicated phantom on experimental bench and tested in imaging conditions on a 1.5 T MR system to evaluate decoupling efficacy and speed performances. To validate their performances, MEMS prototypes were compared to a conventional PIN diode based-solution (which has the same endoluminal coil geometry and considered as a reference coil) and to a commercial external array coil.

Chapter 3 deals with simulated coil loop geometries and designs dedicated to the human colon imaging. Different miniature coil-loop geometries were defined and simulated on electromagnetic (EM) software FEKO. Each image intensity distribution was evaluated for different coil orientations with respect to B0. Complementary geometries were selected to propose reconfigurable coil displaying reduced dependency of its sensitivity with its orientation. Switching between loop geometries could be done using MEMS switches to design one-channel reconfigurable MRI RF endoluminal coils (SwiM RE-Coils). Another perspective offered by MEMS switches concerns the reconfiguration of a single loop for multi-nuclear NMR as required for spectroscopic imaging. Usually a primary coil tuned to 1H Larmor frequency is used for anatomical imaging and a secondary coil tuned to another nucleus is used for spectroscopic imaging of the desired nuclei. Using MEMS, it is shown that it is feasible to use a single loop for both steps of the imaging protocol. Preliminary results regarding a possible reconfiguration for 1H and 31P are presented and show promising perspectives.
A discussion and conclusion section including some perspective finalized this manuscript.

This works was carried out in the framework of a CIFRE thesis between CREATIS lab (MAGICS team) and GE Healthcare Inc., (Buc, France & Ohio, USA). In the scope of this thesis, the MAGICs team of CREATIS is specialized in methodology and RF instrumentation in the field of MR and GE Healthcare has an expertise in RF MEMS (Micro Electro-Mechanical System) switch technology. MR Imaging experiments were performed on GE Healthcare clinical MR scanners (1.5 T Optima MR450w & 3.0 T Discovery MR750) located at the Edouard Herriot hospital in Lyon, France.

# Chapter 1: Colon wall clinical context, MRI RF-coils and MEMS switches technology

# Chapter 1

# Colon wall clinical context, MRI RF-coils and MEMS switches technology

## Contents

*Because in this thesis we focused on the concept of introducing and navigating with an endoluminal MRI coils within the colon, the present chapter provides a brief overview of the clinical context and motivation, MRI diagnosis technique and the theory of RF coils technology including the transmission line, MEMS technology and finally the numerical electromagnetic simulations including the loss effect estimation.*

# Chapter 1: Colon wall clinical context, MRI RF-coils and MEMS switches technology

## 1.1. Clinical context

### 1.1.1. Human colon and rectum

Human colon (large intestine) and rectum are the terminal parts of the digestive tract (from the mouth to the anus). The main role of the colon is to absorb residues of water and mineral salts from food and to then produce stools which solidify while transiting in the colon until it passes into the rectum. The latter accumulates and stores them before they are evacuated out of the human body.

As can be seen in Fig. 1-1(left), the colon is composed of several parts: Cecum, ascending colon, transverse, descending and sigmoid colon. Knowing that the colon structure is not uniform, colon length and diameter are variable from 1.5 to 1.8 m and from 3 cm (sigmoid) to 8 cm (caecum), respectively. Overall, rectum length and diameter are about 20 cm and 5 cm.

As seen in Fig. 1-1(right), the colon wall is about of 2 mm global thickness. The layers from inside (light) to the outside are: Mucosa, Submucosa, Muscularis (Muscularis externa) and Serosa. The rectum has the same colon layers but for the Serosa.

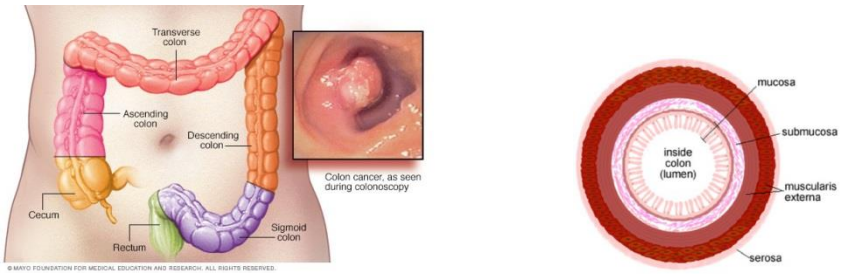


**Fig. 1-1.** The human colon-rectum anatomy. (left) The terminal digestive tract parts [1]. (right) The wall layers description/structure [2]. From inside (light) to the outside are: Mucosa, Submucosa, Muscularis (Muscularis externa) and Serosa.

As all body organs, Human colon and rectum can be affected by several diseases such as inflammatory bowel diseases (IBD).

### 1.1.2. Inflammatory bowel diseases

Nowadays, lot of people suffer from inflammatory bowel diseases (IBD) characterized by lesions and disorders affecting the digestive tract [3]. They mainly appear as ulcerative colitis and Crohn's diseases. The ulcerative colitis is characterized by inflammation and contiguous damaged areas occurring first at the rectum and which can propagate further into the innermost layer of the colon mucosa (Fig. 1-2(left)). The Crohn's disease is characterized by inflammation and damaged areas occurring in several portions (discontinuous parts) along the mucosa of all digestive tract (Fig. 1-2(right)) and often spreads deep in multiple wall-layers.

According to the inflammation degree and location, both ulcerative colitis and Crohn's diseases have some common symptoms, such as abdominal pain, fever, tiredness, diarrhea, blood in stool, reduced appetite and unexplained weight loss.

Exact causes of an IBD remain unknown but a main possible cause is related to a defective immune system. A normal immune response leads to an attack of the undesirable virus and bacterium to protect the body. However, an abnormal or incorrect immune response (due to an immune system malfunction) may lead to attack not only virus and bacterium but also digestive tract cells and thus inducing an inflammation of the gastro-intestinal tract. Some risk factors, such as heredity (genetic component), cigarette smoking, some nonsteroidal anti-inflammatory medications and the life environment can be causes of IBDs.

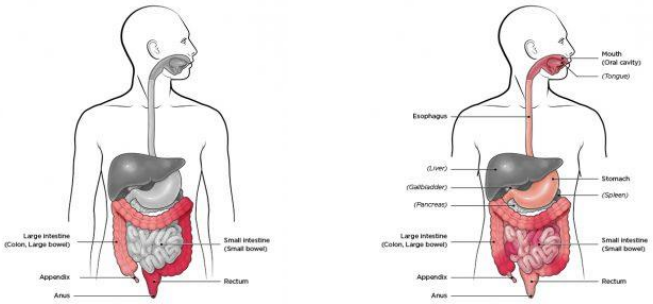


**Fig. 1-2.** Inflammatory bowel diseases mainly appear as (left) ulcerative colitis or (right) Crohn's disease [4].

Unfortunately, IBDs can advance and evolve into a colorectal cancer (CRC) [5]–[8].

### 1.1.3. Colo-Rectal Cancer

The normal function of the human body relies on keeping a constant cells number in the human body (cell homeostasis phenomena). The natural death of certain cells at every moment is accompanied by growth and division of identical cells according to instructions of cells DNA. However, changes (or mutations) in the DNA of healthy cells lead to an unregulated continuous cell replication (uncontrolled multiplication of abnormal cells). In other words, the initial affected cell becomes "immortal" by cloning itself: that is what we call cancer where cancerous cells accumulation leads to a tumor. Moreover, the cancerous cells can migrate (with time) and settle nearby normal tissues and then body organs of the rest of body to form deposits: that is what is called metastasis.

Our research in this thesis has been carried out in the context of Colorectal Cancer (CRC) which also consists of an uncontrolled multiplication of abnormal cells where the primary tumor develops on the colon or/and the rectum. The fact that the organs concerned are not easily accessible means that CRC development usually takes place unnoticed and the apparition of symptoms indicate an advanced stage. These symptoms include common symptoms to most cancers such as weakness, tiredness, unexplained weight loss and reduced appetite as well as some usual symptoms of digestive disorders such as blood in the stool, persistent abdominal disorders (cramps, gas or pain) and changes in bowel habits (diarrhea, constipation...).

Fig. 1-3 illustrates CRC staging (from stage 0 to IV) of the extent or progress of the cancer appearance which is very important for determining the appropriate treatment.

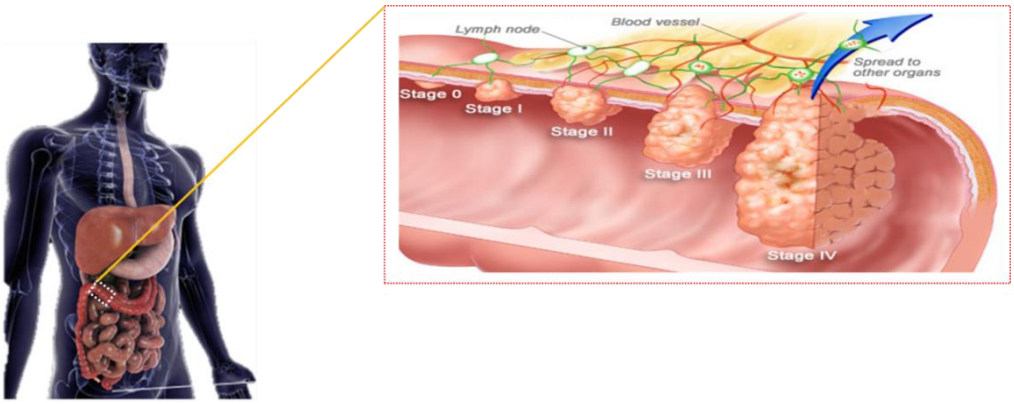


**Fig. 1-3.** Colorectal cancer stages [9].

As can be seen, developments at the early stages take place within the thin colon wall layers and thus being able to diagnose these early stages and increase the survival rate requires being able to analyze deep and thin colon wall layers which is still a challenge nowadays. Recent statistics show that colorectal cancer is one of the most common cancers: worldwide, it is the second and the third most frequent cancer for women and men, respectively [10] and accounts for 8.5% of all cancer deaths [11].

Efficient treatment requires screening, characterization and treatment with monitoring of colorectal cancer extension. The screening is done by checking the blood in the stool. This can be followed by a colonoscopy [12], [13] so as to detect the colorectal cancer. Colonoscopy is based on acquisition of an optical image of the colon wall by the introduction into the patient of a tube fitted with camera, light source and forceps/clamp. This is the initial extension assessment which permits to define the CRC stage (Fig. 1-3) according to the Tumor Node Metastasis (TNM) classification [14], [15]. According to the information of local or regional severity and extension, a therapeutic strategy can be adopted.

Surgery, radiation therapy and chemotherapy are used as possible treatments of CRC but the therapy success depends on the size, location and stage of the cancer along the colon and/or rectum. The fact that CRC developing in the colon can lead to intestinal obstruction at late stages followed by intestinal perforation renders treatment difficult and generally patient's death.

Contrary to that, detection and treatment of CRC at early stages reduce the dying risk and allows a 5-year survival rate higher than 90%, in contrast to late stages where this rate is inferior to 10% [16]. For this reason, an early, accurate and effective diagnosis method is required. MRI is the most frequently used for extension assessment diagnosis [17]–[20] and is the modality concerned by this thesis.

## 1.2. Diagnosis: MRI technique

Magnetic Resonance Imaging (MRI), based on the Nuclear Magnetic Resonance (NMR) phenomenon, is a powerful imaging modality. It can explore different human body soft tissues and organs by providing high spatial resolution and intrinsic contrast of anatomical, structural, functional and metabolic tissue information. To achieve that, several manufacturers (GE Healthcare, Siemens healthineers, Philips …) develop MRI systems.

Since the MRI technique is based on the NMR phenomenon, we attempt to provide a brief overview of important NMR basic principles in the following section.

### 1.2.1. Signal creation: NMR basic principles

The Nuclear Magnetic Resonance (NMR) phenomenon was discovered in 1946 [21], [22]. An NMR experiment relies on three main steps: RF excitation of the region of interest (ROI), detection of the NMR signal and signal processing (MR image reconstruction). In this section, we focus on the first and second steps.

The principle is related to the exploitation of typical nuclei having a non-zero spin number associated to a magnetic moment μ such as $^{1}H$, $^{3}He$, $^{13}C$, $^{129}Xe$, $^{19}F$, $^{23}Na$, and $^{31}P$. These nuclei can be found in the human body at different concentrations and thus MRI can be carried out yielding a powerful diagnostic tool. The hydrogen nucleus (often called proton) $^{1}H$ is the most used one because it is easier to be detected than the other nuclei thanks to its natural abundance in the $H_2O$ molecules which represent 70% of the human body mass. It permits to produce anatomic and structural images as well as assessing physiological information. Other nuclei can be used in combination with the proton to obtain additional information.

During an NMR experiment, nuclear spins of those specific nuclei interact with an intense external static magnetic field ($B_0$). In absence of the latter, all spin states have the same energy and the orientation of magnetic moments is random due to thermal agitation. Thus, the resultant macroscopic nuclear magnetization is zero. In the presence of $B_0$ (assumed to be aligned with the z-axis), each magnetic moment is preferably aligned with $B_0$ and executes a precession motion around $B_0$ (Z axis). In the case of the proton ($^{1}H$), its spin is 1/2 which means two quantum states are possible (±1/2) depending on the spin orientation with respect to $B_0$ and thus the spin ensemble is divided into two spin populations: those having a parallel orientation with respect to $B_0$ which corresponds to a low energy state and those having anti-parallel orientation which corresponds to a high

energy state. All magnetic moments precess around $B_0$ at a specific frequency called Larmor frequency($f_L$) which is given by:

$$f_L = \frac{\gamma}{2\pi} B_0 \tag{0.1}$$

where $\gamma$ is the gyromagnetic ratio[1] of a given nucleus.

It should be noted that the number of parallel and anti-parallel nuclei is not the same: due to a very small difference of the energy (gap) between parallel and anti-parallel states. To get an idea about this quantity, for a population of 1 million nuclei in the case of a magnetic field of 1.5 T and at a temperature of 25°C the difference in population is only of 7. Although weak, this difference leads to a resultant macroscopic nuclear magnetization (M) which is proportional to $B_0$ and oriented parallel to the $B_0$ direction. The resultant macroscopic magnetization displays no transverse component since the individual spins do not display a coherent phase. Due to its orientation, this resulting macroscopic magnetization obtained at the thermal equilibrium state is coined the longitudinal component ($M_z$) Since the created static macroscopic magnetization magnitude[2] ($M_0$) is very small, MRI is considered as a very low sensitive modality and thus static magnetization and variations regarding different tissues are not easy to detect ($M_z$ is parallel to $B_0$ while being several orders of magnitude smaller). After creating this low magnetization, the question now is: how can it be observed?

The idea is to move (or flip) the magnetization from its equilibrium state to a plane where $B_0$ does not exist in order to observe its return to equilibrium using precession properties. This can be achieved by applying to the system an additional transverse magnetic field (called $B_1$) (with the help of a transmitter RF coil) which has the property of oscillating at the Larmor resonant frequency $f_L$. This resonance condition has to be met. If not the net effect of this $B_1$ field will not result in a proper flipping of the magnetization. Assuming a constant $B_1$ amplitude-value (RF pulse), the resulting effect is a tilt of the magnetization from its equilibrium position and around the axis of application of the $B_1$ field, by a certain flip angle ($\theta$ in rad) proportional to the RF pulse duration $\tau$ (in second) according to the following relationship:

$$\theta = \gamma B_1 \tau \tag{0.2}$$

Therefore, if the RF pulse frequency is the same as the Larmor frequency (resonance condition), the flip angle of the macroscopic magnetization is proportional to the RF pulse

[1] The Signal-to-Noise Ratio (SNR) increases with the gyromagnetic ratio.
[2] $M_0$ depends mainly on the $B_0$ field and the gyromagnetic ratio.

($B_1$) amplitude and duration. A 90° flip angle means that the macroscopic magnetization which is in the z direction in the equilibrium state is flipped in the transverse plane (xy) which is perpendicular to $B_0$ and thus the resulting transverse magnetization[3] ($M_{xy}$) reaches its maximum magnitude value. So, the RF pulses permits to manipulate effectively the magnetization through the excitation of the spins having a Larmor frequency within the frequency bandwidth of the RF pulse [23].

At the end of the RF excitation, two types of energy exchanges can be observed:

i/ The longitudinal magnetization ($M_z$) returns to its thermal equilibrium state (i.e. aligned with $B_0$ direction) from 0 to the maximum magnitude of longitudinal magnetization in the equilibrium state ($M_0$) due to energy exchanges of the spins with the surrounding environment (spin-medium interactions). This relaxation can be described by a characteristic time constant noted T1 [24]. Bloch's equations described the longitudinal magnetization evolution:

$$\frac{dM_z}{dt} = -\frac{(M_z - M_0)}{T1} \tag{0.3}$$

The return of the longitudinal magnetization component is given by (Fig. 1-4(left)):

$$M_z(t) = M_0 - \big(M_0 - M_z(0)\big)\exp(-\frac{t}{T1}) \tag{0.4}$$

ii/ The second observed phenomenon is the disappearance of the transverse magnetization ($M_{xy}$) because of the interactions between the spins (spin-spin interactions) which gradually destroys the coherence between spins that was obtained by the application of the RF pulse. This second relaxation process can be characterized by a second transverse relaxation time constant noted T2 which describes the transverse magnetization decay [24]. Bloch's equations also described the transverse magnetization evolution:

$$\begin{cases} \frac{dM_x}{dt} = -\frac{M_x}{T2} \\ \frac{dM_y}{dt} = -\frac{M_y}{T2} \end{cases} \tag{0.5}$$

Solving equation of the transverse magnetization component yields the well-known solution showing an exponential decrease of the $M_{xy}$ amplitude with time from the maximum magnitude of $M_{xy}$ to 0 (Fig. 1-4(right)):

[3] The $M_{xy}$ is under the effect of both $B_0$ and $B_1$.

$$M_{xy}(t) = M_{xy}(0)\exp(-\frac{t}{T2}) \quad (0.6)$$

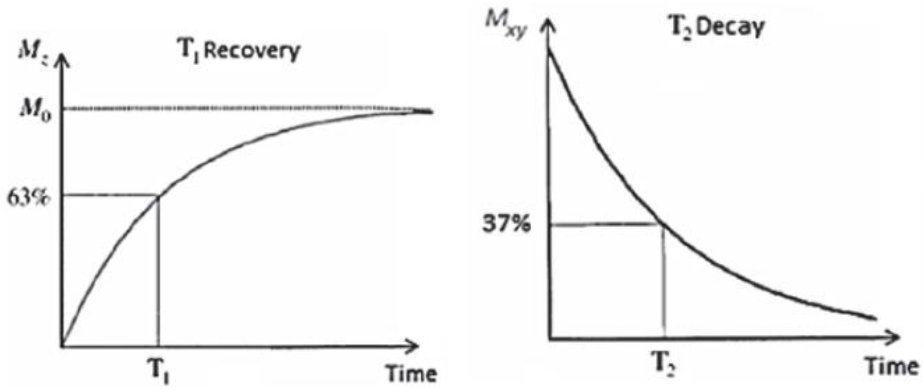


**Fig. 1-4**. T1 relaxation time recovery (left) of the longitudinal magnetization and T2 relaxation time decay (right) of the transverse magnetization [24], [25].

During this relaxation processes (longitudinal and transverse) the macroscopic magnetization precesses around $B_0$ and this motion is the basis for the creation of the NMR signal. Placing a receiver RF coil with its plane perpendicular to the transverse plane will lead to the creation of a magnetic flux variation in the loop coil leading to an induced an electromotive force EMF[4] (thus an electrical signal) at the ports the receiver loop coil. Hence, the RF coil detects an NMR signal also called Free Induction Decay (FID) which can then be further processed to reconstruct a spectrum or an image (with the addition of magnetic field gradients). The resulting image SNR is therefore highly dependent on the signal intensity and maximizing the latter requires that the coil be as close as possible to the sample and that its operating frequency being the same as the Larmor frequency of the targeted nuclei. This can be done by using a volume MR coil such as the whole body coil of the MRI system as transceiver or as in our case a specific MR coil for the receive phase alone.

To measure an NMR signal and to be able to reconstruct an image, an MRI sequence should be used. The latter consists of a repetition of successive events taking place at specific times namely, magnetization flip, signal measurement and recovery period. Two main sequence parameters related to the timing of these events are: the echo time (TE) which corresponds to the time delay between magnetization flip and signal measurement and the repetition time (TR) which is corresponds to the time between two successive magnetization flips. Several types of sequences can be used but since the objective of

[4] The RMN signal is coming from the elementary volume.

this project is related to the geometry-design of the receiver RF coil, only two basic sequences were used: gradient echo and fast spin echo sequence.

So, The NMR signal is detected by an MR coil and amplified before being digitized and processed to reconstruct MR images. In the next paragraph, presentation of signal detection and transmission are made.

## 1.3. Signal detection and transmission:

### 1.3.1. MR coils

An MRI coil is a resonating circuit (RLC tank) composed of a metallic loop (or several loops) formed, generally, by copper wire or strip conductors, equipped with different electronic components (such us capacitors, diodes, inductances …) and placed around or close to the sample (tissue, phantom …). It permits to convert by induction the precession motion (which takes place at the Larmor frequency) of the macroscopic magnetization during relaxation into an electric voltage of the same frequency at its terminals. From an electrical point of view, an isolated MRI coil is an electronic circuit consisting mainly of an RF loop tuned to be resonant at the Larmor frequency of the targeted nucleus. This ensures that a maximum RF energy is transferred between the coil and the nuclei under investigation and vice-versa.

#### a) Volume coils

Volume coils can be used as RF transceivers (i.e. for both RF transmission and RF reception). In fact, during RF transmission, a signal is sent to the volume coil, such as the whole-body coil (WBC) of the MRI scanner, to generate a short-lived magnetic field ($B_1$ field used to flip the macroscopic magnetization) with amplitude proportional to the current intensity flowing through the coil. The use of such volume coil is meant to ensure a uniform excitation with a controlled and precise flip angle of the magnetizations of tissues to be imaged. During the RF receive phase, there is no deliverance of the excitation magnetic field and thus it is possible to use the body coil to collect the NMR signal from the tissues under investigation. A uniform sensitivity profile can be obtained over the whole region of interest. However, the low magnetization and the relatively large distance between the body coil and the region of interest leads to a very small induced current in the body coil and therefore a small NMR signal which is a limitation for the majority of MR applications.

Solving this issue has led to the development of specific receiver coils for which the RF surface coil is an interesting solution in certain situations.

## b) Surface coils

A surface coil is usually an external device placed as close as possible to the region of interest thus enhancing the captured NMR signal and the resulting image SNR.

A well-chosen surface receiver coil can lead to significantly improved image SNR in the region of interest while also displaying a non-uniform sensitivity with a decrease when moving away from the loop coil(the sensitivity which is inversely proportional to the loop radius and decreases rapidly with the distance [26].

For a circular surface coil with a radius r, through which flows a current I, this dependency along the coil axis, is given by the following relationship:

$$SNR\ \alpha\ \frac{B_{1xy}}{I} = \frac{\mu_0}{2}\frac{r^2}{\left(r^2+d^2\right)^{\frac{3}{2}}} \qquad (0.7)$$

where $\mu_0$ is the magnetic permeability in free space ($4\pi.10^{-7}$ H/m) and d distance from the coil-plane. Equation 1.7 is plotted in Fig. 1-5 for three different coil radiuses and illustrates that the coil radius must be a carefully chosen parameter so as to optimize the SNR in the region of interest. Another feature of surface coils is the non-uniformity of the resulting SNR with the distance from the coil plane.

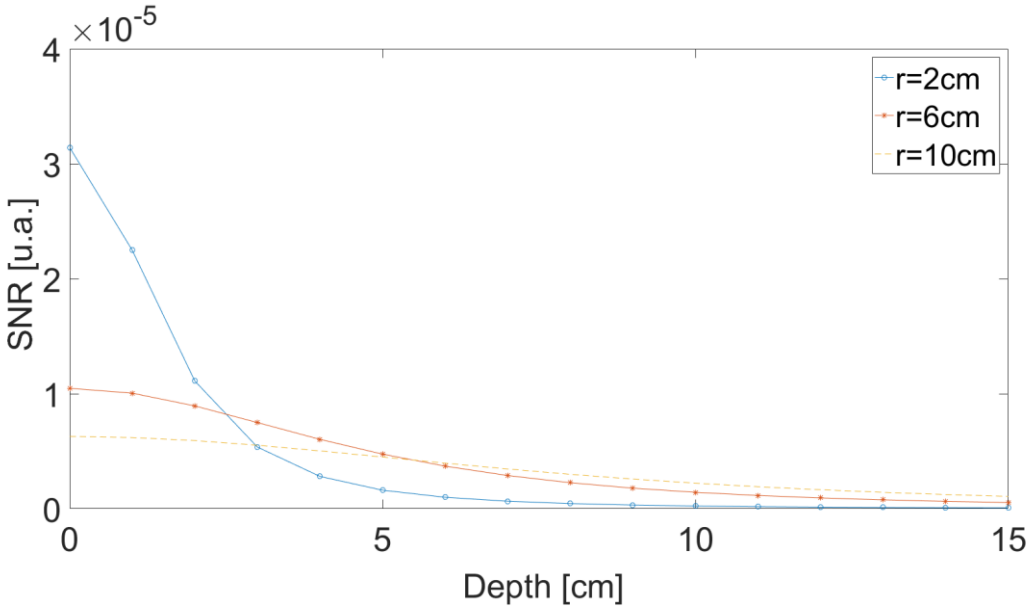


**Fig. 1-5.** SNR profile versus the exploration depth Measured from different coils size.

This particular feature while acceptable during the receive phase cannot be tolerated during the transmit phase. This phenomenon can be a limitation for several specific

applications where the region of interest lies far from the body surface thus annealing the specific advantage of such coils.

Once the NMR signal is detected by a reception coil, it must be sent to the MRI system. Although active research is being carried out for a wireless transmission, for the moment the signal transits through a physical transmission line. To achieve that, several technologies are reported in the literature but the coaxial cable is the conventional technology nowadays.

## 1.3.2. Coaxial cable

The coaxial cable (galvanic cable) is the unbalanced type which is based on the use of two conductors with unequal impedances. As shown in Fig. 1-6, a coaxial cable is made up of two conductors: a central inner conductor and an outer metallic braid conductor, often called the shield, (used as ground) with inner and outer surfaces. The two conductors are separated by an insulation dielectric. The external layer is an insulation sheath that also ensures mechanical and chemical protection of the cable. This type of transmission lines are commercialized with two characteristic impedances $Z_0$ (50 Ω for applications where important electrical power is sent or 75 Ω when losses have to be minimized). In this thesis all used coaxial cables have 50 Ω characteristic impedance.

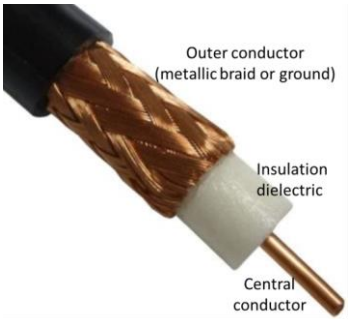


**Fig. 1-6**. Picture of a coaxial cable used as galvanic line.

The coaxial cable being the physical support linking the coil to the amplification stage, all three need to matched impedance-wise so as to ensure an efficient transmission.

### Impedance matching

A coaxial cable is mainly characterized by its impedance ($Z_0$) which is the voltage to current ratio at any point of the transmission line. During signal propagation, there is an incident wave (useful signal) in the load stage and a reflected wave (signal loss), circulating in opposite direction, back to the RF source. The reflection coefficient (Γ) is

the reflected-voltage to incident-voltage ratio and can be defined at any given point on the transmission line and at any frequency.

Since an MR coil detects the NMR signal; then sends it to the transmission line (coaxial cable in this case), coil and cable are considered as generator and load, respectively.

$$\Gamma = \frac{|Z_{cable} - Z_{coil}|}{Z_{cable} + Z_{coil}} \quad (0.8)$$

To maximize the transmitted power and therefore the signal, reflection losses between coil and cable must be minimized as much as possible and thus the voltage reflection coefficient (which is between 0 and 1) should be as near to 0 as possible corresponding to a reflected wave with zero amplitude. To achieve that, the numerator of the reflection coefficient (eq. 1.8) must be equal to 0 in the ideal case. Thus, $Z_{coil}$ should be as near to $Z_{cable}$ as possible (or equal to $Z_{cable}$ in the ideal case). And this justify why it is required to match the coil to the $Z_{cable}$ (noted $Z_0$). In other words [27]:

$$Z_{coil} = R_{coil} + j\, X_{coil} = Z_0 \quad (0.8)$$

that is $R_{coil} = Z_0$, $X_{coil} = 0$, where $R_{coil}$ and $X_{coil}$ are, respectively, real and imaginary parts of the coil impedance ($Z_{coil}$). $Z_0$ is generally taken to be 50 Ω (sometimes 75Ω). In this thesis, all used coaxial cables have $Z_0$ of 50Ω (RG-58).

Once understanding the importance of having tuned and matched a coil, the next question is:

**How to tune and match an MR coil when using coaxial cables?**

To achieve this goal, two classical ways are reported in the literature: capacitive coupling and inductive coupling.

## ***a. Inductive coupling***

This method permits to adjust the global impedance of the coil to $Z_0$ (50Ω). It is based on inductive transformer principle where the received signal is transmitted by the coil-loop inductance ($L_s$) to another inductance ($L_P$) connected to the transmission line with $Z_0$ (Fig. 1-7) [28].

The inductive coupling between the inductances of primary and secondary circuits represents the mutual inductance M which is given by:

$$M = k\sqrt{L_p\, L_s} \quad (0.9)$$

where k is the coupling coefficient between the two stages.

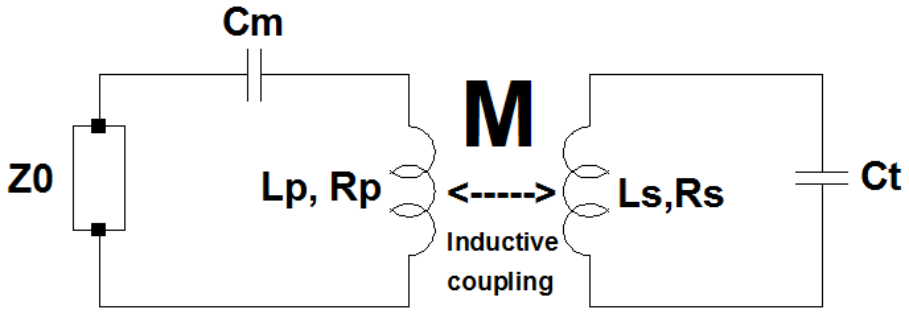


**Fig. 1-7.** Electronic schematic of tuned and matched RF coil based on inductive coupling principle. (left) The primary circuit which serves to match (right) the secondary resonant circuit. The capacitor $C_t$ serves to tune the coil at $F_0$. Lp, Rp, Ls and Rs are inductance and resistance of primary and secondary circuits, respectively.

In this case, the inductive coupling depends mainly on the distance separating the loops and loop size. One advantage of this method is that tuning and matching values are independent. In addition, inductive coupling method has the advantage of reducing the load effect when the sample is placed in the coil where the electric field distribution in the sample is symmetrical regarding the coil (reduced shift of the resonance frequency) [28]–[30]. However, the inconvenience is the size limitation especially in the case of endoluminal imaging. In this case, the inductive coupling depends mainly on the space between loops or coil-loop size [28]–[30].

### ***b. Capacitive coupling***

Contrary to the inductive method, the capacitive method is based on the use of only the coil circuit (Fig. 1-8). Since $C_t$ serves to tune the coil to $F_0$, adding another capacitor $C_m$ serves to get directly the desired impedance matching $Z_0$ (50Ω). R and L are coil resistance and inductance, respectively. There are two ways to do that: series or parallel tuning.

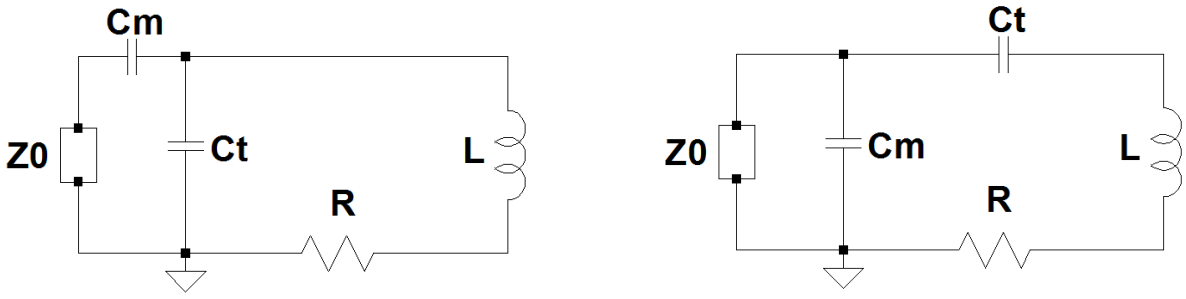


**Fig. 1-8.** Electronic schematic of tuned and matched coil based on capacitive coupling principle using (left) parallel tuning or (right) series tuning. In both cases, $C_t$ and $C_m$ serve to tune and match the coil at $F_0$ and to $Z_0$ (50Ω).

In the case of parallel tuning (Fig. 1-8(left)), the RF coil-loop can be tuned to the desired resonance frequency by adding tuning capacitor ($C_t$) in parallel to the loop. In other words, the resonating loop is realized with capacitive tuning associated to a series matching. In the case of series tuning (Fig. 1-8(right)), $C_t$ is added in series with the coil-loop. In other words, the resonating loop is realized with capacitive matching associated to a series tuning.

In the two configurations, there are interdependencies between $C_t$ and $C_m$. That means the modification of one of them induces a modification for the other which is important when characterizing the coil on bench. However, if this dependency is inconvenient, the capacitive coupling technique permits to cut the ground currents leading to a reduced dielectric effect with the sample and thus reducing the losses [31]. The efficacy of this method depends on the position of the sample regarding the coil. From a practical point of view, this technique is better suited for miniature coils used for endoluminal imaging (no need for a secondary inductance-loop and less capacitors required). For these reasons, in this thesis we focused on coil-designs based on the capacitive method in particular series tuning configuration (please find details in chapter 2 of the manuscript).

Once the MR surface coil is connected to a coaxial cable while respecting the optimal tuning and matching, the cable is then connected to the MRI system. In this thesis, this link is ensured through a specific interface connector.

### Interface connector

To connect our home-made receiver coil to the MRI scanner of GE Healthcare Inc., it is necessary to use an interface connector (A-PLUG) (Fig. 1-9) with the adequate configuration file [32]. In this thesis, we worked on an Optima 1.5 T MRI scanner (MR450w).


**Fig. 1-9.** An interface connector type of A-Plug (GE Healthcare Inc.).

**RF TRAPS**

The coaxial technology is considered as the conventional technology used to transmit the NMR signal detected by the MR coils. However, it requires the use of certain specific elements named RF traps placed along the cables. In such a transmission line, two signal propagation modes can intervene herein. The first one is the Differential Mode (DM) signal which is carried out by the strong coupling effect between the central conductor and inner surface of the grounded shield. Therefore, it results two currents with the same magnitude but opposite current direction (180° phase) (there is a voltage difference between these two conductor-surfaces). In this case, DM signals are transmitted along coaxial cable as a TEM (Transverse Electro-Magnetic) wave between these two surfaces and this is the useful information.

Unfortunately, a major RF engineering problem is the presence of unwanted Common Mode (CM) currents (which represents the second propagation mode) on the shield of the coaxial cable often called common or ground and considered as a zero potential. In fact, the strong coupling between the central conductor and inner surface of the outer conductor leads to force the CM currents to move on the outer surface of the shield and the characteristic of this CM current is that it flows in the same direction as the current flowing in the central conductor [33], [34] ($I_3$ in Fig. 1-10).

In MRI examinations where a surface coil is interfaced with a coaxial cable, unwanted CM currents are due to several factors [33]. The first cause is the absence of a properly grounded cable termination. The second origin is related to the coupling between resonating circuits such as a body coil (which acts only as transmitter) and a surface receive-only coil, where CM signals are due to the transmission-coil field (external interference and radiation) induced onto the coaxial cable shield of the receiver-coil. Another origin is due to the coupling/interaction between the coil-loop (unbalanced loop voltages) and the coaxial cable shield but in the case of receive-only coils (which is our case) this effect is not predominant.

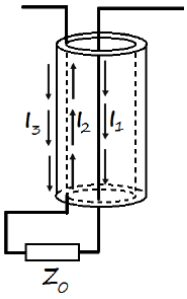


**Fig. 1-10.** Currents flowing on a coaxial cable [34].

In any case, an induced electric field (**E**) is generated near the coaxial cable when connecting a coaxial cable to a surface coil inside an MR scanner. However, since MR is based on high frequency electromagnetic fields, the RF electric field induces currents at the same frequency in conductors in particular coaxial cables forming an asymmetrical transmission line and creating additional losses (dielectric and radiation).

As the frequency grows, the wavelengths become shorter and comparable to the length of the used coaxial cables and thus the coaxial shield is forced to act as antenna of arbitrary length and generate antenna current patterns, where the maxima occur at each odd number of quarter-wave lengths.

As a result, CM signals lead to a serious risk of a local heating (RF burn) in patient tissues. This is described by the increase of the local Specific Absorption Rate (SAR) [35]–[37] in particular with the increase of the static electric/magnetic field of the MRI system [38]–[40]. In addition, CM signals affect also the coil performance due to the excess noise introduced into the MRI environment which leads to drops in SNR, and thus a degradation of the MR images quality. Therefore, it is fundamental to reduce the CM signals as much as possible.

Different practical solutions have been reported in the literature to suppress or reduce the propagation of common mode currents along the shield of a coaxial cable. A first simple solution is to use coaxial cables with lengths inferior to λ/4 to avoid peak local overheating along coaxial cables. This corresponds to about 78 cm at 1.5T and 39 cm at 3T which is relatively short length and not always possible.

LC (Inductor-Capacitor) traps blocking current such as RF traps, balun or again common-mode choke have been proposed in the literature. Their role is to filter parasitic currents flowing on the outer surface cable shield of the reception coaxial cable [41], [42] or to minimize the electromagnetic coupling between channels of a reception coil in the case of array technology or to minimize the coupling between loop elements of different resonance frequencies [43].

A simpler design of an RF trap (Fig. 1-11,a) consists in using only one capacitor placed in parallel to a solenoid [33], [44]. The solenoid can be achieved by winding a coaxial cable for a certain number of turns and soldering a variable capacitor between the two ends of the outer surfaces of the cable ground. The number of turns and the range of capacitor values depend on the operating frequency. Finally, the trap is adjusted by changing the capacitor value and visualizing on a Vector Network Analyzer (VNA) until achieving the tuning of the trap at the coil resonance frequency. It should be noted that multiple traps should be placed at specific distances along coaxial cables to avoid the maximum of

current magnitudes (generally every λ/4 starting from the coil). The signal flowing in the inner conductor of the coaxial cable is not affected.

In this thesis, Fig. 1-11,b illustrates the picture of one of the RF traps used in MR experiments to filter parasitic currents flowing in the outer surface of each coaxial cable ground at 64 MHz.

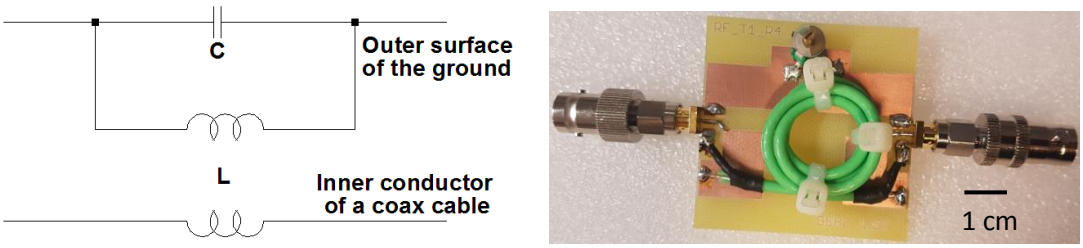


**Fig. 1-11.** The electrical schematic (left) and the picture (right) of an RF trap designed for filtering parasitic currents flowing in the outer surface of a coaxial cable ground. In green, a coaxial cable winding to form an inductance (four turns in this example, with a diameter around 1.4 cm for each turn). A variable capacitor (range of 2-22 pF) is soldered in parallel to the formed inductance to create an LC circuit operating to filter parasitic currents at 64 MHz.

Another solution that deserves to be mentioned due to its particular advantage in the case of endoluminal imaging concerns optical transmission lines. It consists in replacing the galvanic wire connection by fiber optic link to ensure full optical transmission of the NMR signal and thus full patient safety during the colon exploration [37]. It should be noted that this is the objective of several teams in the world, including team "MAGICS" of CREATIS Lab which proposed an electro-optical conversion using a crystal with specific properties [17]. However since this solution was not used in this thesis we will not go into further details.

In this present work, all RF and DC links are based on the conventional (galvanic) technology: coaxial cables fitted with RF traps. However in an endoluminal imaging context which is the subject of this thesis, this may not be a realistic solution due to the size and geometry of such traps which are not compatible with human colon size (patient discomfort and acceptance issue). Indeed in the case of colonic wall imaging, external array coils do not enable high enough SNR to be able to analyze the thin colon wall layers and enable the early diagnosis of pathologies developing in the colon. An interesting idea is to place a dedicated miniature coil inside the colon very close to its wall layers which is the region of interest (ROI). This technology is called endoluminal coils used for endoluminal imaging.

## 1.4. Endoluminal imaging

Endoluminal imaging is an attractive solution for getting high local SNR and thus providing very high spatial resolution of the image for all deep-lying organs. An endoluminal coil is a specific type of surface coils based on dedicated small coil size placed inside of the human body to be close to the ROI; thus to image the deep regions (such as deep and thin colon wall layers) which is not possible with the external coils.

Endoluminal coils can be used for RF transmission but they suffer from the $B_1$ inhomogeneity. Usually endoluminal coils are used only for reception in combination with the Whole-Body Coil (WBC) integrated in the MRI system for transmission.

In the literature, an MRI endoscopic receiver coil has been proposed [45] and used for endoscopic MRI in the upper gastrointestinal tract [46]. Previous works have demonstrated the feasibility of using endoscopic coils for imaging the prostate [47]–[50] or colonic tissue [51]–[58] with high spatial resolution. Other previous works have demonstrated the possibility of using endoscopic coils to differentiate the intestinal wall layers in rabbits [59], [60]. In intervascular applications, MRI endoluminal receiver probes with high spatial resolution have also been proposed [61], [62]. Despite these improvements, human digestive system and in particular the colon wall in depth is still difficult to be explored.

It should be noted that using this combination of a separate transmitter and receiver coil as done with the WBC and endoluminal coils, requires a decoupling strategy since both receiver and transmitter coils both have the same resonance frequency.

### Coil decoupling

During the transmit phase (transmission of RF $B_1$ pulse), the endoluminal coil must be decoupled from the transmitter coil by moving away from the coil resonance frequency from the Larmor frequency. This is done to avoid the inductive coupling between RF coils and the RF concentration close to the receiver coil that could lead to flip angle variations and safety issues. During the receiver phase, the endoluminal coil frequency should be restored and it is the resonance frequency of the transmit coil that should be shifted. Additional circuits and components should be added to the coils to ensure this active decoupling or active detuning that have to be operated depending on the sequence timing. PIN diodes are the most popular components used as RF switches in the majority of clinical systems. In this thesis, we propose to exploit MEMS switch technology as

alternative solution. A description of MEMS technology is briefly presented in the next section and in details in chapter 2.

# 1.5. MEMS technology

## Why MEMS technology in MR applications

MEMS switches can be used in MR applications mainly for two purposes:

a) As an active decoupling element in receiver coils

b) As a switch enabling modification of the current path and therefore reconfiguration of the coil geometry to simplify the coil design and to propose new geometry solutions for medical diagnosis or to accomplish a specific role. In the literature, MEMSs were mainly used for external coils for different MR applications such as: a reconfiguration of external two-channel array coil geometry to achieve spin and torso MRI diagnosis [63], a decoupling strategy of double-tuned RF coil for achieving [64], [65], a design with high RF shimming performances (high localized $B_0$ homogeneity) [66] and an MRI-compatible wireless (power transfer system) receive coil array [67].

In the case of endoluminal coils, both features are very interesting. Indeed, reconfiguration of coil geometries to lessen the adverse consequence of coil orientation with respect to $B_0$ is an interesting proposition. This could be done using MEMS switches which once integrated in the endoluminal coil could also fulfill the role of active decoupling element. These two aspects will be covered in chapters 3 and 2 respectively but in the next paragraphs, we will give a brief overview of MEMS switches which will also be further developed in chapter 2.

## MEMS switch

The used MEMS (Micro Electro-Mechanical System) switch (MM7100, Menlo Microsystems, Inc., Irvine, CA, USA) (Fig. 1-12) is developed by GE Healthcare Inc. [68]. It is a fast and pure mechanical switch based on a mobile micro metallic actuator fabricated inside a chip of 1 cm x 1 cm packaging-size. Table 1-1 illustrates some important characteristics of this MEMS switch. The important feature is the possibility to fully disconnect the RF element from the circuit; ensuring high isolation. Also, MEMS has low power consumption (a few nW) due to the low necessary current (a few pA) and has fast switching delays (a few µs).

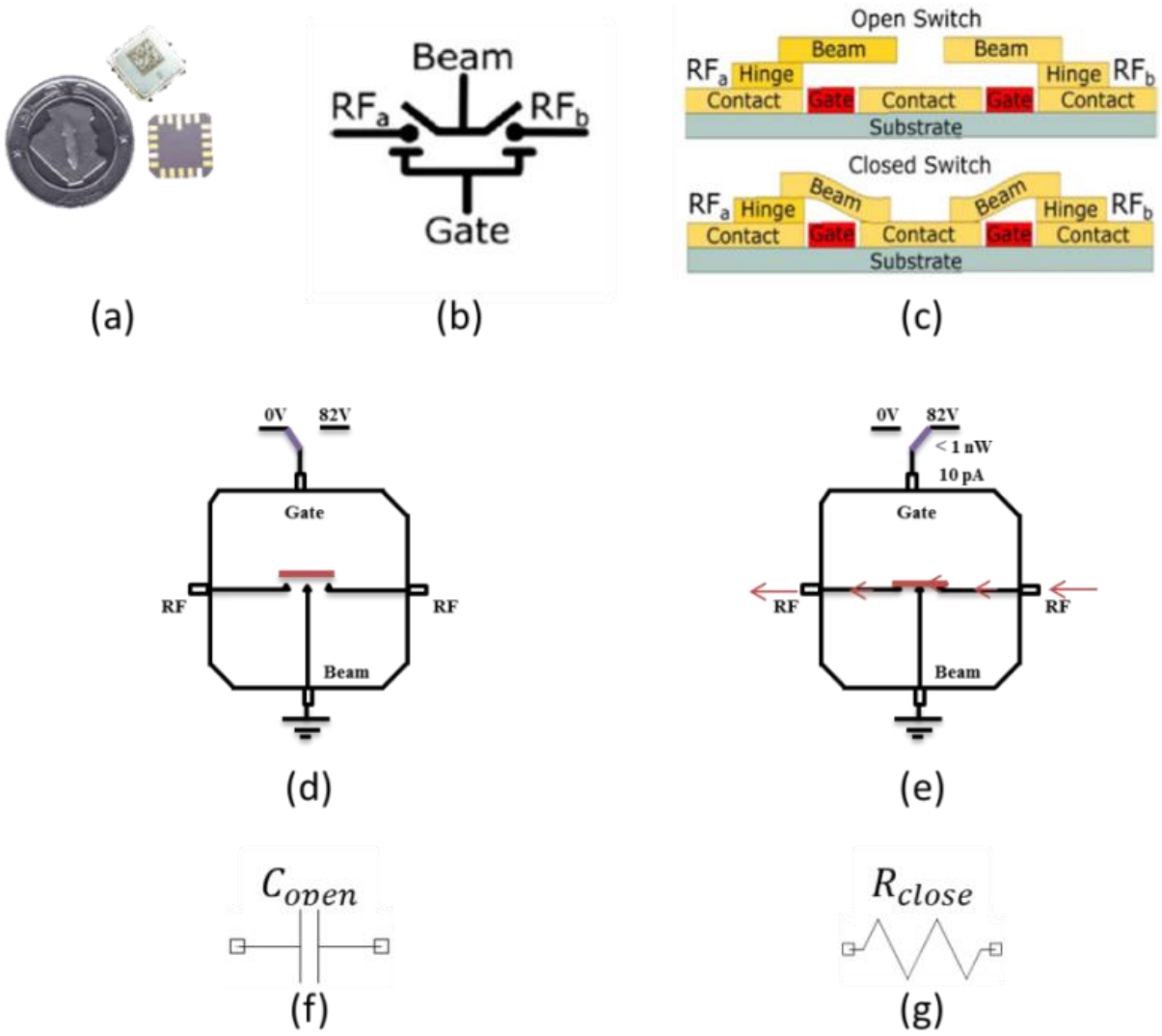


**Fig. 1-12.** The MEMS switch (a) picture (b) symbol (c) side view (d) open state (e) closed state (f) with its open and (g) closed electrical representations.

The MEMS is open by default. Applying an 82 V (MEMS bias voltage) induces an electrostatic force that closes the switch by mechanically moving the actuator to create a short circuit between the gate and the beam electrodes of the MEMS. Removing the MEMS bias voltage, the actuator moves again to open the circuit. MRI applications in this work required the addition of a driver circuit and external power sources to control MEMS opening and closing since those control signals were not readily available on the used MR scanner. However in certain recent MR scanners from GE, these signals are made available easing the use of MEMS.

**Table 1-1.** Characteristics of MEMS switch developed by GE Healthcare Inc.

| MEMS characteristics | Typical values |
|---|---|
| Control voltage (v) | 82 |
| Control current (pA) | 10 |
| Standoff voltage (V) | 500 |
| Capacitance of open MEMS CAB (pF) | 1.5 |
| Resistance of open MEMS RAB (MΩ) | 10 |
| Resistance of closed MEMS RAB (Ω) | 0.5 |
| Switching delay to open the MEMS (µs) | 1 |
| Switching delay to close the MEMS (µs) | 4 |

## MEMS driver

The MEMS Driver Circuit houses three Inputs: two DC bias inputs for an 82 V and 10 V voltages to bias, respectively, the MEMS and its driver, and a DC control input which is fed either -5 V voltage to set the 82 V on the gate-electrode of the MEMS and close the MEMS or a 7 V (100 mA) signal to release the switch and open the MEMS. More details about the MEMS and its driver were provided in previous work [69]. The MEMS and its driver are presented in Fig. 1-13. The MEMS Driver Circuit houses three Inputs: two DC bias inputs to receive 82 V and 10 V voltages to bias, respectively, the MEMS and its driver, and a DC control input to receive a -5 V voltage to set the 82 V on the gate-electrode and closes the MEMS or a 7 V (100 mA) signal to release the switch and opens the MEMS. More details about the MEMS and its driver were provided in previous work [69].

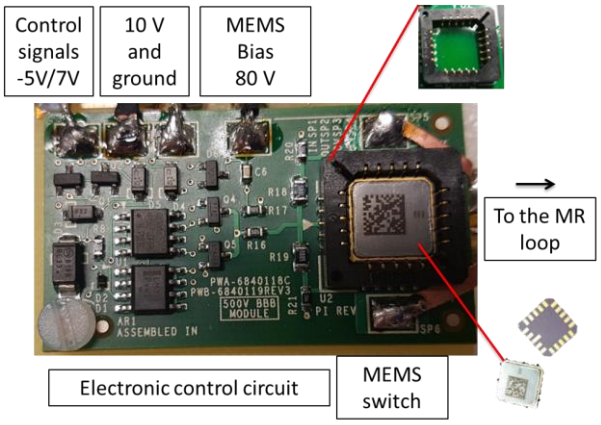


**Fig. 1-13.** The picture of MEMS driver circuit (MDC) including the MEMS switch (GE Healthcare Inc.). The dimension of the board circuit are of 4.4 cm x 2.2 cm.

To avoid redundancy, more details about the characteristic and operating of MEMS switch and board (control) are described in chapter 2.

Once the MR signal is formed according to the NMR phenomenon, detected by an RF coil (respecting the decoupling strategy) and transmitted to the MRI system by a line transmission, MR images are reconstructed. Thus, the MR image quality should be evaluated.

## 1.6. MR image quality

After an MRI examination, the diagnosis efficacy depends mainly on the image quality whose two major characteristics are namely spatial resolution and SNR parameters [70]. They can be completed by other characteristic such as the contrast to noise ratio or signal intensity uniformity.

The SNR is a measure used to quantify the image quality. One definition is given by the ratio between signal levels in a region of interest with respect to the standard deviation of the noise level which is measured outside the sample (in air). For MRI applications, the SNR can be defined as the ratio between the induced MR-signal (maximum signal amplitude) and the thermal noise voltage [71], [72].

The noise observed on MR images is reflected in an identical manner on the signal of each voxel due to the invariance of the noise voltage at any point in space. It can be related to the RMS amplitude of the thermal noise voltage ($V_{Noise}$) measured across the equivalent (total) noise resistance ($R_{Noise}$) of the loaded MRI coil [73]. The $V_{Noise}$ is given by:

$$V_{Noise} = \sqrt{4kT\Delta f R_{Noise}} \tag{0.10}$$

where $\Delta f$ is the reception bandwidth and $T$ is the coil-loop temperature. Thus, the SNR of an NMR experiment is given by [73]–[76], [51]:

$$SNR = \frac{peak\ signal}{RMS\ noise} = \frac{\omega_0 M_0 V_s}{\sqrt{4kT\Delta f}} \frac{\frac{B_{1xy}}{I}}{\sqrt{R_{Noise}}}\ \alpha\ \frac{B_{1xy}}{I\sqrt{R_{Noise}}} \tag{0.11}$$

where $\omega_0$ is the nuclear precession pulsation (rad/s), $V_s$ is the sample volume, $k$ is the Boltzmann constant, $T$ is the absolute temperature, $\Delta f$ is the receiver bandwidth and $M_0$ is the magnetization (magnetic moment per unit volume) which is given by:

$$M_0 = \frac{N\gamma^2 \hbar^2 I(I+1)B_0}{3kT} \tag{0.12}$$

where $N$ is the spin density, $\gamma$ is the gyromagnetic ratio, $I$ is the spin quantum number, $\hbar$ is the Planck's constant divided by $2\pi$ and $B_0$ is the static magnetic field.

The $\frac{B_{1xy}}{I}$ term is the magnetic field per unit of current flowing in the coil and represents the coil sensitivity. Assuming a $B_0$ aligned along the z-direction, $B_{1xy}$ is given by [77]:

$$B_{1xy} = \sqrt{B_{1x}^2 + B_{1y}^2} \tag{0.13}$$

where $B_{1x}$ and $B_{1y}$ are then the field components orthogonal to $B_0$.

So, optimizing $\frac{B_{1xy}}{I\sqrt{R_{Noise}}}$ leads to optimize the coil performance. The loss phenomenon which is associated to the thermal energy dissipation $R_{Noise}$ represents an important factor to be determined. More details about this particular are provided in the chapter 3.

**SNR optimization**

The SNR can be optimized by increasing $B_{1xy}$ or decreasing $R_{Noise}$. Increasing the static magnetic field $B_0$ induces an increase in the Larmor frequency $F_0$ which in turn leads to an increase of the signal quantity ($B_{1xy}$) and SNR. However, $R_{Noise}$ also depends on the frequency (detailed in the chapter 3). In addition, the noise origins are multiple. In this context, numerical electromagnetic simulations are required to achieve the optimal geometry design.

# 1.7. Numerical Electromagnetic simulations

Computational electromagnetic (EM) simulation techniques based on solving Maxwell's full-wave equations, such as Finite-Element Method (FEM) [78], Finite-Difference Time Domain (FDTD) [79], [80], and Method of Moments (MoM) [81], [82], have been reported in the literature. They all enable calculation of the sensitivity of various coil geometries designed for specific regions of interest [83] with numerical results being very close to those of experimentation [84]. This is very helpful for coil designing and building in terms of cost, time, effort and efficacy [84]. Overall, these numerical solvers can be classified in two categories: partial differential-equation or integral-equation techniques.

## 1.7.1. Partial differential-equation techniques

This section is devoted to the presentation of the two numerical solvers category based on partial differential equation techniques: Finite-Difference Time-Domaine (FDTD) and Finite Element Method (FEM)

### Finite-Difference in Time-Domaine (FDTD)

FDTD is a numerical technique used a field method to solve Maxwell equations directly in their partial differential-equation and the solution is found in the time domain (particularity of this technique) [80]. After the discretization into appropriately sized unit cells, an excitation source should be applied under form of currents or plane wave. At any point in space, the updated value of the E-field in time is estimated from both local H-field and previous E-field value. Thus, electric and magnetic fields are determined in a meshed parallelepiped volume, and at any given instant in time and space [84]. If the FDTD technique is set in the time domain, the use of Fourier techniques allows the calculation of wide-band frequency domain information. This method is well-suited to modelling inhomogeneous materials. More details about this method can be found in the literature [80], [84]–[87].

### Finite Element Method (FEM)

FEM is a numerical technique used to solve Maxwell equations using differential equation technique and consisting in finding approximation of the solution in frequency domain [88], [89]. In fact, the computational domain is discretized on finite elements (hence its name) which are small sub-domains represented by triangular elements (the triangle is the element while the points defining the triangle are called nodes) in the case of 2D modelling and by tetrahedral or hexahedral elements in the case of 3D modelling (the FEM is a volume meshing technique permitting an accurate mesh for arbitrarily shaped volumes). The solution accuracy depends on the order of the polynomials of the interpolation functions [90]. The numerical solution is obtained by solving a system of linear equations formed by an integro-differential formulation. The FEM is well-suitable for modelling of electrically large or inhomogeneous dielectric bodies (not efficiently solved with MoM). More details about this method can be found in the literature [84], [91].

## 1.7.2. Surface integral technique

The Method of Moments is a surface integral technique widely used in the literature and the next paragraph will be devoted to a brief presentation of the technique.

### Method of the moments (MoM)

This technique forms the basis of the FEKO solver and represents the core of the FEKO program. In fact, MoM is a full wave solution of Maxwell's integral equations in the frequency domain for obtaining directly the induced current (or charge) density [84],

[88], [89]. In other words, it is a source method (and not a field method), and the integrand itself is an unknown to be solved [92], [93].

To estimate and evaluate the currents, MoM discretizes only the surface of the objects under investigation. In fact, MoM mainly uses triangular[5] mesh elements for modeling such surface geometries [92], [94]. For that, wires and conducting surfaces are discretized into segments and small triangular elements, respectively [92]. Also, MoM can use local or volume meshes for dielectrics which is very important to get a different mesh from that of metallic surfaces to reduce the simulation time with accurate mesh of dielectric parts [95], [96]. Then, associated surface current distribution on the discretized portions can be determined after applying an arbitrary excitation source. From the obtained currents, fields are then post-processed and can be derived (indirectly)[6].

Since the MoM is a source method, only the structure is discretized and not free space as with other techniques based on field methods. Boundary conditions do not have to be set. The memory requirement scale is proportional to the geometry and the required solution frequency. With MoM, it is possible to choose surface (SEP) or volume equivalent principle (VEP) (*http://www.altair.com*).

**Surface equivalent principle (SEP)**

The SEP introduces equivalent electric and magnetic currents on the surface of a dielectric body arbitrarily shaped. The discretization is based on triangular elements.

**Volume equivalent principle (VEP)**

The VEP allows the creation of dielectric bodies and is associated with a volume mesh. This method is well-suited to inhomogeneous and thin dielectric bodies.

[5] MoM can employ other mesh elements such as tetrahedral or quadrilateral.

[6] The current on each portion is then decomposed into a linear combination of basic functions. The use of the Green function serves to link the electric field at an arbitrary observation point to the current at the source point leading to formulate an integral equation which defines the electric field resulting from an arbitrary excitation source (the applied voltage source is equivalent to setting up an incident E-field). Basis functions are used to expand the current distribution, and testing functions are used to enforce the electric field boundary condition on the discretized parts leading to create a system of simultaneous linear equations. After testing each basis function, integral equations are transformed into a matrix equation with the unknown being the currents on the coils and then fields can be derived.

### 1.7.3. MoM vs FEM vs FDTD

As seen in the previous section, Both FEM and FDTD are partial differential-equation techniques while MoM is a surface integral-equation technique.

Overall, both FEM and FDTD consists in discretizing the region to be analyzed into volume elements and cells while MoM consists in discretizing all wires into segments and only the object surface into small triangular elements. In addition, FEM or FDTD use volume discretization of the entire problem domain by the use of tetrahedrons or grid-based cubical Yee cells for discretization, respectively.

Another main difference between these methods is that the FDTD is a time-domain based simulation technique while both FEM and MoM are mainly based on frequency domain simulations [92], [97].

MoM has an advantage of a smaller matrix size compared to the FEM and FTDT [95] thanks to the smaller number of surface-only mesh elements and hence the reduced number of unknowns [94]. However, a main limitations and challenges of MoM based solution are related to the simulation time and memory [92], [95] due to Green's Function interactions [98] which leads to get a dense matrix [94]. In brief, MoM matrices are smaller due to surface-based discretization but dense, which presents a time and memory bottleneck [97].

MoM is well-suited for modeling complex coil structures and is often used to model resonant antennas. However, this technique is not as well-suited to model complex and complicated biological tissue loads, particularly in the case of inhomogeneous dielectrics due to its requirement to use a complicated Green’s function [99].

On the other hand, FDTD and FEM are well-suited for modeling complex geometries based on inhomogeneous dielectrics [92]. However, they have a limitation of the capability to model such coil structure [100]. In addition, since FEM and FDTD are volume-based methods, they require the source and solution regions to be volumetrically discretized for getting a correct evaluation of fields at desired locations and thus this results in large number of variables (especially for large geometries). A mesh is necessary for the entire volume to be analyzed and this requires the use of absorbing boundary elements at the outer surface of the meshed region in order to model unbounded geometries [101].

To conclude, surface integral and partial differential equation techniques are complementary and combining them in the same software (hybrid numerical electromagnetic modeling techniques) can lead to interesting results in the case of

specific applications [101]. The main focus of this solution is the MRI RF coil modeling and electromagnetic fields calculation [84].

There are a large number of commercial electromagnetic simulation tools on the market that use either of the solving methods. Each requires a period of training and consequent mastery. In this thesis, the choice fell on FEKO using MoM as the computational method, for providing current distribution and thus magnetic field which is the variable that we seek [7], [26]–[28].

Because we focus on the comparison of several coil-loops having different geometries and different number of conductors, the losses effect must be taken into account and estimated. These losses are represented by the calculation of an equivalent resistance ($R_{Noise}$) which must therefore be estimated.

## 1.8. Loss effect estimation

The coil performance can be analyzed and optimized with the coil sensitivity through the $\frac{B_{1xy}}{I}$ ratio. However, the comparison between different coil geometries requires the introduction of total loss resistances $R_{Noise}$ of each geometry. Since the coil has a huge impact on the image quality reconstruction and since the SNR includes the $R_{Noise}$ effect in its expression, the SNR distribution can be used to analyze and optimize the coil design. As seen in the chapter 1, the proportional SNR term is given by the following relationship [29], [73], [102]:

$$SNR\ \alpha\ \frac{B_{1xy}}{I\sqrt{R_{Noise}}} \tag{0.14}$$

To simplify the notation, the $B_{1xy}$ is often noted $B_1$ and represents the generated transverse magnetic field $B_1$. In the objective of estimating $R_{Noise}$, we present below a brief theoretical description of the $R_{Noise}$ sources.

The combination of the coil and sample introduced inside an MRI system leads to create some phenomena responsible for generating the noise voltage and thus $R_{Noise}$ which affects the SNR and degrades the image quality. Each source represents a parasitic resistance (dissipating the electric power) which describes the noise magnitude related to such physical phenomenon [103].

As seen in Fig. 1-14, noises are related to: RF-loop, electrical components, radiations and sample (magnetic & dielectric losses).

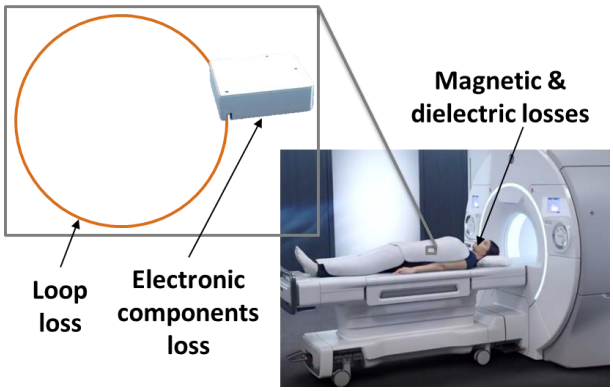


**Fig.1-14.** Noise sources in an MRI experiment.

## 1.8.1. Coil-loop loss

Two main effects participating in increasing the $R_{Noise}$ are related to the coil loop itself: skin effect (losses in loop conductors) and proximity effect (losses to neighboring conductors).

### Skin effect

The skin effect is related to the losses in loop conductors due to increased electrical resistance at high frequencies. This is due to the concentration of current on the surface of such conductor (i.e. the skin depth). Losses within conductors depend on the conductor geometry: wire or rectangular types.

In the case of copper wire-conductors (round section), the skin depth $\delta$ can be approximated by (Fig. 1-15):

$$\delta = \sqrt{\frac{1}{\pi f_0 \mu_0 \sigma}} = \sqrt{\frac{\rho}{\pi f_0 \mu_0}} \qquad (0.15)$$

Where $f_0$ is the frequency, $\mu_0$ the free space permeability ($4\pi\,10^{-7}\,H/m$), $\sigma$ is the conductor conductivity ($0.596\,10^{8}\,m^{-1}.\Omega^{-1}$ for copper) and $\rho$ is the conductor resistivity ($1.68\,10^{-8}\,m.\Omega$ for copper). Table 1-2 illustrates some examples of skin depth values for different specific frequencies ($^1$H nucleus / copper).


**Fig. 1-15.** The skin depth ($\delta$) in such copper wire-conductor with (left) $f_0 = 0$ and (right) $f_0 \neq 0$. Its value decreases with the frequency [104].

**Table 1-2.** Examples of skin depth values for different frequencies (proton/copper).

| skin depth ($\delta$) | 64 MHz | 128 MHz | 200.2 MHz |
|---|---|---|---|
| $^{1}$H | 8.1 µm | 5.8 µm | 4.6 µm |

The conductor section in which the current flows is inversely proportional to the frequency. The skin effect increases the coil-loop electrical resistance and thus the voltage noise.

As a first approximation, the current is taken to be uniformly distributed over the surface, it is then possible to calculate analytically the electrical resistance $R_{el}$ per unit length. In the case of wires, when $\boldsymbol{r_{wire} \gg \delta}$ (which is a reasonable assumption at our frequencies) [105] it is given by the following relationship:

$$R_{el} \equiv \frac{1}{2\pi r_{wire}} \frac{1}{\delta\, \sigma} = \frac{1}{4\pi r_{wire}} \sqrt{\frac{2\,\pi\, f_0\, \mu_0}{\sigma}} \qquad (0.17)$$

where $r$ is the wire conductor radius.

However, the current is not uniformly distributed over the surface in the case of strip conductors (rectangular sections); thus analytical calculations of the electrical resistance $R_{el}$ are not available. In this case, numerical calculations based on the use of electromagnetic simulation software are required but in general, the electrical resistance $R_{el}$ decreases by increasing the strip-width or the thickness of strip conductors [106].

### Proximity effect

The proximity effect appears in the case of a coil designed with several neighboring conductors through which flows an alternative current. The distribution of the latter on such conductor is affected by the magnetic flux produced by the adjacent (neighboring) conductor, as well as the magnetic flux produced by the current in the conductor itself. This leads to an added resistance. However, it is difficult to determine this resistance by analytical calculations in particular for complex geometries. Numerical calculations using electromagnetic simulation software is then the solution for that.

For example, a previous work [106] has evaluated the proximity effect between two layers (two loop connected in parallel and printed on FR4 substrates with thicknesses of 0.8 mm then 1.6 mm). Results show that electrical resistance decreases with the substrate thickness (by a factor of 1.73 and 1.88 for, respectively, 0.8 mm and 1.6 mm,

regarding a single loop). This is due to the diminution of the proximity effect between the layers.

## 1.8.2. Sample loss

Sample losses ($R_{sample}$) origin is related to RF currents in the sample (phantom or patient), induced by the fluctuating magnetic field and by electric fields in the sample; mainly generated by the coil capacitors [107]. So, the presence of the sample close to the coil causes magnetic and dielectric sample losses [108], [109].

### Magnetic losses

Magnetic losses are related to the circulation of magnetic field lines which causes eddy currents in a sample having non-zero conductivity. In other words, they are related to the sample electrical conductivity affected by the alternative field produced by the coil leading to create Eddy currents in the sample and thus to an additional power dissipation by Joule effect which increases the total loss resistance [110]. Magnetic losses on the sample increase with ${w_0}^2$. Magnetic losses resistance can also be estimated by the electromagnetic simulations. In fact, unloaded and loaded coil quality factors ($Q_u$ and $Q_l$) can be determined to estimate the magnetic resistance through the following relationship:

$$R_m = \frac{1}{w_0 C_t}\left(\frac{1}{Q_l} - \frac{1}{Q_u}\right) \tag{0.18}$$

### Dielectric losses

Dielectric losses are related to the dielectric properties of the sample. In fact, a distributed capacitor between the coil and the sample leads to capacitive losses from the coil-inductance to the sample then to the ground [28]. In this case, the electric field lines passing through the sample material causes energy dissipation (lossy capacitor) due to the sample resistance [30]. In other words, this represents an additional dielectric resistance which leads to increase the total loss resistance [76]. Since dielectric loss resistance depends mainly on the coil environment, it is difficult to be estimated. However, it is possible to reduce them using a distributed tuning [28], [111] and keeping the sample as far away from the ground plane as possible.

## 1.8.3. Lumped elements loss

Electronic circuits based mainly on tuning, matching and decoupling lumped components (such as capacitors, PIN diodes, …) cause some additional losses that are not negligible as it can be seen in the following example.

### 1.8.4. Radiation loss

Generally, radiation losses are negligible compared to coil and sample losses.

### 1.8.5. Example of total loss in MRI experiments

To give a quick overview, a previous work [112] detailed the power flow of unloaded and loaded two channel receiver surface coil (dimensions of 9.5 cm x 6.0 cm) for a frequency of 63.65 MHz, as shown in Fig. 1-16. The coil is positioned with a curvature of 12.7 cm radius on a cylindrical phantom (12.7 cm diameter and 15.24 cm height) characterized by a 72.3 electric permittivity and 0.69 S/m conductivity. By exciting only one channel (about 1 W incident power), losses of conductors, total lumped elements and radiation represent, respectively, 40%, 58% and < 1% in the case of unloaded coil. In the case of loaded coil, losses of conductors, total lumped elements, radiation and the sample losses represent, respectively, 12%, 18%, <1% and 68%. It should be noted that these percentages depend on the coil size and geometry and the nature of the load (sample), as well as on the frequency (Fig. 1-17). In fact, loss resistance associated with conductors, lumped elements, radiation and load depend on the operating frequency with $\sqrt{\omega_0}$, $\omega_0^{0.45}$, $\omega_0^4$ and $\omega_0^2$, respectively.

This was a general example reported in the literature. However, losses related to our application are evaluated experimentally (chapter 2) through their effect on quality factor (characterization on bench) and through the MR image (imaging conditions). Then, losses are evaluated by EM simulation run with FEKO software (chapter 3) where we focused on the impact of the electrical resistance of the isolated (unloaded or in vacuum) coil and magnetic resistance of the sample (phantom losses) as noise sources [106], [113], [114]. Losses of loaded coil (coil & phantom) represent the total equivalent resistance in series with the coil inductance.

Since the quality factor Q is one of most important quantity used to test the coil performance, an idea is to derive $R_{Noise}$ from the simulated or measured Q-factors. More details about that are described in the next chapters.

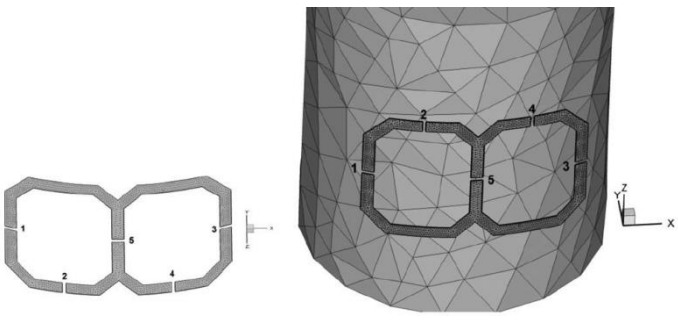

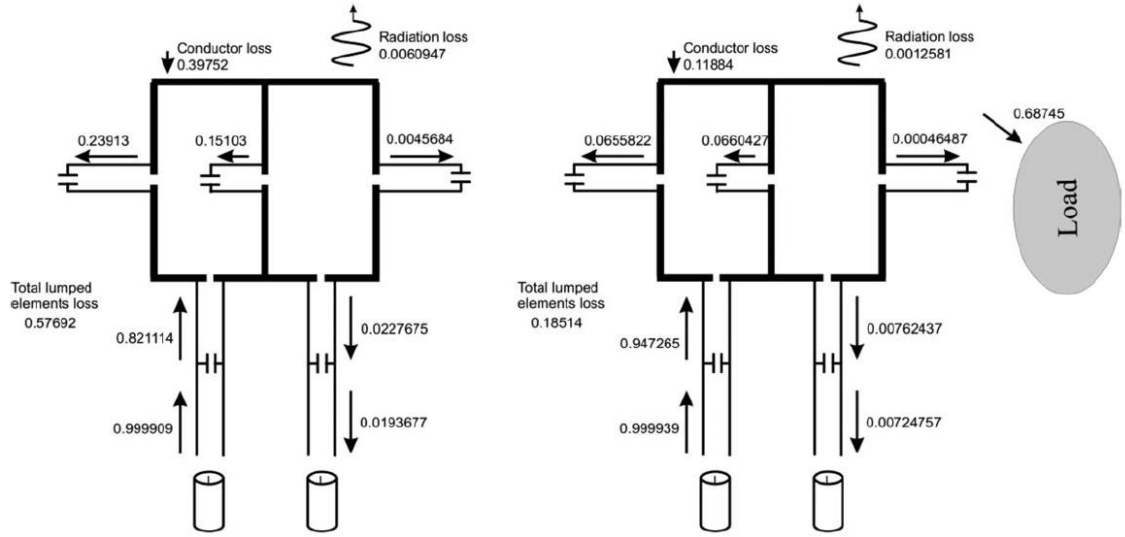


**Fig. 1-16.** Example of (first line) unloaded and loaded two channel RF surface coil and (second line) associated noise sources [112].

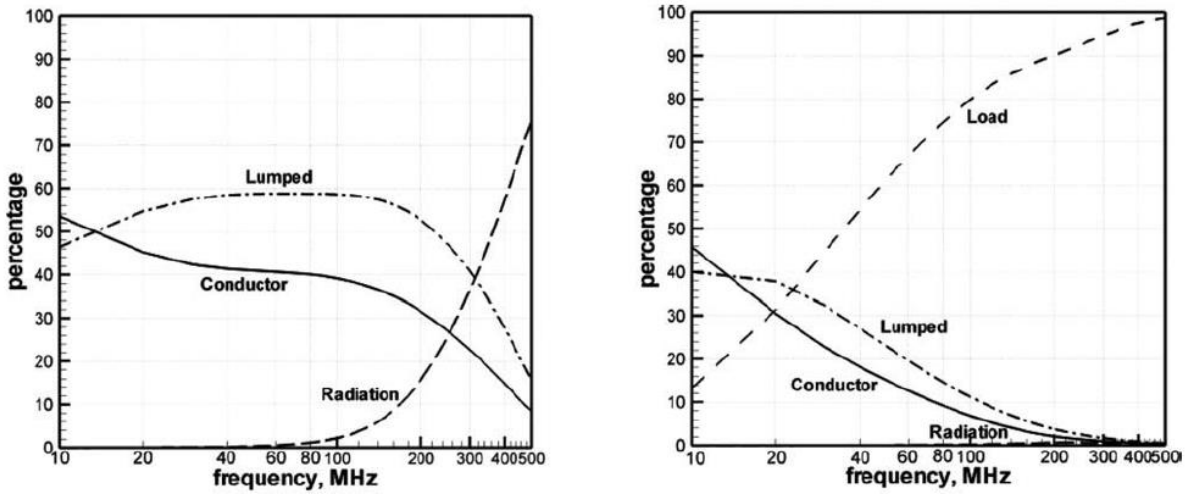


**Fig. 1-17.** Losses and frequency dependence for (left) unloaded and (right) loaded coil [112].

## 1.9. Chapter conclusion

The chapter contains main information necessary to handle original work carried out in this thesis and focusing on the potential use of MEMS switches to reconfigure endoluminal coil-geometry according to its orientation with respect to $B_0$ while also fulfilling the active decoupling of receiver endoluminal coils. The assessment of active decoupling performances using MEMS switch technology in the specific case of endoluminal coils is presented in the next chapter.

# Chapter 2: Serial and Parallel Active Decoupling Characterization Using RF MEMS Switches for Receiver Endoluminal Coils at 1.5T

# Chapter 2

# Serial and parallel active decoupling characterization using RF MEMS switches for receiver endoluminal coils at 1.5T

## Contents

*This chapter details the first thesis axis related to the assessment of the active decoupling of one-channel endoluminal coils based on two different configurations using MEMS switches and the comparison with other technologies (PIN diode, array coils and whole body coil) and corresponds to an accepted journal article :* "Serial and parallel active decoupling characterization using RF MEMS switches for receiver endoluminal coils at 1.5 T", Hamza Raki, Kevin Tse Ve Koon, Isabelle Saniour, Henri Souchay, Simon A. Lambert, Fraser Robb and Olivier Beuf; and which has been published in IEEE Sensors Journal, May 2020, DOI: 10.1109/JSEN.2020.2995055, vol. 20, no. 18, pp. 10511-10520. This may be used for non-commercial purposes.

# 2. Serial and parallel active decoupling characterization using RF MEMS switches for receiver endoluminal coils at 1.5 T

## Abstract

MEMS (Micro Electro Mechanical System) switches were assessed and compared to PIN diode in fulfilling the task of active decoupling of Receiver Endoluminal Coils (RECs). Three prototype RECs with the PIN diode in parallel (pPIN), MEMS in parallel (pMEMS) and MEMS in series (sMEMS) with the REC loop were built. Quality factors (Q-values), decoupling efficiency and switching delays were characterized on bench and Signal-to-Noise Ratios (SNRs) established on images at 1.5 T. Q-values were equal to 62.5, 41.2 and 65.1 for pPIN, sMEMS and pMEMS, respectively. In the decoupled state, reflection coefficients S11 and S21 at resonance frequency both indicated proper decoupling. Switching delays were less than 0.7 µs and 10 µs for pPIN and MEMS RECs, respectively. Decoupling/coupling delays of MEMS remained compatible with most Magnetic Resonance (MR) clinical applications. For all prototypes, MR images displayed no signal saturation and similar elliptical image sensitivity patterns. No artifacts due to active decoupling failure were observed. Mean SNR values obtained with pMEMS REC were higher than those obtained with sMEMS REC but lower than with pPIN REC because of the use of additional instrumentation to render the scanner compatible with the MEMS utilization. MEMS in parallel are an interesting alternative to PIN diode for decoupling and could lead to better SNR with a compatible MR system (dedicated control signal). The MEMS in series can be used for both decoupling and reconfiguration of the REC loop geometry for colon wall examination. **Index Terms**— Active decoupling, endoluminal coils, MEMS, MR switch.

## 2.1. Introduction

Magnetic Resonance Imaging (MRI) is a common modality used for medical diagnosis of abdominal and intestinal diseases. In the case of colorectal cancer, which is one of the most frequent and fatal cancers worldwide [115], [11], [116], [10], [117], colonoscopy investigation remains the gold standard. One intrinsic limitation of this optical imaging technique is the low penetration depth, which can result in tumor growing within the bowel wall being detected only at a late stage. This limitation could be overcome by a high spatial resolution (in-plane pixel size <100 µm and 2-mm slice thickness) MRI examination.

MR arrays of external receiver radiofrequency (RF) coils are commonly used for abdominal imaging with improved Signal-to-Noise Ratio (SNR) owing to the combination of small surface coils that provide higher sensitivity [118]–[120]. Unfortunately, the gain in SNR is not sufficient to depict the thin bowel and colon wall in deep regions located relatively far from the body surface, thus making analysis of the colon wall and subsequent colorectal cancer staging difficult.

For this purpose, early works [106], [121], [122], [77] have demonstrated the feasibility and value of Receiver Endoluminal Coils (RECs) close to the region of interest (ROI). A simple REC design consists of a very small surface coil with an adapted size and geometry so as to fit the lumen being investigated. In the case of colon examinations, the favored geometry is a rectangular loop with a width somewhat smaller than the diameter of the colon. In this configuration, the REC displays a cylindrical sensitivity pattern (with respect to its long axis) with a very high SNR close to the loop, enabling a decreased voxel size. The sensitivity decreases rapidly with the distance to the long axis [26] which is, however, sufficient to enable high-resolution imaging of the first centimeters of the colon wall and thus visualization of its different layers. RECs have been used *in vivo* on rabbit [123] and mouse [124], [125] colon walls. The REC is used in combination with the whole-body RF transmitter coil in order to provide a well-transmitted RF pulse uniformity over the imaging volume [107]. Both coils must hence be decoupled during the transmission phase in order to avoid any mutual induction and the subsequent non-uniform $B_1$ magnetic field in the vicinity of the receiver loop coil. Therefore, a decoupling circuit is mandatory to avoid uncontrolled and spatially dependent image contrast. Another negative consequence is the local increase in the Specific Absorption Rate (SAR) that could lead to patient safety problems [126].

To this end, several electronic switching components enable this active decoupling. PIN

diodes are the most popular components used as RF switches in the majority of clinical systems. The main advantages are their compatibility with a magnetic environment (non-magnetic packaging), the small size (a few millimeters) and a switching delay below 1 µs.

Other components such as MR-compatible memory resistive elements (Memristors) have been used [127]. The principle resides in applying different DC control voltages to switch between two resistive states during transmit and receive modes. The particularity of this technology is that the Memristor, unlike the PIN diode, can memorize and retain the resistive state information after the control signal is removed. It is particularly relevant in multinuclear MR coils. Other methods based on optical components have been proposed in the literature mainly founded on photoelectronic devices such as the photoresistor [128], photodiode [129], [130], combined photodiodes and a PIN diode [131], PhotoMOS [132], or MOSFET with optically isolated [133] devices. The optical decoupling solutions have the advantage of using nongalvanic transmission means thereby avoiding induced current in the shield and increasing patient safety [37]. Finally, low noise preamplifiers have been used for the decoupling between loops of the coil in the case of multiple-element array coils [134]–[136].

A few years ago, Micro ElectroMechanical System (MEMS) switches were introduced by GE Healthcare, Inc. [68] to act as MR-compatible switches (Fig. 2-1a and b). As can be seen in Figure 1 (c and d), the MEMS as a switch has two working states: open and closed. The open state electrically corresponds to a small capacitance (1.5–2 pF). The closed state is electrically equivalent to a very small parasitic resistance (0.5–1 Ω). Owing to their high electrical isolation (approximately 10 MΩ) and their MR compatibility, MEMS ("MEMS" will be used to denote "MEMS switch" hereafter) were successfully used as switches. MEMSs were used to open or close portions of metallic conductors for rapid reconfiguration of external two-channel array coil geometry as was done for spine and torso MRI [63]. MEMSs have also been used as an alternative solution to the traditional passive decoupling strategy in the case of double-tuned RF coil designs used, for example, for sodium imaging. A proton coil is still required for co-registration purposes and the decoupling of the coils is performed with MEMSs by shifting the resonance frequencies. The MEMS-based solution demonstrated comparable results to the PIN diode and better performance than the trap circuit [64]. In the same context, a study based on four-element fixed phased transmit–receive coils used MEMS to switch between 1H (64 MHz) and 19F (60 MHz) resonance frequencies for lung imaging [65]. In a design of integrated parallel reception, excitation and shimming coil arrays, MEMSs were used to reduce the cost and complexity of the design by employing a single DC supply with an

adaptive distribution of the DC current (instead of using "N" DC supplies for "N" shim loops) and thus achieving high RF shimming performances (high localized $B_0$ homogeneity) with no SNR loss [66]. Finally, MEMSs were also used for both the control of an array of primary coils and the automatization of the impedance matching network of an MRI-compatible wireless power transfer system used on a wearable wireless receive coil array [67].

Endoluminal MRI using RECs could also benefit from the use of MEMSs for the active decoupling while additionally enabling reconfigurable REC geometries [137]. In this work, we focus on studying the feasibility of using a MEMS as an active decoupling element. This is an interesting question considering the very small size of the REC loop and therefore its resulting small electrical resistance with respect to that of the MEMS. Since the impact of MEMSs used in parallel to the loop (the MEMS is similar to either an additional capacitor or a short circuit shifting the REC resonance frequency) is not the same as the impact of the MEMS used in series with the loop (the MEMS is similar to either an additional parasitic resistance or an open circuit in the REC loop), we first tested the two configurations not only in terms of active decoupling performance but also in terms of an active image quality to detect the performance advantages and drawbacks of each configuration.

This manuscript presents the first step of our project. For this purpose, two RECs with active decoupling circuits using MEMS placed in series or parallel to the loop were assessed and compared with a reference REC using a conventional PIN diode. All RECs were characterized on experimental benches, in both coupled and decoupled states. Tuning, matching, quality factor and isolation (decoupling efficacy) were measured. Switching delays to couple or decouple the REC were also estimated. Finally, the three RECs were tested in imaging conditions on a 1.5-T MR system. SNR mean and distribution were measured to assess differences on the acquired image.

# 2.2. Materials and Method

## 2.2.1. REC prototypes

In this study, three copper RECs with identical rectangular loop geometries were mechanically etched on an FR4 epoxy substrate of 1.6-mm thickness (S63, LPKF Laser and Electronics, Germany). Each REC consisted of a single rectangular loop (5.1-mm width, 47-mm length and 35-µm copper track thickness). In order to operate with a 1.5-T MRI system, fixed capacitors (ATC, New York, USA and Temex Ceramics Exxelia,

Pessac, France) were soldered in the proximal side to match 50 Ω and in the distal position to tune the loop to the working proton resonance frequency (63.87 MHz).

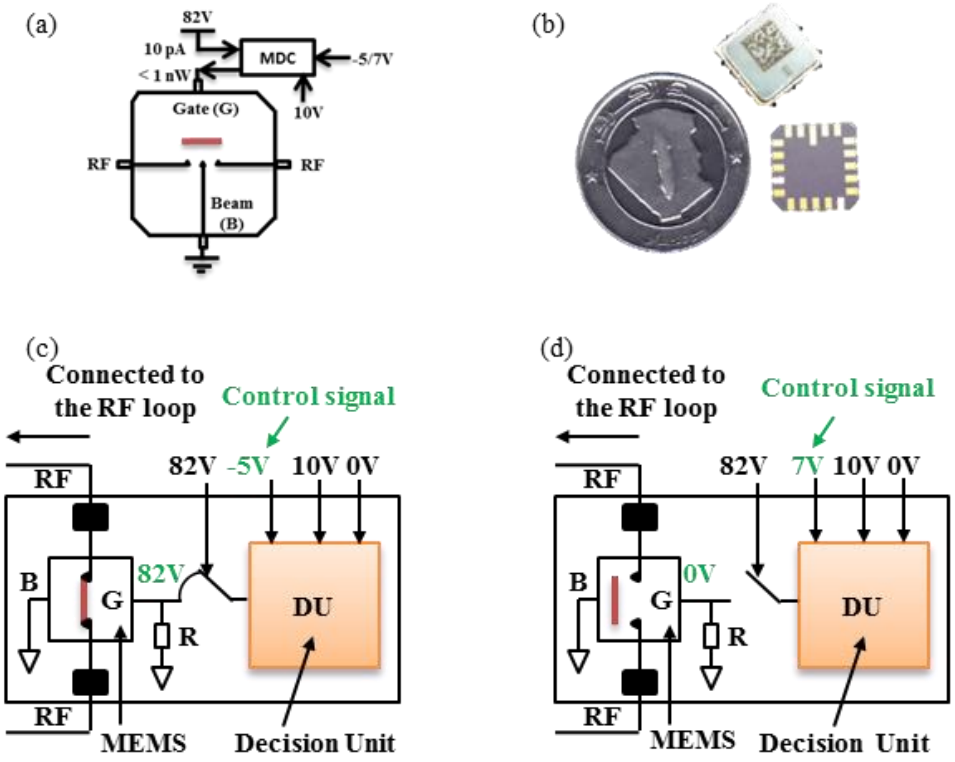


**Fig. 2-1.** *Description of MEMS switch and its driver. (a) Scheme of the controllable RF MEMS switch developed by GE Healthcare Inc. (b) Photograph of the 1 cm × 1 cm chip package of only the MEMS switch with 1 Algerian dinar coin. Second line shows two small diagrams of the MEMS and its driver circuit (MDC). The MDC consists of an electronic Decision Unit (DU) biased with 10 V and 0 V input voltages and allowed to compare a predetermined threshold voltage to the control signal. (c) If the DU receives a control signal of -5 V, an external 82 V (typical value) is delivered between the gate (G) and beam (B) electrodes of the MEMS thereby closing the switch. (d) If the DU receives a control signal of 7 V (or 100 mA delivered by the MRI system), the external 82 V is blocked and cannot be delivered to the MEMS gate. In this case, 0 V is delivered between G and B thereby opening the switch.*

MEMS switches (MM7100, Menlo Microsystems, Inc., Irvine, CA, USA) were used in this study to couple or decouple the REC during endoluminal MRI. The MEMSs used are fast mechanical switches based on a mobile micro metallic actuator (Fig. 2-1a) inside a chip of 1 cm × 1 cm size (Fig. 2-1b). The MEMS is open by default and to close it, sufficient voltage (in our case, the typical value was 82 V) has to be applied between the gate (G) and the beam (B) of the MEMS. For our MRI application, since the MR system was not able to deliver these voltages, a driver circuit supplied the required voltage to open or close the MEMS so as to achieve the coupling/decoupling of the REC. As can be seen in the two schematics of the MEMS Driver Circuit (MDC) in Fig. 2-1c,d, the MDC consists of

an electronic decision unit (DU) and is equipped with four inputs. Three of them are used to receive continuously the required bias voltages: 0 V as ground, 10 V as bias voltage of the DU and 82 V to close the MEMS switch. The last input receives the control signal and directs it to the DU, which compares it to a predetermined threshold voltage leading to the delivery or blocking of the 82 V to the gate of the MEMS. Applying a -5 V control signal to the DU delivers the 82 V to the MEMS gate (G) and thus closes the MEMS switch (Fig. 2-1c), while a 7-V voltage (which is equivalent to a current of 100 mA provided by the MRI system) leads to 0 V being applied between G and B and thus opens the switch (Fig. 2-1d). More details about the MEMS and MDC information were provided in previous work [138].

To evaluate the MEMS performances for active decoupling of RECs, two different active decoupling REC configurations with MEMS in series (*s*MEMS REC) and MEMS in parallel (*p*MEMS REC) to the loop were built and assessed. In the *s*MEMS REC configuration (Fig. 2-2a,d), the MEMS switch was integrated into the loop (in series with the tuning capacitor Ct). During transmission, the MEMS must be open (REC is not resonating). In the *p*MEMS REC (Fig. 2-2b,e), the switch was integrated in parallel to the tuning capacitor Ct. During transmission, the MEMS must be closed to shift the resonance frequency and thus detune the REC. In addition, a third REC was built with a conventional decoupling circuit using a PIN diode component (DH 80055, Temex Ceramics, Pessac, France) placed at a distal position in parallel (*p*PIN REC) to the tuning capacitor (Fig. 2-2c,f). The PIN diode was controlled using a forward biased voltage of 3.8 V (which is equivalent to a current of approximately 100 mA provided by the MRI system). A summary of tuning and matching capacitor values used to build the different RECs is given in Table 2-1.

REC prototypes were characterized on two experimental measurement benches as well as by imaging using a phantom made of a cylindrical vessel (90 mm outer diameter, 100 mm long) filled with a solution of 1.25 g $NiSO_4 \times 6H_2O$ + 5 g NaCl per liter of distilled water mimicking tissue losses and with a through-hole (11 mm inner diameter) allowing for the introduction of the REC loops (Fig. 2-3). For ease of use, three identical phantoms were built, one for each REC prototype.

### 2.2.2. Experimental bench characterization set-up

Two complementary experimental electronic benches were used to assess the frequency and temporal responses of the different REC prototypes. Each REC was first connected to a Vector Network Analyzer (VNA) (Agilent Technologies Inc., E5071C, Santa Clara, CA, USA) to measure the reflection coefficient $S_{11}$ in both coupled and decoupled states

(Fig. 2-4a,b). In the coupled state, the reflection coefficient response ($S_{11}$) enabled tuning and matching of each REC at the Larmor resonance frequency ($F_0$) by choosing the adequate tuning and matching fixed capacitors. Thus, the quality factor (Q-value) of each REC was derived from $S_{11}$ response at -3 dB bandwidth [139]–[141].

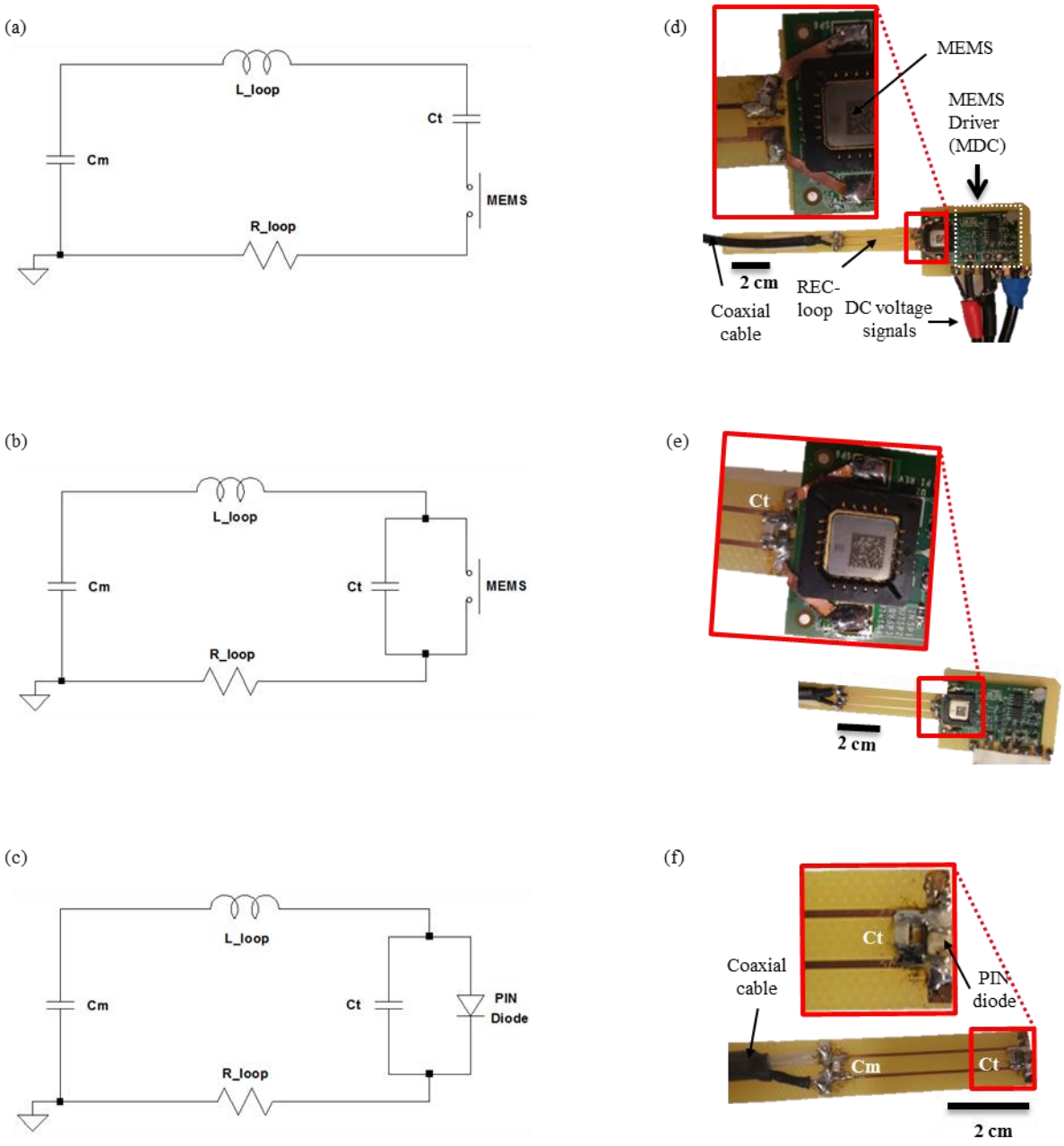


***Fig. 2-2.*** *Electrical schematics (first row) and the associated built prototypes (second row) of RECs using a controllable MEMS switch for active decoupling integrated (a,d) in series (sMEMS REC) or (b,e) in parallel (pMEMS REC) to the loop or using (c,f) a PIN diode integrated in parallel to the loop (pPIN REC). Ct and Cm are tuning and matching capacitors, respectively. R_loop and L_loop are the electrical resistance and inductance of the rectangular loop with 5.1 mm × 47 mm × 0.8 mm of width, length and thickness dimensions, respectively. The coaxial cable is the RF output used to transmit the NMR signal.*

***Table 2-1.*** *Tuning and matching capacitor values used.*

| RECs | MR switches | Ct values (pF) | Cm values (pF) |
|---|---|---|---|
| ***p*MEMS** | MEMS | 142.0 | 582.0 |
| ***s*MEMS** | MEMS | 120.2 | 382.0 |
| ***p*PIN** | MEMS | 158.2 | 549.0 |

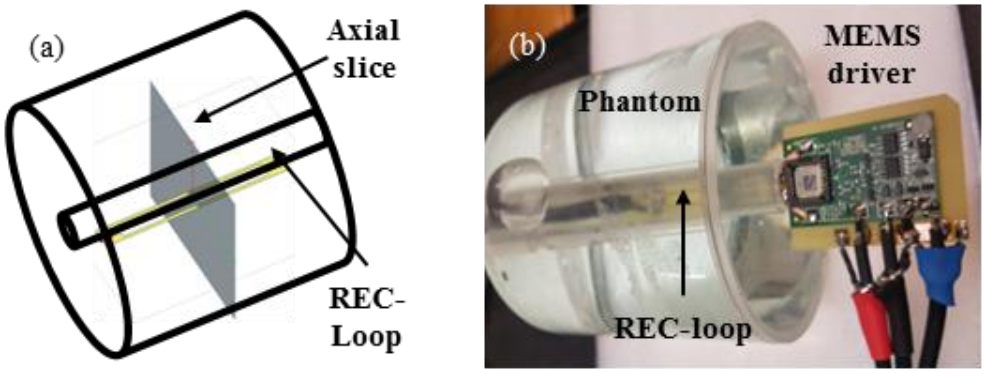


***Fig. 2-3.*** *(a) Drawing and (b) photograph of the cylindrical phantom used to load the REC for characterization as well as for imaging. The dimensions of the cylindrical phantom are 11 mm inner and 90 mm outer diameters and 100 mm length. It is filled with a solution of 1.25 g* $NiSO_4 \times 6H_2O$ *+ 5 g NaCl per liter of distilled water mimicking tissue losses.*

To assess the decoupling efficacy with a capacitive method, the $S_{11}$ response in the decoupled state was first used. In parallel decoupling strategies (*p*MEMS and *p*PIN RECs), decoupling is achieved by detuning the RECs (shifting of the resonance frequency) resulting in no resonance at $F_0$, which is characterized by the associated $S_{11}$ value at $F_0$ close to 0 dB. In the case of *s*MEMS REC, the switch is opened for a completely open REC loop thereby achieving active decoupling with a similar result in $S_{11}$ at $F_0$.

To confirm the obtained results, RECs were tested again with a mutual-induction method [142] based on the $S_{21}$ measurements. Two homemade flux probes (Fig. 2-4,c) were connected to the two ports of a VNA and overlapped to be mutually decoupled in free space (parallel, adjacent and overlapping loops). The REC was then placed close to the two probes such that if it resonated at $F_0$, a mutual coupling between the previously decoupled probes was created via the REC and specifically at its resonance frequency $F_0$. On the contrary, if the REC was decoupled then at $F_0$ there was no longer a coupling between the probes and the $S_{21}$ measured would drop significantly (by at least 30 dB). This is illustrated in Fig. 2-4,d. For both $S_{11}$ and $S_{21}$ measurements, coupled/decoupled

states were achieved by driving the opening or closing of the MEMS switch as explained previously.

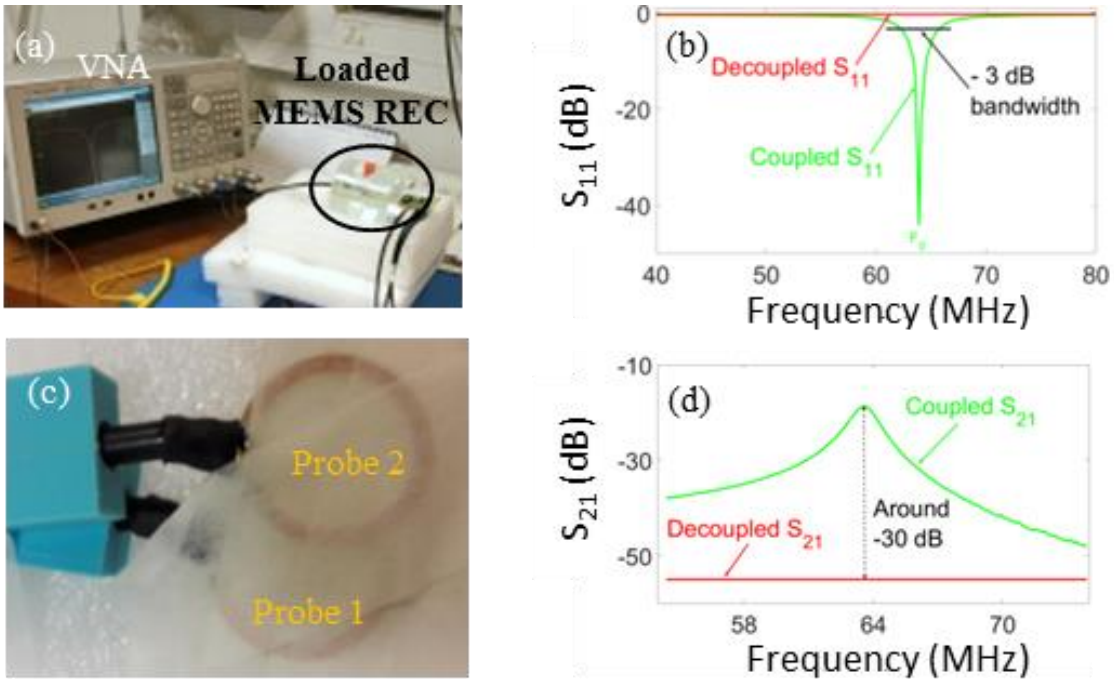


***Fig. 2-4.*** *First RF characterization set-up image (a) and the associated reflection coefficient ($S_{11}$) measurement method (b) by using a VNA. At coupling state (resonance frequency), amplitude at Larmor resonance frequency ($F_0$) and quality factor were derived from the $S_{11}$ response. At decoupling state, $S_{11}$ amplitude at $F_0$ was measured. (c) Decoupled dual loops position. (d) Second RF characterization set-up image and (e) the associated $S_{21}$ measurement method using the VNA.*

To assess the decoupling speed, switching delays from the coupled state to the decoupled state and vice versa were measured. A circular broadband copper loop (41 mm inner diameters) connected to a frequency generator (HAMEG Instruments HM 8134-3, Mainhausen, Germany) was used to generate an RF signal at $F_0$. By inductive coupling with the REC, the induced RF signal was measured using a digital oscilloscope (LeCroy waveJet 314, Lake Mary, FL, USA). To estimate the switching delays, a periodic square electric signal generated by a Waveform Generator (WG) (Agilent Technologies Inc. 33220A, Santa Clara, CA, USA) was used as coupling/decoupling control signal (-5 V / 7 V for MEMS on the MDC control input and 3.8 V / -10 V for the PIN diode) (Fig. 2-5,a). The coupling and decoupling delays were measured as the time between the DC square control signal and the RF response signal (Fig. 2-5,b).

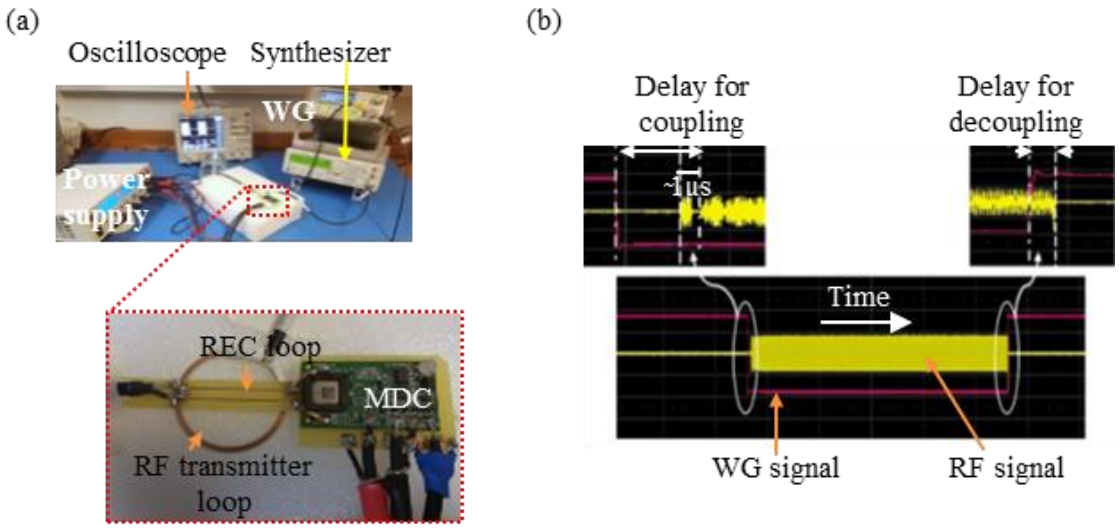


***Fig. 2-5.*** *Switching delays set-up image (a) and the temporal response measurements (b) of the MEMS Receiver Endoluminal Coil (REC). A frequency generator excites a circular copper loop to generate an RF magnetic field at the resonance frequency of the REC. The latter detects the RF signal while in coupled state but is unable to do so in the decoupled state. Coupling and decoupling are ensured by applying a square electrical signal from the WG. The received signal is observed on a digital oscilloscope. (b) Then, delays to couple or decouple the REC are estimated by measuring the delay between the applied control signal and the receive RF signal response.*

### 2.2.3. MRI set-up

Electronic circuits based mainly on tuning, matching and decoupling lumped components (such as capacitors, PIN diodes, …) causes some losses. MRI experiments were performed on a clinical Optima MR450w 1.5-T MR scanner (General Electric, Inc. Trademark) (Fig. 2-6). The body coil was used as RF transmitter. Both the REC and phantom were placed within the scanner with their axes aligned with the $B_0$ field in order to acquire 2D axial images. To interface the homemade REC to the MR system, a single-channel connector (A-plug) including a preamplifier (managed directly by the MRI system) with the appropriate configuration file was used. An RF circuit (RF/DC splitter) was placed between the RF channel of the A-plug connector and the REC in order to divert the DC control logic signal provided by the MR scanner. This was necessary because before starting a sequence, the MR system checks whether a coil is correctly plugged by verifying that a current can flow in the decoupling circuit. A decoy circuit was used in the case of MEMS RECs.

It should be noted that the DC control logic signal supplied by the MR scanner during the sequence does not always match the input control voltage required by the MEMS control circuit. Indeed, in the case of the *p*MEMS REC design, the MR control logic (out of the

MRI system) has to be inverted. Since the MR scanner we used was not configurable to perform this task, our solution was to use a waveform generator (WG). Thus, *p*MEMS REC was controlled in this work only by using the WG ($pMEMS_{WG}$ REC), while the *s*MEMS REC was controlled either directly by the MR system (*s*MEMS REC), as in the case of the *p*PIN REC and also with WG ($sMEMS_{WG}$ REC) so as to be able to characterize the effect of using the WG. For both MEMS configurations using a WG, a control signal of -5 V/7 V was generated with the WG while a control signal of -5 V/100 mA was used with the A-plug of the MRI system. An external power supply (Electro-Automatik EA-PS 2384-03B, Viersen, Germany) was used to supply 10 V and 82 V (bias signals) to the MDC. Both the power supply and the WG were placed outside the Faraday cage, in the technical room. Thus, three DC lines using coaxial cables (4.7 m for each line) were used to transport the three DC signals (10 V, 82 V and control signals). Traps were added every eighth of the wavelength (λ/8) of each coaxial cable (11 traps for each DC line) to avoid RF-induced signal [33], [34], which would otherwise lead to not only strong image quality degradation but also damage to the device (MEMS or/and MDC). The same was done on the RF signal reception cable.

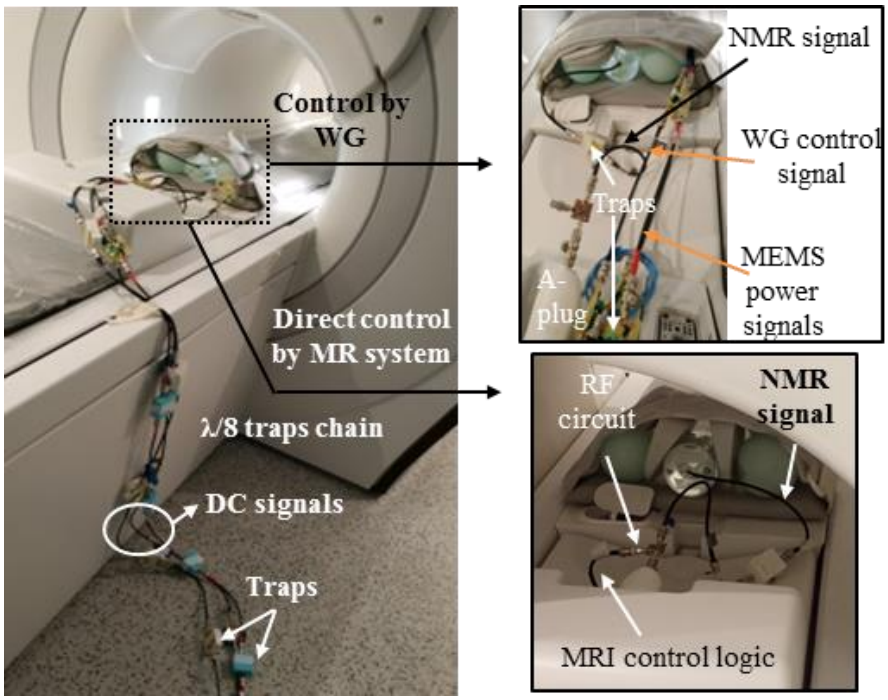


***Fig. 2-6.*** *Implementation on a 1.5-T MR system of the Receiver Endoluminal Coil (REC) using controlled MEMS switch. The body coil is used as an RF transmitter coil and the endoluminal coil as receiver. The RF circuit makes it possible to deviate the DC signal. The trigger by the WG makes it possible to ensure the DC control without the need to add an inverter circuit in the case of pMEMS REC. The REC is connected to the MR scanner via a specific interfacing connector (A-plug) with an adequate file configuration to identify the REC. Since both REC and phantom have their axes (lengths) aligned with the $B_0$ field, the 2D axial images are acquired using gradient echo (GRE) and spin echo (FSE) sequences.*

Multiple axial slices were acquired using gradient echo (GRE) and fast spin echo (FSE) sequences. Sequence acquisition parameters are summarized in Table 2-2.

The *s*MEMS, *p*PIN and *p*MEMS$_{WG}$ REC prototypes were compared in terms of mean SNR and SNR isocontours. Although the MR control logic can be used directly to control the *s*MEMS REC, the WG and the associated input control voltage line (including traps) were also used to assess the effects of employing the WG on image quality (*s*MEMS$_{WG}$ REC).

Images were post-processed using Matlab software (Mathworks, Milwaukee, USA), and mean SNR and signal uniformity distributions were calculated. The SNR was determined as the ratio of the mean signal intensity calculated on the entire phantom image and the standard deviation of a rectangular ROI placed outside the phantom. The SNR distribution map (SNR isocontours) was calculated and drawn for each REC. Then, mean SNR values were calculated for FSE acquisitions on concentric circles centered on the REC loop for radiuses between 11 mm and 22 mm.

***Table 2-2.*** *Acquisition parameters used for both gradient echo (GRE) and spin echo (FSE) sequences*

| Sequence | Orientation | TR/TE (ms) | FA (°) | FOV (mmxmm) | Slice thickness (mm) | Spacing slices (mm) | Matrix size | Receive BW (±kHz) | Number of slices |
|---|---|---|---|---|---|---|---|---|---|
| GRE | Axial | 400/9 | 80 | 100x100 | 2 | 0.5 | 256x256 | 11.9 | 13 |
| FSE | Axial | 3100/14.1 | 90/180 | 100x100 | 2 | 0.2 | 256x256 | 15.6 | 13 |

## 2.3. Results

The measured frequency and temporal response parameters for the three REC prototypes in coupled and decoupled states are summarized in Table 2-3. In coupled state, reflection coefficient values $S_{11}$ at $F_0$ were approximately -30 dB for all RECs. The loaded quality factor of the *s*MEMS was significantly lower (37%) than the *p*MEMS REC, which in turn had a slightly higher Q-value that the *p*PIN REC. Unloaded (data not reported) and loaded Q-values were almost similar for each individual REC.

In the decoupled state, measured reflection coefficient values $S_{11}$ at $F_0$ were measured to be almost 0 dB (no resonance) for all RECs. Resonance frequencies of *p*MEMS and *p*PIN RECs were shifted from 63.95 MHz to 20.47 MHz and 29.3 MHz, respectively. In the case of the *s*MEMS REC, the loop is completely open and thus the REC was not resonating at all. The mutual decoupling of the two loops at $F_0$ was also shown with a drop in $S_{21}$ measurements of more than 30 dB for all RECs.

Switching delays to both coupled and decoupled states were less than 0.7 µs for the *p*PIN REC. Regarding both MEMS RECs, coupling delays were equal to 7.5 µs and 2.1 µs for *s*MEMS and *p*MEMS, respectively, while decoupling delays were equal to 1.8 µs and 9.8 µs for *s*MEMS and *p*MEMS, respectively.

For imaging experiments, the presence of traps on the DC control line and DC power supply lines of the MDC was mandatory in order to have an unaltered DC bias and stable power supply during the scan. Indeed, in the absence of traps, RF signals induced by the transmitter body coil were superimposed onto the DC control signal (up to 20 V peak to peak, depending on the sequence used) and could inappropriately couple or decouple the REC. In that case, the acquired image is extremely noisy and moreover, could lead to damaging the MDC board and/or the MEMS switch. This occurs when the number of traps is inadequate.

***Table 2-3.*** *Measured frequency and temporal response parameters for the three coil prototypes with coupling and decoupling states.*

| States | Measured | *p*PIN | *s*MEMS | *p*MEMS |
|---|---|---|---|---|
| **Coupled** | F0 (MHz) | 63.95 | 63.92 | 63.95 |
| | S11 at F0 (dB) | -28.70 | -36.40 | -29.20 |
| | S21 at F0 (dB) | -18.45 | -26.20 | -20.30 |
| | QLoaded | 62.50 | 41.20 | 65.10 |
| **Decoupled** | S11 at F0 (dB) | -0.28 | -0.09 | -0.10 |
| | S21 at F0 (dB) | -48.10 | -56.10 | -55.00 |
| | Delays to couple (µs) | 0.70 | 7.50 | 2.08 |
| | Delays to decouple (µs) | 0.25 | 1.84 | 9.80 |

From a qualitative point of view, Fig. 2-7 shows that the obtained images display similar elliptical image sensitivity patterns and no signal saturation even close to the REC. No artifacts due to active decoupling failure were observed on the images when using GRE or FSE. Small holes were observed on each image (anterior part of the phantom) obtained by both MEMS RECs.

Mean SNR values calculated for FSE acquisitions on concentric circles centered on the REC loop for radiuses between 11 mm and 22 mm showed that for all radiuses, SNR decreased in the following order:

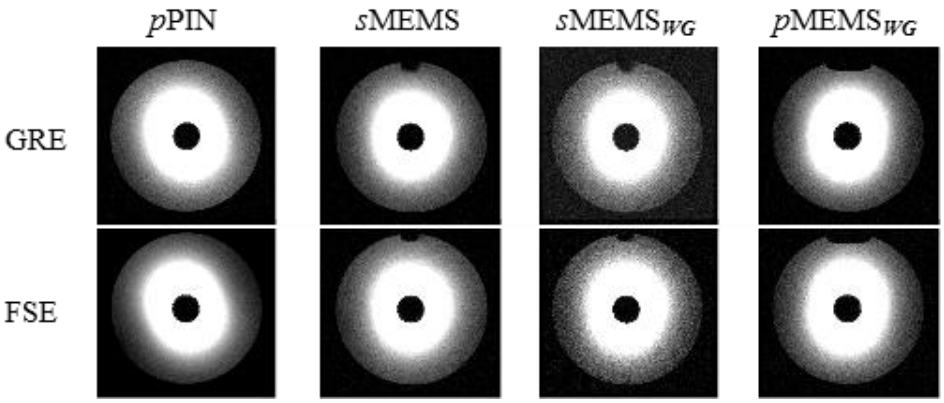


***Fig. 2-7.*** *Representative 2D axial MR images acquired with GRE and FSE sequences for the different RECs prototypes (PIN and MEMS) and displayed using a narrow signal intensity window.*

*p*PIN > *s*MEMS > *p*MEMS$_{WG}$ > *s*MEMS$_{WG}$. The SNR isocontours calculated for all experimental configurations and prototypes using FSE sequences are displayed in Fig. 2-8. Figure 8-a enables an easy comparison of the image quality of *s*MEMS, *p*MEMS$_{WG}$ and *p*PIN RECs together; Fig. 2-8,b compares *s*MEMS$_{WG}$, with *p*MEMS$_{WG}$ (performance of *s*MEMS and *p*MEMS in the same control conditions), while a comparison between *s*MEMS and *s*MEMS$_{WG}$ (WG control technique effect) is presented in Fig. 2-8,c.

## 2.4. Discussion

In this work, we evaluated the serial and parallel active decoupling of MEMS REC performances in terms of switching delays, quality factor, decoupling isolation (efficiency), delays (speed) and image SNR.

Opening and closing delays of the MEMS itself are 1 µs and 4 µs, respectively, which largely explains the decoupling and coupling delay differences of the same MEMS REC. Opening of the MEMS leads to coupling of the *p*MEMS REC and decoupling of the *s*MEMS REC, which thus display almost similar delays of 2.1 µs and 1.8 µs, respectively.

Closing of the MEMS switch instead leads to decoupling of the *p*MEMS REC and coupling of the *s*MEMS REC, which in this case display delays of 9.8 µs and 7.5 µs, respectively. The slight difference in delay (2.3 µs) in the last case is probably due to the specific operation technique of each configuration (by closing the MEMS, the REC loop is closed in coupled state in the case of the *s*MEMS REC while in the case of the *p*MEMS REC, the resonance frequency is shifted by short-circuiting the tuning capacitor). With switching delays between 0.25 µs and 0.7 µs, the reference *p*PIN REC switches faster than the MEMS-based REC for coupled and decoupled states. These relatively longer delays are

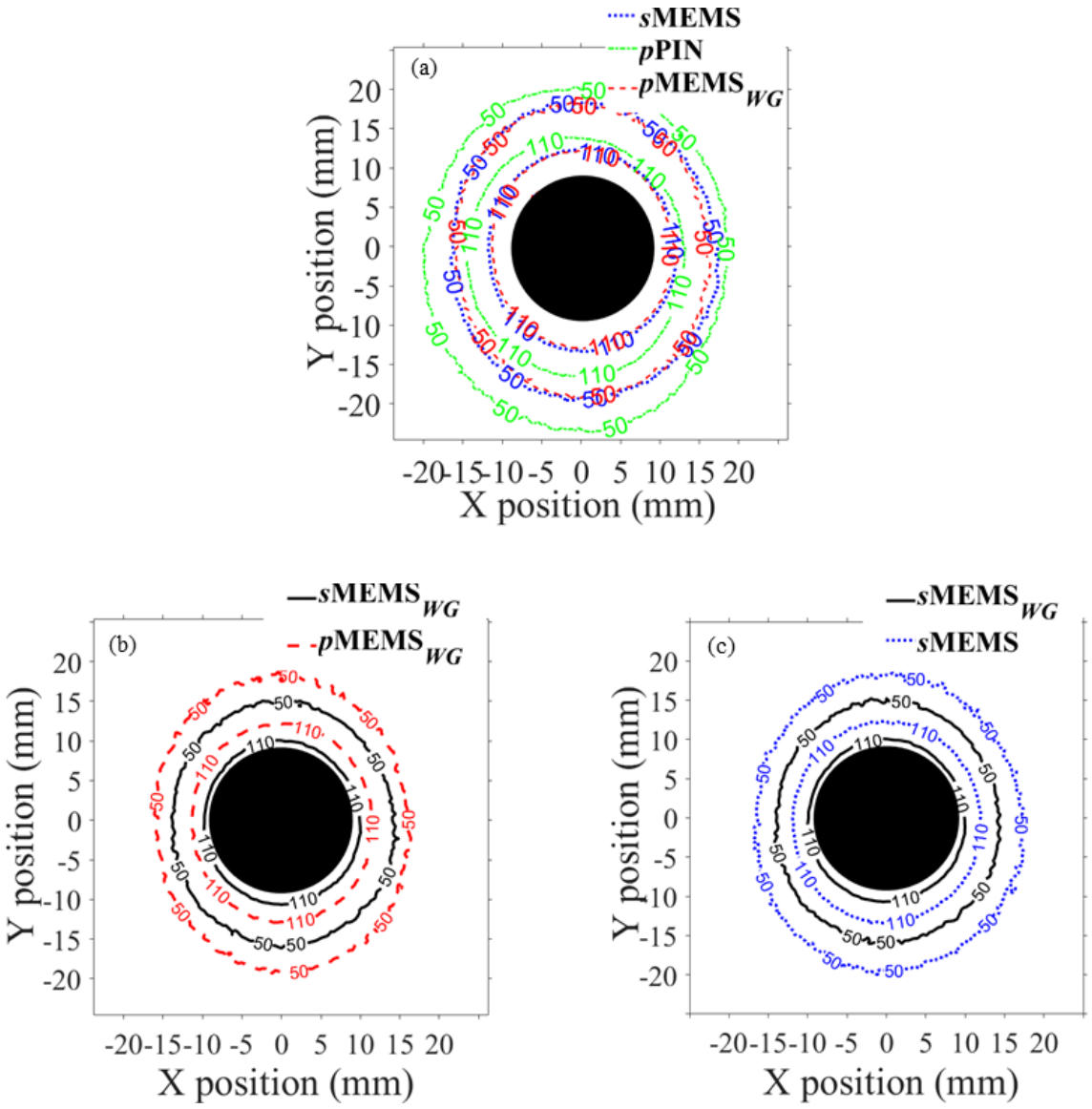


***Fig. 2-8.*** *Signal-to-Noise Ratio (SNR) distributions based on iso-contour lines calculated and drawn on axial FSE images acquired by using the different REC prototypes. Numbers on each iso-contour line represent the calculated SNR value obtained with the associated REC. (a) Comparison between sMEMS, pMEMS$_{WG}$ and pPIN RECs to assess the quality image performance of MEMS RECs. (b) Comparison between sMEMS$_{WG}$ and pMEMS$_{WG}$ RECs acquired with the same experimental conditions to assess the performance of MEMS on the image quality in each configuration. (c) Comparison between sMEMS and sMEMS$_{WG}$ RECs to evaluate the effect of the use of the waveform generator on the acquired images.*

due to the time necessary to move the switch mechanically and to the switching delays of its driver circuit [65]. The increased delays by adding such driver circuit is also demonstrated in a recent work [143] using a PIN diode driver for high-power pulses where the rise-time is close to 1 µs and the fall-time increases to 7.4 µs, which are comparable to the results obtained with controlled MEMSs. Delays are nevertheless of the same order as optical-based decoupling circuits with 13.6 µs and 1.7 µs for tuning and

detuning, respectively [131], which proved to be effective. In any case, MEMS switching delays are still small and compliant with most MR clinical applications where the RF pulse duration of imaging sequences as well as signal readout time [65] are of the order of milliseconds. The only case that would be problematic in our application is that of ultra-short echo times (UTE) in the range of a few microseconds.

An equivalent REC devoid of any decoupling circuit was built and characterized and it has a Q-value of 66. Among the REC loop, the *p*MEMS REC had the highest Q-value (~65). It is comparable to the *p*PIN REC (~62), with the lowest value being for the *s*MEMS REC (~41). This is due to the MEMS characteristics and its location on the REC loop. In the case of the *p*MEMS REC in the coupled (reception) state, the MEMS is open. In this state, it can be considered as an additional capacitor of only about 1.5 pF placed in distal position in parallel to the tuning capacitor of the REC. Because it is a mechanically open switch, it has a high isolation resistance of approximately 10 MΩ. Thus, the MEMS does not impact the real part of the REC impedance, which affects the quality factor minimally. Rescia et. al. [132] also demonstrated on a 4-cm surface coil at 400 MHz (9.4 T) that the MEMS, placed in parallel to the loop, had almost no effect on the quality factor compared with other electrical components such as PIN diodes. In the case of the REC used, the PIN diode had a very moderate effect on the Q-factor. For the *s*MEMS REC, the switch is closed in the reception phase. It can then be considered as a significant 0.5 Ω to 1 Ω parasitic resistance [63], [138] in the loop that should be compared with the loop size and its equivalent electrical resistance. This explains the experimental 0.62 ratio of Q-values between the *s*MEMS REC and a REC without any decoupling circuit. This ratio is comparable to the 0.59 theoretical Q-ratio calculations based on resistive losses [144].

Regarding decoupling efficacy, $S_{11}$ responses of around 0 dB demonstrate an efficient active decoupling of all RECs especially for *s*MEMS REC with an open loop. For all RECs, the $S_{21}$ results confirm the decoupling efficacy with a drop of more than 30 dB in $S_{21}$ measurements at $F_0$. This was confirmed on MR images where no signal artifacts were detected.

Signal intensity distribution, SNR iso-contour and mean SNR values of MR images obtained with *s*MEMS, *p*PIN and *p*MEMS$_{WG}$ RECs confirm that MEMSs are relevant systems for achieving active decoupling. In our experiments, the *p*PIN REC always provided the highest SNR. This was expected compared with the *s*MEMS REC, which had the lowest Q-value owing to the presence of an additional parasitic resistance in the receive phase. In addition, despite the *s*MEMS decoupling signal being generated by the MR scanner through the A-plug, the external power supply was still used (to provide 10 V and 82 V

bias voltages) and thus associated coaxial cables and traps were also used, which led to an additional noise on the images.

In the case of the *p*MEMS$_{WG}$ REC, SNR values are lower than those of the *p*PIN REC, which is not in agreement with the RF bench characterization results in terms of Q-value that was the highest for the *p*MEMS REC and thus we expected a better or at least similar SNR between *p*MEMS and *p*PIN RECs. As mentioned above, the use of an external power supply for the MDC of all MEMS-based RECs is the first factor affecting the measured SNR values negatively. In the case of the *p*MEMS$_{WG}$ REC, there is an additional source of noise originating from the external WG used to obtain the required coupling and decoupling signals (the MR system used could not handle it directly).

*s*MEMS$_{WG}$ and *p*MEMS$_{WG}$ REC experiments based on the same control condition (waveform generator) shown in Fig. 2-8b demonstrate that the *p*MEMS$_{WG}$ REC presents a higher SNR (about 45%) than the *s*MEMS$_{WG}$ REC, which means that the *p*MEMS REC (without WG control) can be estimated to yield an SNR higher (45%) than the *s*MEMS REC, in agreement with the obtained Q-values.

In order to characterize this added noise due to the external WG, images were also acquired using the *s*MEMS REC with the decoupling signal coming from the external wave generator (*s*MEMS$_{WG}$ REC). The resulting images (Fig. 2-7 columns 2 and 3) and SNR isocontours (figures 8-c) demonstrate that the use of the external WG control leads to an SNR reduction of approximately 35%, which can also be used to extrapolate SNR values that could be obtained with a *p*MEMS REC (without the use of the external WG). The *p*MEMS$_{WG}$ performance compared with the *p*PIN performance is hence significantly penalized by this step, which was mandatory because of the use of an MR450w system. Performing the experiments on a new GE MR scanner would ease the use of MEMS as a decoupling component thanks to the native integration of 82-V and 10-V delivery voltages as well as DC bias delivery for active decoupling in logic suited for all MEMS configurations. Such "on-board" voltage sources would then remove the additional noise from the mandatory setup described.

It should be noted that three separate but identical (size and solution) phantoms were used for the PIN, *s*MEMS and *p*MEMS experiments. The small holes that can be seen on the MEMS images correspond to air bubbles (see also Fig. 2-3b) in each MEMS phantom due to the cylindrical vessel not being completely air-tight and not due to the MEMSs themselves. Coincidentally, the PIN phantom cylindrical vessel was almost completely

air-tight and did not have air bubbles; thus, no hole was observed on the MR images obtained with the *p*PIN REC.

In addition, SNR values in the ROI of the *p*MEMS REC are much higher (factor of approximately 10) than those obtained with the Whole Body Coil (WBC) or with a commercial external array coil (GEM Flex Coil 16-S Array, 1.5T Receive Only, NeoCoil, USA) as shown in Fig. 2-9. It should be noted that the array coil displays its maximum SNR on the external surface of the phantom, which is not our ROI, and the SNR decreases rapidly when moving away from the surface so that in the ROI, its SNR is much lower than that achieved with our REC.

Table 2-4 summarizes the important SNR results obtained.

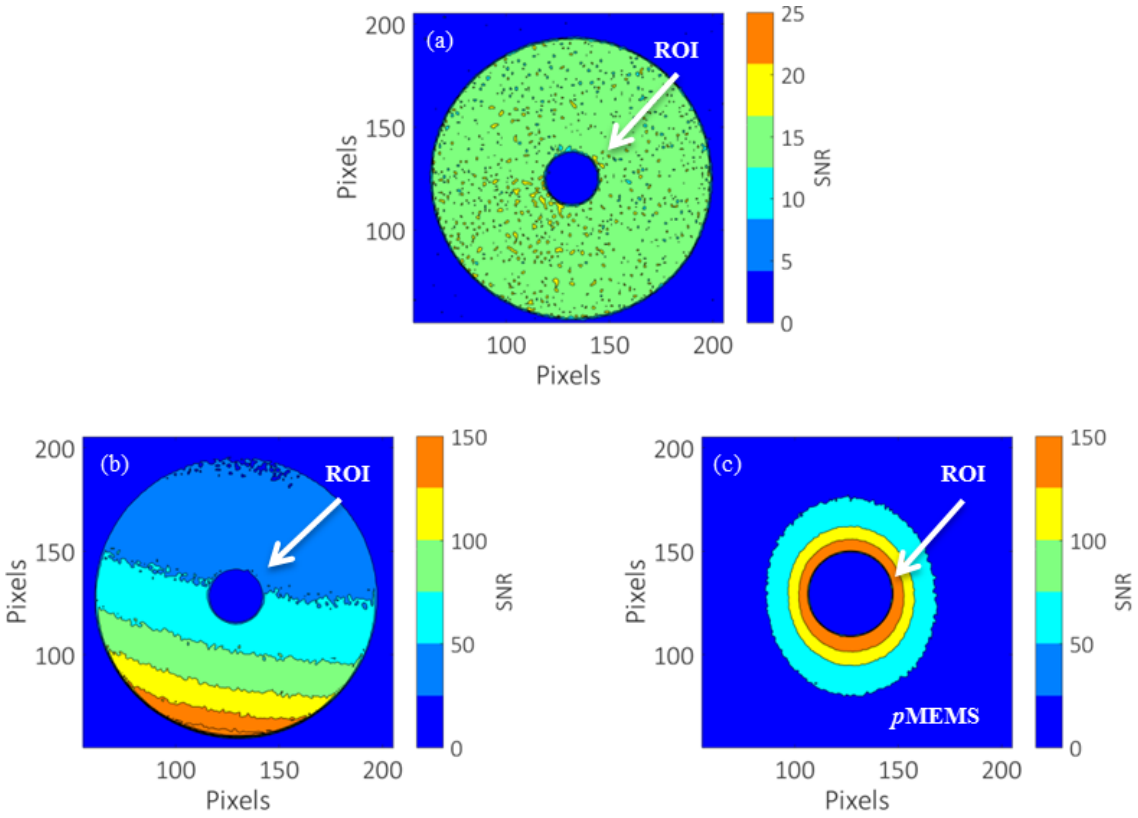


***Fig. 2-9.*** *SNR maps obtained with (a) the whole-body coil, (b) an external commercial array coil and (c) the pMEMS REC. The pMEMS REC provides an SNR higher than both the WBC (gain of 10) and the array coil. The latter displays high SNR only on the anterior surface of the phantom, (which is not our region of interest) with a rapid decrease when moving away from it. Since our region of interest is the internal surface, the array coil is not a convenient solution for our imaging target.*

***Table 2-4.*** *Table SNR results summary.*

| Analysis parameter | Comparison |
|---|---|
| **SNR** | pPIN diode coil has the highest SNR |
| | pMEMS > sMEMS (same conditions) : 45% |
| | Effect of WG : -35% |
| | pMEMS > Body coil : factor of 10 |
| | pMEMS > commercial array coil : in ROI |

## 2.5. Conclusion

In conclusion, the *p*MEMS$_{WG}$ configuration (based on an external control) presented here does not yet provide significant advantages over the *p*PIN configuration (Fig. 2-8a) mainly because of the external equipment required (WG, DC bias voltages, traps and coaxial cables). As perspectives, it is expected that the *p*MEMS REC decoupling solution should present higher SNRs than the conventional *p*PIN configuration, since the measured Q-values suggest that removing the external control and using an MR-compatible control method for the *p*MEMS REC would yield higher SNRs than those achieved with the *p*PIN REC. An interesting perspective for the use of MEMS switch resides in serial configuration (in series with the REC loop). Although the SNR is reduced, the decoupling remains efficient and MEMS could be used not only for active decoupling but also to allow for REC loop geometry reconfiguration. This could be particularly relevant in the case of colon wall examinations where REC-loop orientation with respect to the main magnetic field changes with location, leading to MR signal distribution changes. We believe that a combination of both *s*MEMS and *p*MEMS configurations in the design of new reconfigurable RECs may offer interesting designs and open the way for novel applications.

## Chapter conclusion

This chapter is the first part of the thesis work which consists in validating the feasibility of using MEMS on endoluminal coils and evaluating their performances in terms of active decoupling and image quality (SNR).

So, two prototype configurations of one-channel MEMS endoluminal coils were proposed to achieve sufficient and fast serial and parallel active decoupling. The serial design consists in integrating a MEMS switch into the coil-loop. The parallel design consists in integrating a MEMS switch in parallel to the coil-loop, precisely in parallel to the coil tuning capacitor. Then, they were built and characterized on both experimental bench and through images acquired on an Optima MR450w 1.5-T MR scanner, General Electric, Inc. Comparison of both prototypes with an external array coils and whole body coil used in receive modes validated what was already known that is, the advantage of using an endoluminal coil for regions close to the coil as in the colon. These prototypes were also compared to the standard decoupling solution (PIN diode). Briefly, obtained results confirmed that MEMS switches are a credible solution for active decoupling.

It should be noted that the main originality of this part is the implementation of the MEMS switches on the miniature endoluminal coils with very good performances, which has never been reported in the literature.

This validation of MEMS coil prototypes performance leads to a strong motivation to focus on the second part of the thesis described in chapter 3. Since the effect of MEMS switches and MEMS drivers have been experimentally assessed in the present chapter, the next chapter will focus on the optimization of the coil with respect to colon-rectum regions, taking into consideration coil and phantom losses with the help of numerical electromagnetic simulations.

# Chapter 3: MEMS-based reconfigurable endoluminal RF coils

# Chapter 3

# Reconfigurable endoluminal RF coils using MEMS switches

## Contents

*This chapter details the second thesis axis related to the dependency of coil-sensitivity with coil-orientation with respect to $B_0$ field. The first part corresponds to a proposition of reconfigurable MEMS-based one-channel endoluminal coil design for MR imaging (corresponds to a submitted article)*. The second part corresponds to *a proposition of* a *one-channel* MEMS reconfigurable 1H/31P rectal coil for spectroscopy imaging.

# 3.1. Optimization of signal distribution through simulation of various RF endoluminal loop geometries with coil orientation: *Reconfigurable loop coil using MEMS*

This section corresponds to the **<u>submitted</u>** manuscript of the article: "*Optimization of signal distribution through simulation of various RF endoluminal loop geometries with coil orientation: Reconfigurable loop coil using MEMS*"; in Journal of Concepts in Magnetic Resonance Part B: Magnetic Resonance Engineering, at October 2020, Hamza Raki, Kevin Tse Ve Koon, Henri Souchay, Fraser Robb and Olivier Beuf. This may be used for non-commercial purposes.

## Abstract

With the objective of improving MR endoluminal imaging of colonic wall, electromagnetic simulations of different configurations of single, double layers and double turns endoluminal coil geometries were run. Indeed, during colon navigation, variations of coil orientation with respect to B0 are bound to happen and lead to impaired acquired images due to a loss of signal uniformity. In this work, three typical coil orientations encountered during navigation were chosen and the resulting signal uniformity of the different geometries were investigated through the simulated $\frac{B_{1x,y}}{I\sqrt{R_t}}$ values. Sampling this quantity over a circle of radius *r* enabled calculating the coefficient of variation (= standard deviation/mean) for this given distance. This procedure was repeated for $r \in [5;15]$ mm which represents the region of interest in the colon. Our results show that a single loop (DSL) and double layer (RDL-OC) geometry could provide complementary solutions for improved signal uniformity. Finally, using four Micro Electro-Mechanical Systems switches, we proposed the design of a reconfigurable endoluminal coil (swiM RE-Coil) able to switch between those two geometries while also ensuring the active decoupling of the endoluminal coil during the RF transmission of an MR experiment.

**Keywords:** MRI endoluminal coils, reconfiguration, MEMS switch, loop-orientation, signal distribution, electromagnetic simulation

### 3.1.1. Introduction

Inflammatory bowel diseases mainly appear as ulcerative colitis and Crohn's diseases [145]. They affect both colon and rectum with an increased risk to evolve into a colorectal cancer (CRC) [7] which is one of the most common cancers [115], [116]. Worldwide, it is the second and the third most frequent cancer for women and men, respectively [10] and accounts for 8.5% of all cancer deaths [11]. The treatment of CRC at early stages allows a 5-year survival rate higher than 90%, in contrast to late stages where this rate is less than 10% [16]. This is why it is important to develop new imaging devices or techniques able to provide an accurate diagnosis for each stage, particularly the early-one.

Magnetic Resonance Imaging (MRI) is one of the major techniques used for medical diagnosis, particularly for digestive diseases, due to several developments such as the increase of the static magnetic field strength to improve SNR [146]–[148], the development of fast imaging sequences to reduce the acquisition times [149], the increase in the number of channels in the MRI systems and the use of arrays of external receiver surface coils based on combination of small radiofrequency (RF) loops to improve significantly the SNR [75], [118], [148], [150], [151]. Unfortunately, all these developments are still insufficient for bowel and colon wall imaging. Analysis of the deep and thin colon wall layers, assessment and staging of colorectal cancer are still very much challenging.

Previous works have demonstrated the value of endoluminal imaging based on miniature internal receiver surface coils (endoluminal coils). In the context of colon imaging, endoluminal coils provide a high local SNR very close to the region of interest compared to the external surface coils [152]. Preclinical endoluminal coil designs, usually based on single channel and single loop geometry, were assessed for the imaging of arterial wall of large vessels [153], pelvis and gastrointestinal tract [77], rabbit colon walls [121] and mouse colon walls [124]. In clinical routine, MR endorectal single coil-loops were used to visualize the prostate and the rectum area (Medrad Prostate eCoil, Bayer) or the cervix (Medrad Cervix eCoil, Bayer).

An important issue with the use of endoluminal coil for deeper regions is the total safety of the patient for which no compromise must be tolerated. Strong and local SAR increases can be induced by transmitter RF coil within the connection cables. Because of the space constraints, the use of cable traps [33], [34], [154] is not appropriate and full optical-based signal transmission appears as a potential alternative to solve this problematic [37]. A second limitation is the acceptance and comfort of the patient. The

reduction of the coil diameter strongly contributes to advances in this domain. In addition to increasing the patient comfort, it also helps obtaining a higher local SNR. However, the gain in sensitivity is only local and accompanied by a rapid decrease with increasing distance from the coil [26]. Fortunately, the targeted colon wall area is less than 1 cm thick which renders endoluminal coil designs a credible alternative for colon wall imaging. This article deals with the problematic related to the required coil navigation within the colon. In fact, a coil loop suffers from sensitivity-map variations as a function of coil-orientation with respect to the main magnetic field ($B_0$). A maximum of coil-sensitivity and uniformity is ensured only when the long axis is aligned with $B_0$ that is, the normal to the coil loop surface (main $B_1$ direction) is orthogonal to $B_0$ [155]. This orientation is considered as the reference orientation. Departure from this optimal condition induces changes in the coil sensitivity map and thus both intensity values and radial distribution uniformity (shape) are altered by this coil orientation effect leading to degraded coil sensitivity and thus impaired image quality. This question of sensitivity variations with the orientation is a major challenge for colon wall imaging (Fig. 3-1). As can be seen, the sensitivity variation depends on the colon region. In this work, we defined 3 main groups of regions according to the possible coil-orientations (Fig. 3-1):

- Vertical regions: rectum (1), descending colon (3) and ascending colon (7).
- Horizontal region: middle part of transverse colon (5).
- Tilted regions: sigmoid (2) and the two extremities of transverse colon (4, 6).

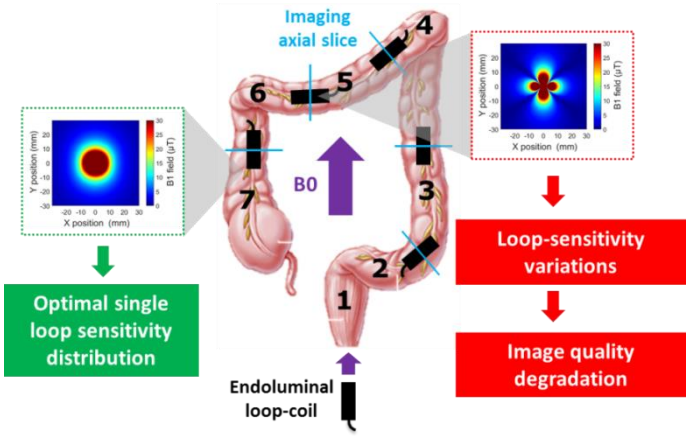


**Fig. 3-1.** The coil-path inside of the colon: the effect of the different coil-orientations within $B_0$ on the sensitivity map of the coil. Parts 1, 2, 3, 4 and 5 are rectum, sigmoid colon, descending colon, transverse colon and ascending colon, respectively.

Different research groups have characterized non-uniformity of reception profiles and hence developed strategies to correct it. Some analytical corrections have been proposed without [156], [157] and when [158]–[160] taking into account the coil orientation effect. However, none of these methods was able to achieve a complete correction [160], [161]. Other approaches are based on hardware development by designing optimal and

dedicated coil geometries to improve the radial signal uniformity without using post-processing corrections. In this context, an anal-sphincter endoluminal-coil based on two turn loops with an angle of 50° or 70° between them was assessed. Compared to a single loop, this design allowed improving the radial distribution uniformity [58]. However, the coil orientation regarding $B_0$ was not taken into consideration in this work. Intravascular catheter guiding using visible markers based on resonating coils can also be affected by coil orientation variations inside the magnet [162]. To the best of our knowledge, none of the published work addressed sensitivity variations that can be met during navigation within colon due to coil orientations.

Few years ago, Micro Electro-Mechanical System (MEMS) were introduced by GE Healthcare Inc. [68] to act as MR switches. MEMS switches were successfully used: i) to open or close portions of metallic conductors and thus to reconfigure coil-loop geometries [63]; ii) to shift the resonance frequency in the case of dual tuned RF coils [64], [65]; iii) to get high RF shimming performances (high localized $B_0$ homogeneity) [66]; iv) to control and automatize a wireless power transfer system [67] and finally v) to control multiple receiver coil arrays with reduced power consumption and cabling system improving SNR [163]. A recent work [164] demonstrated the feasibility and the impact of using MEMS switches on endoluminal coils for fulfilling the task of serial and parallel active decoupling and studying their impact on the image quality.

In this context, the main goal of this work was to investigate different geometries with small width coil loop (5 mm) and to assess the radial sensitivity pattern with respect to coil orientation with respect to $B_0$ (signal intensity and distribution). This was carried out through electromagnetic (EM) numerical simulations. Then, complementary geometries were chosen to design a theoretical reconfigurable RF coil using switches such as MEMS placed in parallel or in series within loop path in order to change the coil geometry according to its orientation to have optimal coil sensitivity pattern.

## 3.1.2. Material and Methods

Different miniature rectangular single and double loop-geometries were defined and evaluated. The dimensions were chosen taking into consideration the eventual insertion into the colon (less than 10 mm outer diameter) and defined within a cuboid volume with dimensions 5 mm × 5mm × 47 mm (Fig. 3-2).

All loop geometries were designed with 47 mm conductor strip lengths. A diagonal single loop (DSL) was defined in the diagonal (in two opposite parallelepiped-faces); thus the

loop width was about 7.1 mm (Fig. 3-3). Four rectangular double loops (RDLs) geometries were defined with a strip conductor in each parallelepiped-face (Fig. 3-4).

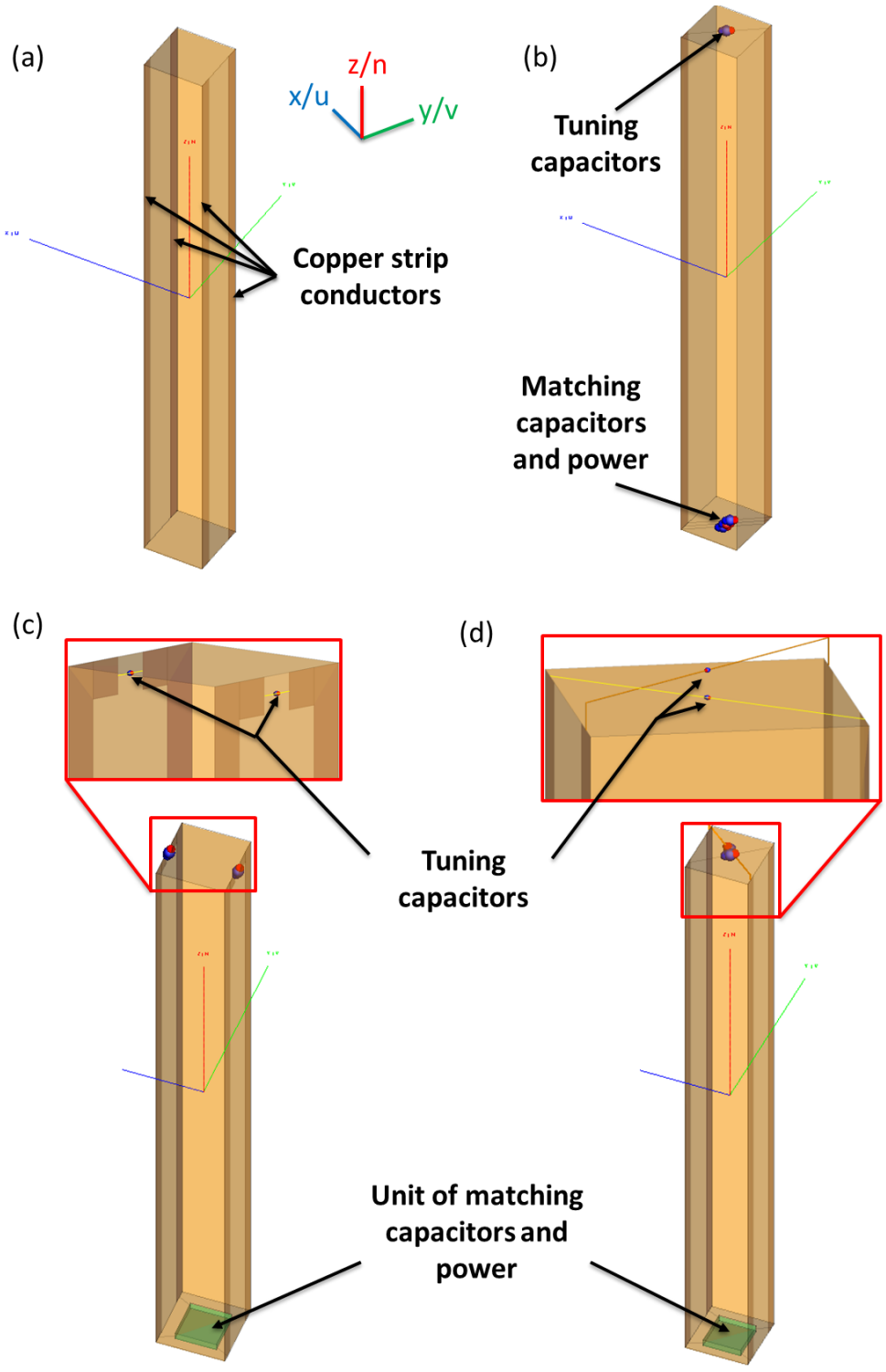


**Fig. 3-2.** Different simulated endoluminal loop-geometries. (a) The basic design of cuboid volume (5 mm × 5mm × 47 mm dimensions) with four copper strip conductors. (b) Diagonal single loop (DSL). (c) Rectangular double loop (RDL). (d) Diagonal double loop (DDL).

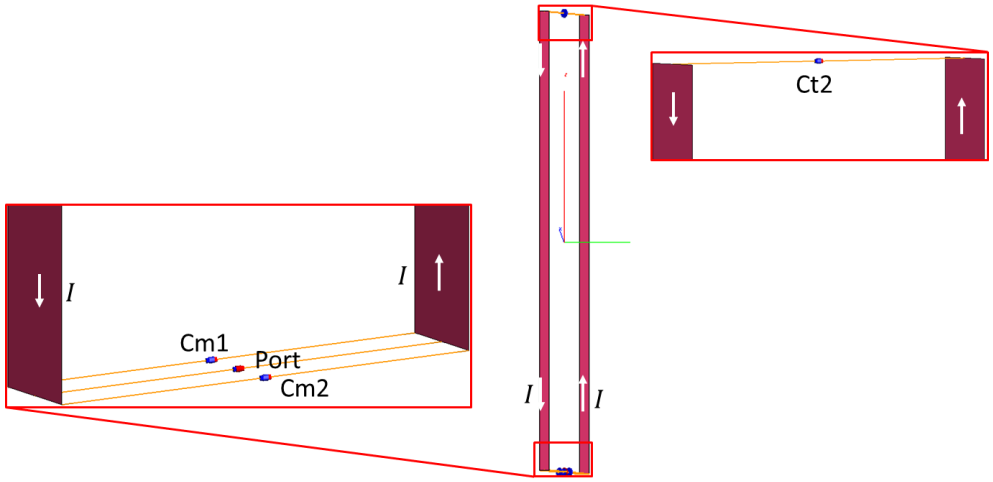


**Fig. 3-3.** Detailed diagonal single loop (DSL) design.

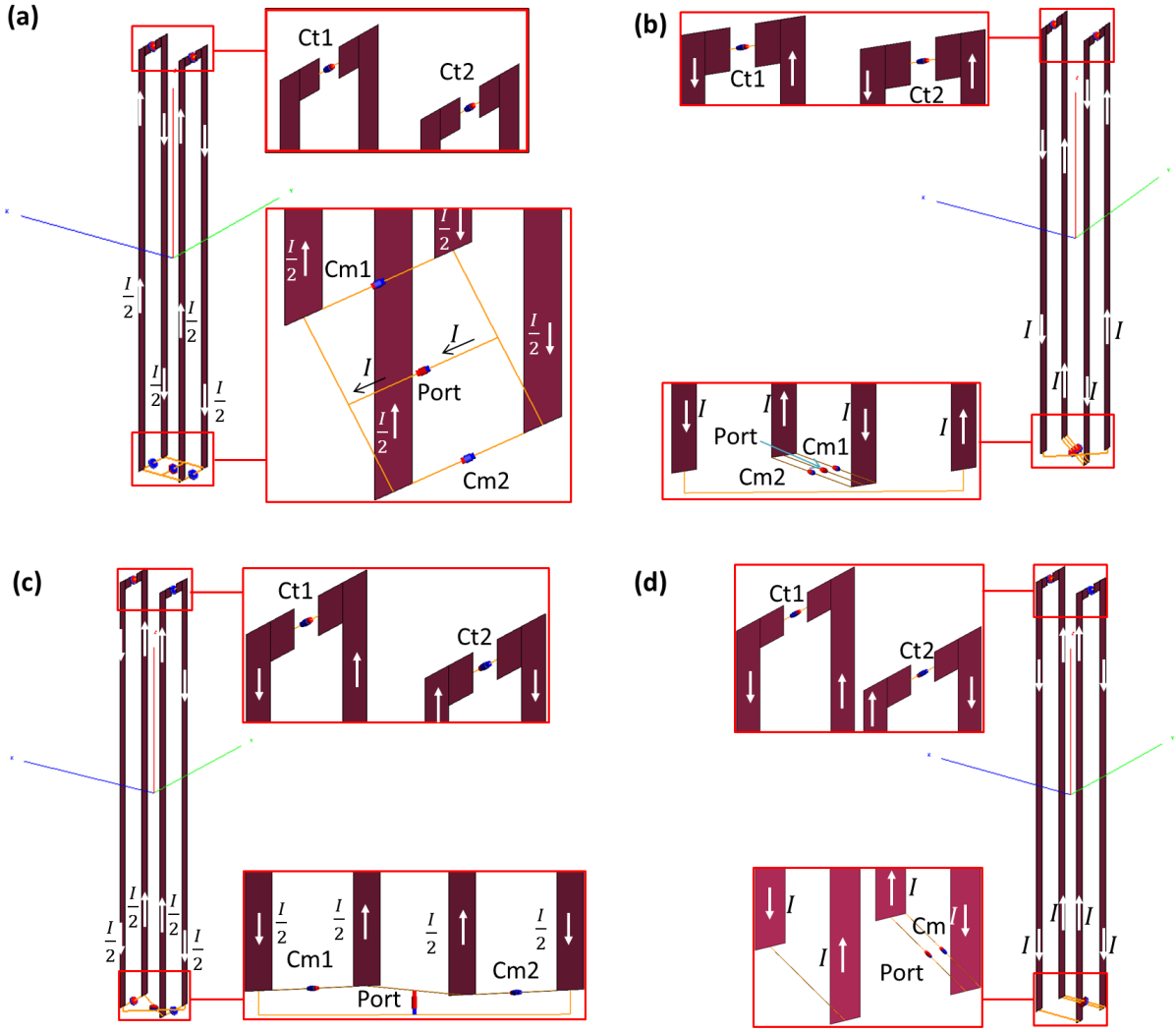


**Fig. 3-4.** Detailed rectangular double loop (RDL) designs. (a) The rectangular double layer, same current (RDL-SC). (b) The rectangular double turn, same current (RDT-SC). (c) The rectangular double layer, opposite current (RDL-OC). (d) The rectangular double turn, opposite current (RDT-OC).

Loops were defined on two opposite faces with 5 mm loop spacing. Then, the current direction was modified to get four possible designs: two double turn loops and two double layer loops. In the double turns design; the two loops are in series whereas for the double layers design; the loops are connected in parallel. For the two geometry designs, current can flow in the same direction or in the opposite direction giving the four studied geometries. Finally, similarly to the RDL design, a diagonal double loop (DDL) was defined with a strip conductor in each parallelepiped-face but linked in the diagonals (Fig. 3-5) to form also double turn or double layer loops. The two defined loops are then perpendicular to each other and current can flow in two directions: D1 and D2. Hence, the number of loops, the serial or parallel type and the current flow direction defines each coil loop configuration.

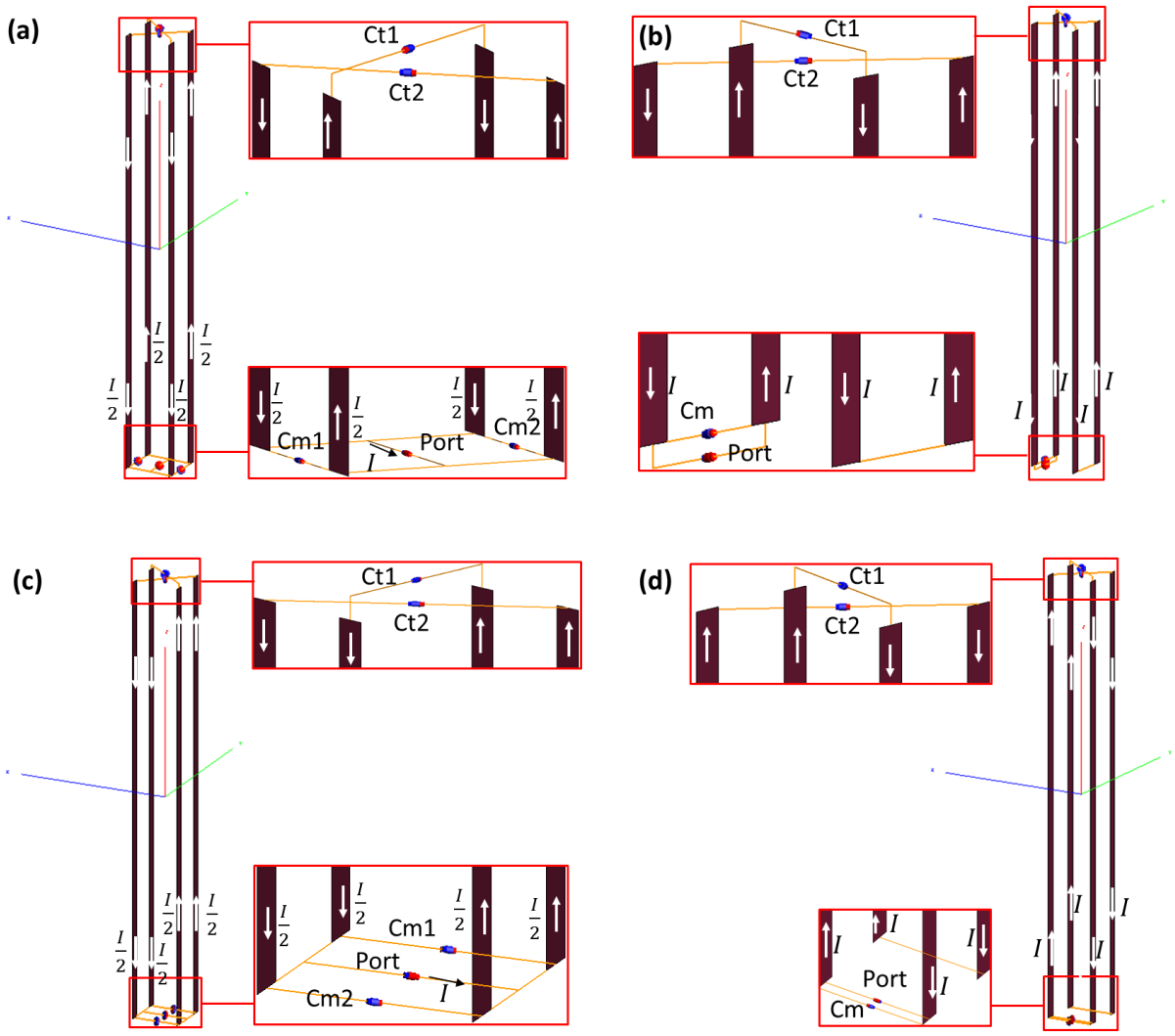


**Fig. 3-5.** Detailed diagonal double loop (DDL) designs. (a) The diagonal double layer, current direction 1 (DDL-D1). (b) The diagonal double turn, current direction 1 (DDT-D1). (c) The diagonal double layer, current direction 2 (DDL-D2). (d) The diagonal double turn, current direction 2 (DDT-D2).

All geometries were first defined using a commercial electromagnetic (EM) software FEKO (EM Software and Systems, South Africa) [165]. Without any coil-rotation, we assume that the coil coordinates system $(u, v, n)$ and the MR scanner coordinates system $(x, y, z)$ are superimposed ($z$ is the B0 axis and $x$ is the vertical axis). As shown in figures 2, all copper strips were drawn with their long axis aligned along $n_{axis}$.The **uOv** plane corresponds to the horizontal plane of the MR scanner when the coil is in the reference orientation (without any coil-rotation). Simulations were carried out based on the full-wave numerical Method of Moment (MoM). The latter is a numerical technique used to solve Maxwell equations in their integral form by applying an arbitrary excitation source (with 1W power, 1 V voltage) and discretizing wires into segments and conducting surfaces into triangles in order to determine the associated current distribution in the frequency domain. The magnetic fields can hence be derived [84], [89]. So, after defining such loop geometry, a meshing of surfaces was done without the need of boundary conditions. Thus, $\boldsymbol{H}_1(u, v, n)$ magnetic field components were calculated for each loop-geometry in a plane perpendicular to the loop's main axis. In a colon MR imaging context, this corresponds to acquiring images of the colon with an imaging plane perpendicular to the local colon axis [166] which is the most relevant imaging plane for colon wall analysis.

Using Matlab software (Mathworks, Massachusetts, USA), extracted $\boldsymbol{H}_1$ components were used to deduce the magnetic induction $\boldsymbol{B}_1 = \mu\, \boldsymbol{H}_1$ with the permeability μ chosen as in the air. The effect of coil orientation with respect to the magnetic field $\boldsymbol{B}_0$ (z-axis) on $\boldsymbol{B}_1$ (u,v,n) components is given by the following 3D rotation matrices using the relationship:

$$\boldsymbol{B}_1(x, y, z) = \begin{bmatrix} 1 & 0 & 0 \\ 0 & cos\alpha & -sin\alpha \\ 0 & sin\alpha & cos\alpha \end{bmatrix} \times \boldsymbol{B}_1(u, v, n) \qquad (3.1)$$

where $\alpha$ is the rotation angles about x-axis. So as to simplify the discussion while being realistic, three coil orientations were studied related to the three groups of regions defined in figure 1 corresponding to the coil-navigation in the colon during an MR examination:

1. In the vertical regions, the orientation will be assumed to be 0°. We here suppose that the coil design including the outer packaging will represent a cylinder of diameter 10 mm which therefore fits tightly within the colon leaving little possibility for the coils to adopt a different orientation to that of the colon.

2. The horizontal region corresponds to an orientation of 90°. It should be noted that this the region where we expect the worst B1 uniformity since in this orientation, we expect signal cancellations. Again, in this region as in the vertical regions, we will suppose that the coils will not be able to adopt a different orientation to that of the colon.

3. In the tilted regions we have assumed that the coil orientation will be 45° which we take to be the highest rotation in these regions and therefore the worst possible case. This is of course a very simplified picture of the different orientations that may occur in the sigmoid or extremities of the transverse colon.

In the imaging procedure, it is assumed that the slice selection orientation will always be orthogonal to the main axis of the coil [166]. Thus, the resulting $B_{1x,y}$ in the transverse plane (xOy) is given by:

$$B_{1x,y} = \sqrt{B_{1x}^2 + B_{1y}^2} \tag{3.2}$$

Then, signal-to-noise ratio (SNR) distributions can be assessed using the following relationship [29], [73], [102]:

$$SNR = \frac{peak\ signal}{RMS\ noise} \propto \frac{B_{1xy}}{I\sqrt{R_t}} \tag{3.3}$$

In this expression, $I$ is the current following in the coil-loop and $R_t$ is the total resistive losses. Thus in this work we will only consider the term $\frac{B_{1x,y}}{I\sqrt{R_t}}$ as a measure of the effect of the reception coil on the SNR.

Both current I and losses $R_t$ are estimated by the electromagnetic simulations using FEKO software. Adding a very small load (1mΩ) in series with each loop enable estimation of the exact current flowing inside each portion of the loops. Losses calculations were derived from the simulated reflection coefficient ($S_{11}$) responses in both unloaded and loaded coil states.

To avoid a long simulation time, $S_{11}$ responses were first numerically simulated only at the resonance frequency (63.87 MHz corresponding to a 1.5T magnet) and optimal tuning and matching capacitors were found using an optimization method. When getting the best possible matching at this specific frequency, the coil loop was simulated again on a span of 10 MHz frequency. These steps were followed for both unloaded and loaded coils and yielded unloaded and loaded $S_{11}$ responses. The quality factor Q (which is one

of most important quantities used to test the coil performance) in loaded and unloaded conditions were derived from each $S_{11}$ response at -3 dB bandwidth [139], [141]. Losses effect ($R_t$) were then estimated from simulated unloaded and loaded quality factor ($Q_{u\_simu}$ and $Q_{l\_simu}$) values.

Since an RF coil can be considered as an RLC circuit, a theoretical way to estimate the unloaded coil quality factor $Q_{u\_theo}$ is given by:

$$Q_{u\_theo} = \frac{2\pi F_0 L_{coil}}{R_{coil}} \tag{3.4}$$

Where $F_0$ is the Larmor frequency, $L_{coil}$ is the inductance of coil conductors and $R_{coil}$ is the estimated coil resistances. Under this condition of unloaded coil, losses are represented by equivalent electrical resistance of the coil ($R_{el}$). The latter can be computed by setting equal both $Q_{u\_theo}$ equation and $Q_{u\_simu}$ simulated value therefore giving:

$$R_{el} = \frac{2\pi F_0 L_{coil}}{Q_{u\_simu}} \tag{3.5}$$

The coil-loop inductance was also estimated and derived from Smith abacus. This was done by simulation of the loop at the desired resonance frequency (63.87 MHz) without adding the lumped elements (tuning and matching capacitors). Thus, a first estimation of the electrical resistance of the conductor loop can also be derived to check for consistency of the computed$R_{el}$.

In the case of loaded coil, simulations were done using a phantom consisting of a cylindrical vessel with a through-hole (9.2 mm inner and 45 mm outer diameters, 50 mm long) allowing the introduction of each coil loop and filled with a solution of 1.25g NiSO4 x 6H2O + 5g NaCl per liter of distilled water mimicking tissue losses (Fig. 3-6). The phantom is the dielectric medium which has electrical proprieties of about of 0.67 S/m conductivity, 94.73 relative permittivity/dielectric constant and 1120 kg/m3 mass density [167].

For all the simulations, the phantom was meshed with 2mm local mesh size (this was the maximum resolution enabled by FEKO and our hardware). For unloaded coil-loops, the mesh was of 0.5 mm, 1 mm and 0.01 mm for triangle edge length, wire segment length and wire segment radius, respectively. Each loaded coil-loop was meshed with a custom mesh of 0.25 mm, 0.5 mm and 0.01 mm for triangle edge length, wire segment length

and wire segment radius, respectively. Also, EM simulations were performed using double precision numerical computations.

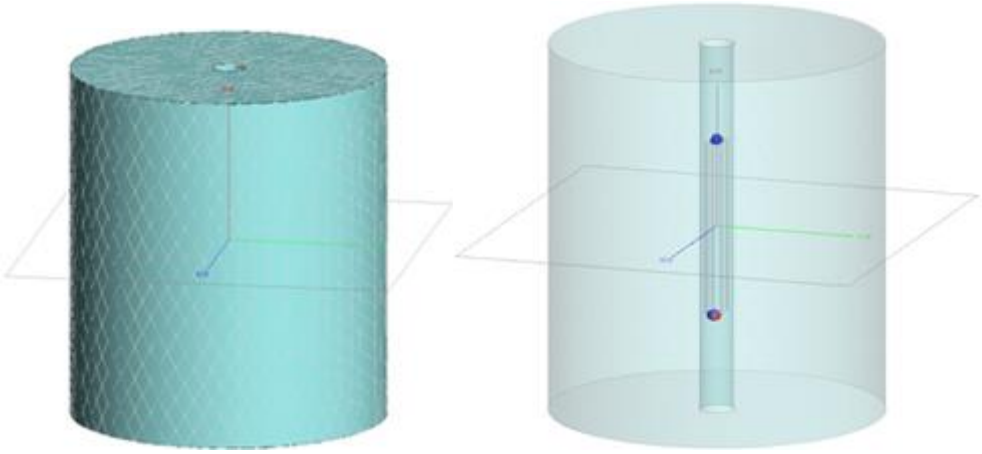

**Fig. 3-6.** The used phantom for simulation of different loaded coil-loops.

Similarly to the previous case, a theoretical way to estimate the quality factor $Q_{l\_theo}$ of the loaded coil is given by:

$$Q_{l\_theo} = \frac{2\pi F_0 L_{coil}}{R_{el} + R_m} \tag{3.6}$$

where $R_{el}$ is the electrical resistance losses due to the coil-loop and $R_m$ is the magnetic resistance losses due to the phantom. Under these conditions, $R_m$ is given by:

$$R_m = 2\pi F_0 L_{coil}\left(\frac{1}{Q_{L_s imu}} - \frac{1}{Q_{u_s imu}}\right) \tag{3.7}$$

The total loss resistance $R_t$ was then the sum of electrical resistance of the coil and magnetic resistance of the phantom and was given by [58], [106]:

$$R_t = R_{el} + R_m \tag{3.8}$$

The $\frac{B_{1x,y}}{I\sqrt{R_t}}$ term (which is proportional to the SNR distribution) of each loop geometry was then calculated. They were analyzed in regions close to the coil which corresponds to colon wall location. By using Matlab software, intensity values and radial uniformity of signal distributions were assessed in a region defined by a disc centered on the coil axis and having 5 mm and 15 mm inner and outer radiuses (the targeted colon wall imaging area). To achieve that, $\frac{B_{1x,y}}{I\sqrt{R_t}}$ values were calculated on concentric circles (with 10° angle sampling from 0° to 360°), for each chosen distance and specific coil orientations with

respect to $B_0$. As already mentioned it is assumed that the coil loop rotates around x-axis with an angle $\alpha$ = 0°, 45° and 90°.

Finally, geometries providing the best signal uniformity at the different coil orientations and for different imaging distances were compared. They were then combined in a theoretical single reconfigurable endoluminal coil using MEMS switches [68].

The Fig. 3-7 summarizes the different steps from the design of the loop-geometry until the results analysis.

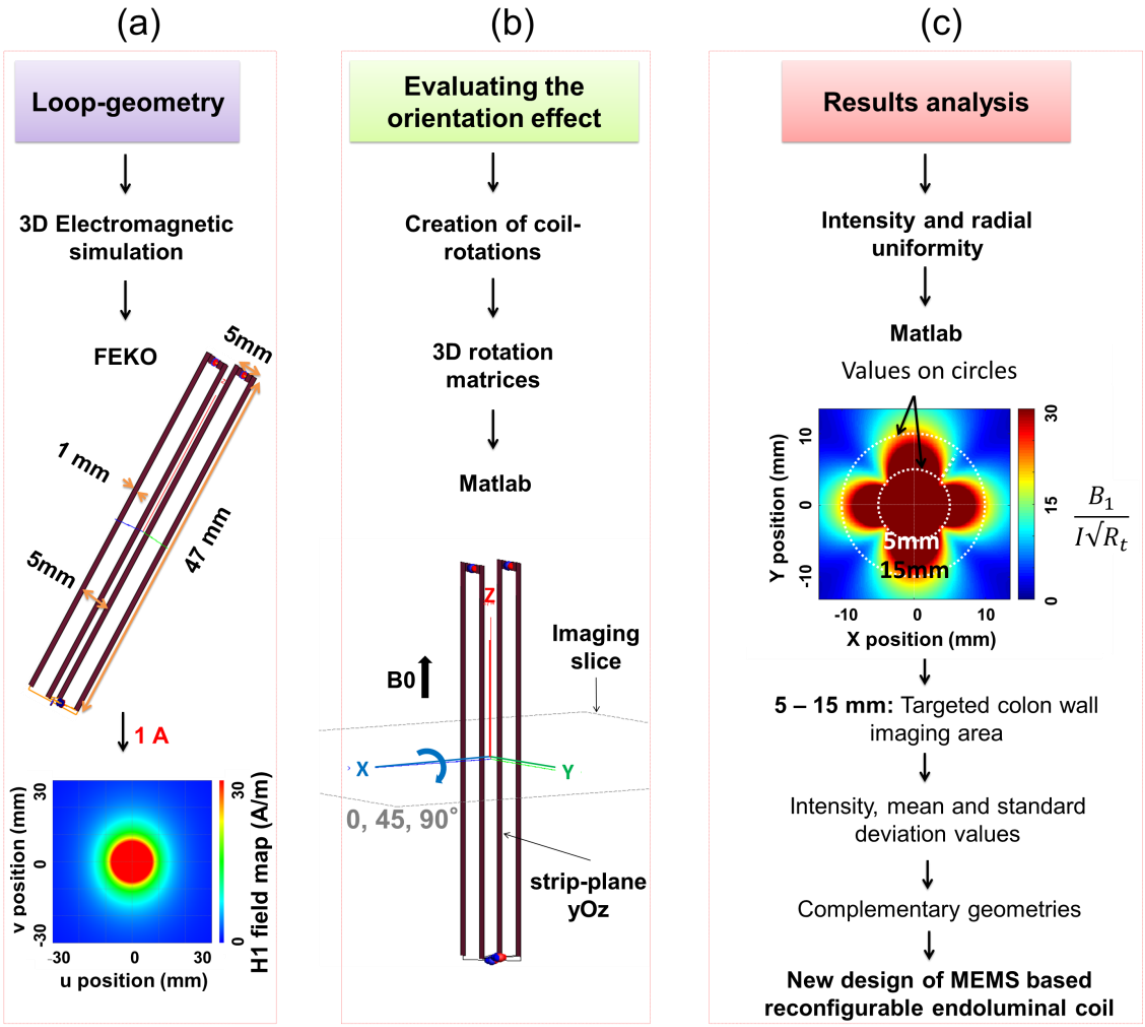


**Fig. 3-7.** Different steps from the coil-design to the results analysis. (a) The full wave electromagnetic simulation with FEKO software to get the magnetic field H1. (b) Application of the coil-orientations effect about x-axis on $\boldsymbol{B_{1x,y}/I\sqrt{R_t}}$ (which is proportional to the SNR) distributions by using Matlab software (3D-transformation based on rotation matrices). (c) The result analysis corresponding to the chosen criteria: coefficient of variations between 5 mm and 15 mm from the center of the coil (targeted colon wall imaging area).

## 3.1.3. Results

So as to evaluate the performance of the different loop geometries presented in the method section, we have run comparisons in two steps. First, the four configurations of double loops were evaluated so as to determine the one which would be best suited for endoluminal colon imaging. In a second step, the chosen double loops configurations were compared to the diagonal single loop (DSL) since it is the state-of-the-art reference solution.

**Part I: Unloaded rectangular and diagonal double layer/turn loops**

In this section, only results of unloaded coils will be presented since the simulated values of $R_m$ for the double layer/turn loops are much smaller than $R_{el}$. Therefore unloaded and loaded simulations will lead to almost the same conclusions. Results of $\frac{B_{1x,y}}{I\sqrt{R_t}}$ values (which are proportional to signal intensity) of rectangular and diagonal double loops, sampled every 10° on circles of radii 10 mm (centered on the loop center) are displayed in Fig. 3-8. As can be seen configurations that display higher $\frac{B_{1x,y}}{I\sqrt{R_t}}$ intensity also tend to have higher variations with respect to the sampling angle. From the sampled values, means and standard deviations were calculated and the subsequent coefficient of variations (CV = standard deviation/mean) derived. The corresponding CVs for the different geometries and in the reference orientation (0°) are displayed in Fig. 9. The RDL-OC and RDT-OC offer smaller CVS than the DDL or DDT are therefore, RDL-OC and RDT-OC are the two geometries which will be considered for the rest of this work.

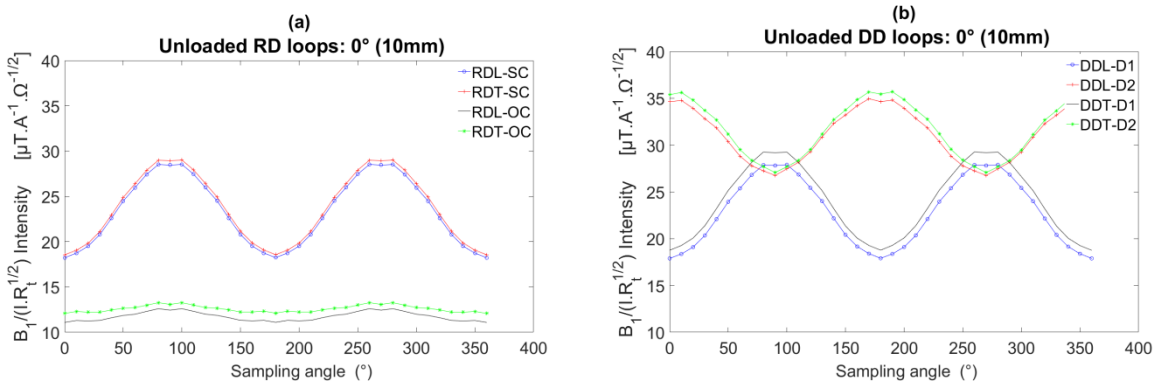


**Fig. 3-8.** Unloaded $\frac{B_{1x,y}}{I\sqrt{R_t}}$ intensity versus sampling angle for (a) rectangular double loops and (b) diagonal double loops at reference orientation and at 10 mm distance from the loop-center at reference orientation (0°).

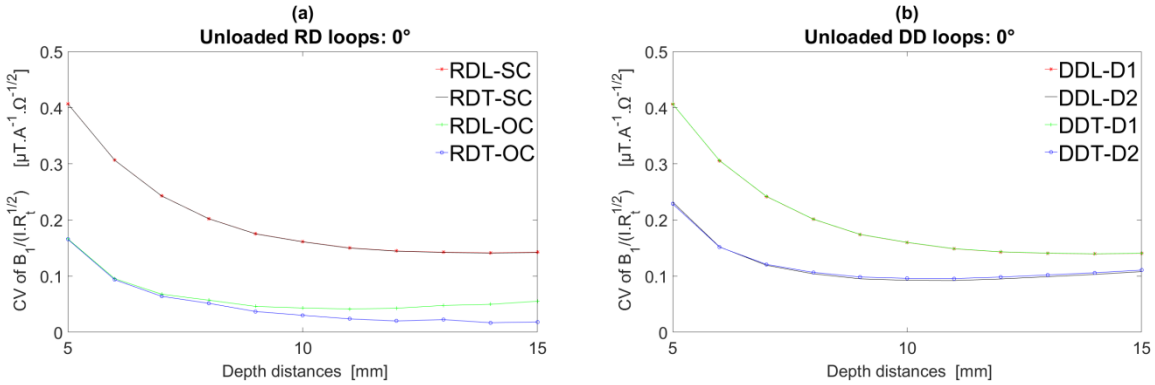


**Fig. 3-9.** The CVs (coefficients of variation) versus distances of unloaded (a) rectangular double (RD) loops and (b) diagonal double (DD) loops with loops in the reference orientation (0°).

## Part II: Loaded single and double loops

These two selected geometries (RDL-OC and RDT-OC) were compared to the diagonal single loop (DSL) and for orientations of the loops about x axis of 0°, 45°, 90° and at different distances (5 to 15 mm) from each loop-center. This time all simulations were run in loaded conditions since simulated $R_m$values were quite different between the DSL and double loop geometries.

For each distance, $\frac{B_{1x,y}}{I\sqrt{R_t}}$ intensity values were sampled every 10°. Then means and standard deviations (calculated on concentric circles) were calculated for each loop (RDL-OC, RDT-OC and DSL). Means and coefficients of variations (CV = standard deviations/mean) of $\frac{B_{1x,y}}{I\sqrt{R_t}}$ versus distances from each loop-center (from 5 to 15 mm) and for the three specific orientations mentioned above (0°, 45° and 90°) were specifically studied.

### Mean of $\frac{B_{1x,y}}{I\sqrt{R_t}}$ versus distances at specific RF loop-rotations

As shown in Fig. 3-10, mean signal intensity (mean $\frac{B_{1x,y}}{I\sqrt{R_t}}$) values for all loops dropped-off rapidly when moving away from the loop-center. The DSL presented mean $\frac{B_{1x,y}}{I\sqrt{R_t}}$ values higher than the other loops for all distances and loop-orientations. Obtained mean $\frac{B_{1x,y}}{I\sqrt{R_t}}$ values of RDL-OC and RDT-OC displayed nearly identical mean values for all distances and for the three considered orientations. However, their mean values were also inferior to those of the DSL in all the tested conditions.

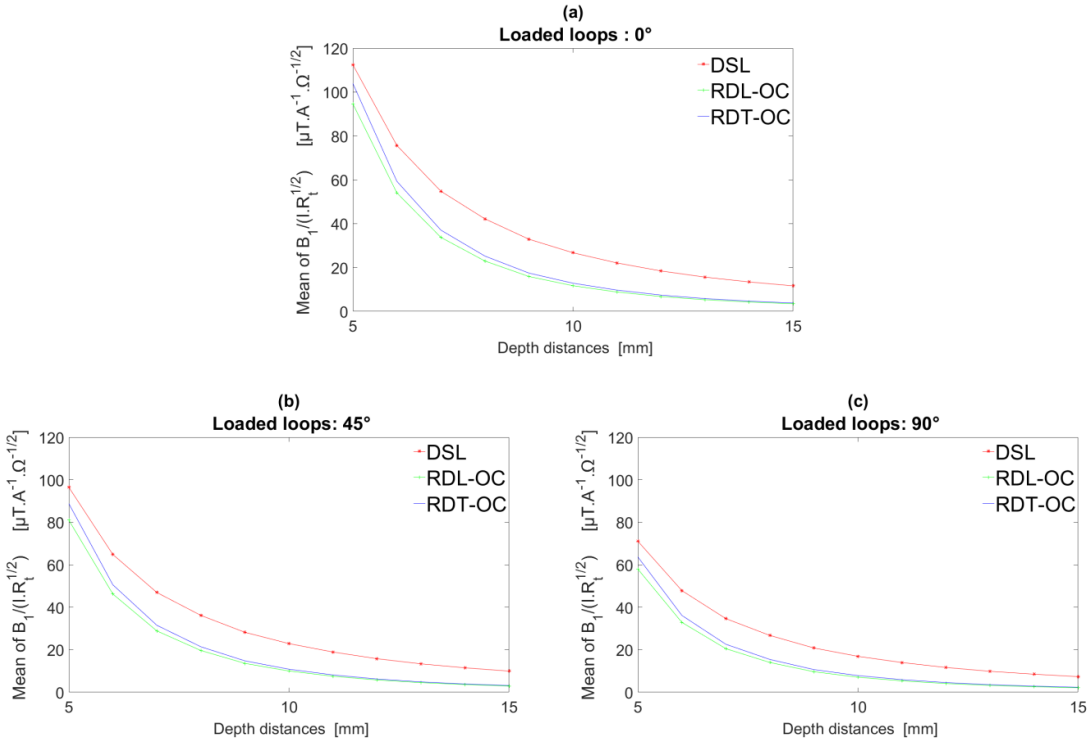


**Fig. 3-10.** Means of $\frac{B_{1x,y}}{I\sqrt{R_t}}$ ratio (calculated on concentric circles) versus distances from each loop-center (from 5 to 15 mm) at specific orientations with respect to X-axis: angles of (a) 0° (b) 45° and (c) 90°.

### Coefficients of variations (CV) of $\frac{B_{1x,y}}{I\sqrt{R_t}}$ versus distances at specific RF loop-rotations

Coefficients of variations for the three geometries and for distances between 5 and 15mm are plotted in figures 8 (a) to (c) corresponding to the three investigated orientations (0°, 45° and 90°). At the reference orientation (Fig.3-11a) and for distances inferior to 9 mm, CV values of RDL-OC and RDT-OC were very close to each other and smaller than those displayed by the DSL. Between 9 and 12mm the DSL is the geometry displaying the smallest CV but above 12mm it is the RDT-OC which displays the smallest CV. At 45° loop-orientation (Fig.3-11b), the RDT-OC and RDL-OC geometries show the smallest CV until 8mm but above, the DSL is the best suited geometry. By further increasing the loop-rotation angle and in particular at the 90° position (Fig.3-11c), the DSL exhibits the smallest CV for all distances.

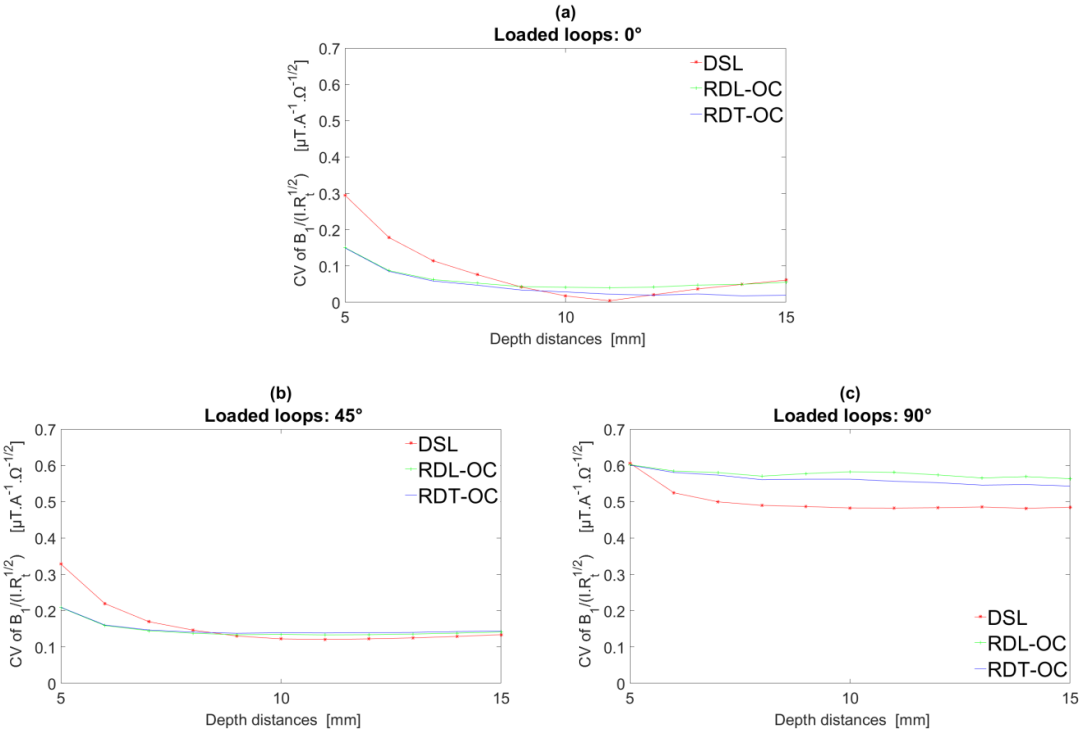


**Fig. 3-11.** Coefficients of variations (CV) of $\frac{B_{1x,y}}{I\sqrt{R_t}}$ ratio (calculated on concentric circles) versus distances from each loop-center (from 5 to 15 mm) at specific orientations with respect to X axis: angles of (a) 0° (b) 45° and (c) 90°.

## 3.1.4. Discussion and Conclusion

In our application the coil is placed very close to the region of interest. This leads to very high signal intensities close to the conductors. However, there is a rapid signal decrease when moving away from the coil center as can be observed in all surface coils [26]. Starting from a given coil geometry with given positions of conductors, multiple single-channel double turns/layers models were designed and compared to a diagonal single loop geometry which will serve as reference. In this study, we focused on the combination of the two main criteria: signal intensity and variations characterized by the mean and standard deviations measured on concentric circles centered on the coil center. These two measures were combined to obtain coefficients of variations which will reflect signal uniformity in the regions of interest.

In a first step, obtained simulation results of different configurations of rectangular and diagonal double loops led to select rectangular double layer and turn with opposite current directions (RDL-OC and RDT-OC) since they were the ones which displayed the smallest CVs. This is mainly related to the intensity values which are less than those of rectangular double layer and turn with same current directions and thus less variation.

In a second step, simulation results of the different loaded single and double coil-loops were studied for distances ranging between 5mm and 15mm and for three specific orientations. As mentioned in the method section, the choice of the three orientations was made according to plausible orientations of the coil during navigation in the colon during an MR examination. In vertical regions (rectum, descending colon and ascending colon), we assumed that each coil is oriented at 0° with respect to the x axis. In this case, the RDL-OC and RDT-OC presented the best signal uniformity at low distances (<9 mm). For distances between 9 and 12 mm, the DSL exhibits higher signal intensity and smaller CV. Above 12 mm, the RDT-OC exhibits smaller CV.

In horizontal regions (medium part of transverse colon), we assumed that each coil has operated at 90° rotation around the x axis. The DSL presents the best signal uniformity for all considered distances. This is understandable since for this particular orientation, the RDL-OC and RDT-OC both have their coil planes perpendicular to B0 (which is the worst-case scenario for signal uniformity) whereas the DSL due to its particular plane orientation has its normal to the coil plane at 45° to $B_0$. Thus, the DSL appears to be the best solution in this case. It should be noted that rotating the DSL by a further 45° but this time around the y-axis would enable an even better signal uniformity since the coil plane would then lie in the horizontal plane of the MR scanner. However this is not within the scope of work which considers reconfiguration and not re-orientation of coils.

In tilted regions (sigmoid and the two extremities of the transverse colon), we assumed that each coil was oriented at 45° with respect to x axis. In this case, the RDL-OC and RDT-OC present the best uniformity up to 8 mm and the DSL for higher distances (>8 mm).

To summarize, after analysis of these simulated results given by every individual geometry, the selection of complementary loop-geometries emerged as a relevant possibility to provide improved robustness regarding the coil-orientations. It is now necessary to see how it would be possible to switch between these three geometries using MEMS.

## Proposed design of MEMS-based reconfigurable endoluminal coil

The proposed MEMS-based reconfigurable endoluminal coil (swiM RE-Coil) design is illustrated in Fig. 3-12. It consists of using only four copper strips and two electronic units (Fig. 3-12a). The latter include sets of capacitors and MEMS switches located at the proximal and distal parts of the loop (Fig. 3-12b). It should be noted that the inclusion of MEMS switches is not such an easy task. In a previous work [168], a single MEMS switch was included in a rectangular single loop design of such an endoluminal coil and validated

with optimal performances not only in terms of active decoupling but also for image quality. Although the switch in itself is fairly small, it requires the additional use of other driver circuits which are quite bulky with respect to the present context of endoluminal imaging. These can be remotely located but this then requires that activation signals be transported using galvanic conductors which raises further issues. Thus, during the design process, care was taken so as to minimize the number of required MEMS switches which is equal to four in our present design.

It is possible to use the RDT-OC but it requires the use of more components (MEMS and capacitors). For this reason and given that at the reference orientation (0°) the CV of the RDT-OC is only marginally better that that of the DSL above 12 mm, in the proposed design, only the RDL-OC and DSL have been considered such that the final design includes :

- At 0°: RDL-OC below 9 mm and DSL above 9 mm
- At 45°: RDL-OC below 8 mm and DSL above 8mm
- At 90°: DSL

The active decoupling state is ensured by opening all MEMS switches: S1 to S4. This ensures that there is no closed loop in the design (Fig. 3-12c). The DSL loop-geometry is obtained by closing S1, S2 and opening all other switches (Fig.3-12e) and it is used at high distances for vertical and tilted regions and in all conditions for horizontal regions. Finally, the RDL-OC is obtained by closing S3, S4 and opening all other switches (Fig.3-12f) and it is used at low distances for titled and vertical regions.

Other more complicated geometries could theoretically be considered for example, in the horizontal regions of the colon, a reconfiguration of the RDL-OC geometry so as to create a loop plane in the yOx plane could be done. However, adding this configuration to the proposed design would require an important number of MEMS switches and capacitors which would be too bulky for endoluminal application and was therefore ruled out in the current work.

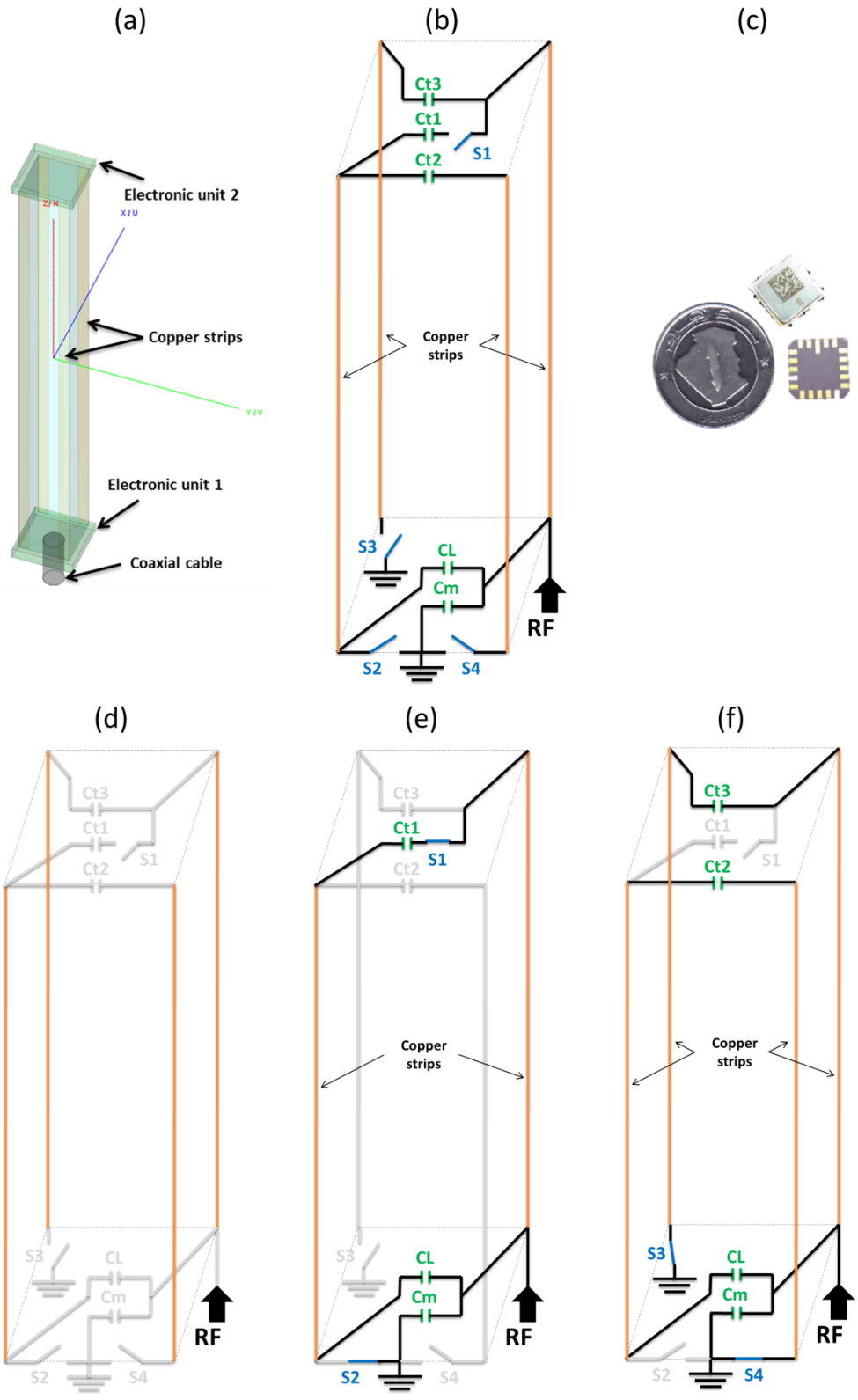


**Fig. 3-12.** (a) The proposed and (b) detailed MEMS-based reconfigurable endoluminal coil design. (c) The MEMS switch (1 cm x 1 cm). (d) The active decoupling state. (e) The DSL loop-geometry. (f) The RDL-OC geometry.

In conclusion, endoluminal MR imaging is actually the best alternative to get the required SNR per unit time enabling proper visualization of colon wall layers. However, signal distribution (intensity and uniformity of the coil-sensitivity) is affected during coil navigation within the colon since it leads to modifications of coil orientations with respect to the static magnetic field. Reconfiguration of coil loop geometries according to the colon area (coil-orientations) and distance from the coil center is an interesting way to reduce this dependency and thus improve the coil-sensitivity uniformity and image quality. To achieve the switch between loop-configurations, the use of MEMS switches is an attractive solution but in practice is still a challenge in the case of endoluminal imaging where available space and component sizes are critical. The proposed design of reconfigurable endoluminal coil is based on four MEMS switches and permits not only to switch between RDL-OC and DSL but also to achieve an accurate active decoupling of the endoluminal coil during the RF transmission of an MR experiment.

Further work will have to be carried out to assess the feasibility of such a coil and also to evaluate the experimental performance of such a solution. Indeed, as seen in the second chapter, the addition of MEMS switches in a coil does have a negative impact on the coil quality factor and therefore on the obtained images.

## Acknowledgments

Authors would like to thank GE Healthcare, Inc. and ANRT for funding this project. This work was conducted in the scope of the LABEX PRIMES of University of Lyon (ANR-11-LABX-0063), within the program "Investissements d'Avenir" (ANR-11-IDEX-0007) operated by the French National Research Agency (ANR).

Another design used for $^{31}P$ spectroscopic imaging and $^{1}H$ imaging has been proposed and simulated by using a MEMS reconfigurable $^{1}H/^{31}P$ rectal coil.

# 3.2. Design of MEMS reconfigurable $^{1}H/^{31}P$ rectal coil for spectroscopic imaging using automatic tuning, matching and active detuning

## Synopsis

External dual-nuclei RF coils provide complementary diagnosis information that cannot be provided by the use of proton-coil only. However, this requires the use of double-channel coils which represents a challenge in the case of the endoluminal imaging. We designed and simulated a reconfigurable single-channel coil-loop, able to operate as a proton ($^{1}H$) or as a phosphorous ($^{31}P$) inner coil introduced by sphincter for MR spectroscopy and imaging. Simulation results with simple reconfiguration circuit allows the sequential operation of the coil at the $^{1}H$ and $^{31}P$ frequencies with efficient decoupling driven by 2 MEMS.

### 3.2.1. Introduction

External dual nuclei RF coils, such as the proton in combination with phosphorous (used in sequential mode), based on two different tuned loops is used for MR examination yielding complementary information [169], [170]. In the case of rectum cancer, dedicated endoluminal coils have the advantage of being introduced with minimum invasion inside the rectum to be close to the region of interest thus enabling high SNR and spatial resolution. However, in the context of endoluminal MR imaging, using two different loops represents a challenge mainly due to space restrictions. In addition, the endoluminal coil has to be detuned when operated in association with a separate 1H transmit coil. A recent study [168] demonstrated the feasibility of using MEMS (Micro Electro Mechanical System) switches [63], [68], [69] for endoluminal RF coils decoupling while preserving good performances. In this study, we propose the design of single-channel reconfigurable endoluminal coil using MEMS switches to shift between $^{1}H$ and $^{31}P$ for MR imaging and/or spectroscopy and also for active detuning purposes.

## 3.2.2. Methods

Using electromagnetic FEKO software, a single-channel endoluminal $^{1}H/^{31}P$ coil was designed with a unique single RF-loop (5 mmx 47mm) including two MEMS and 4 capacitors (Fig. 1a,b), and then simulated with the Method of Moment [84]. The MEMS were considered ideal switches. Coil active detuning is achieved with the exploitation of the MEMS switches by closing MEMS 1 and opening MEMS 2 (Fig. 1c). In tuned mode, opening both MEMS led to match and tune the coil-loop to 50 Ω and at the proton Larmor frequency $F_{0H}$ of 64 MHz at 1.5 T (Fig. 1d). Finally, by closing both MEMS, this frequency is shifted to retune the coil at the phosphorous Larmor frequency $F_{0P}$ of 26 MHz at 1.5 T while also ensuring impedance matching (50 Ω) (Fig. 1e). The tuning and detuning efficacy modes were assessed by determining $S_{11}$ amplitudes at both $F_{0H}$ and $F_{0P}$. Then, magnetic field ($H_{xy}$) profiles and distribution were extracted in tuned modes and at each resonance frequency.

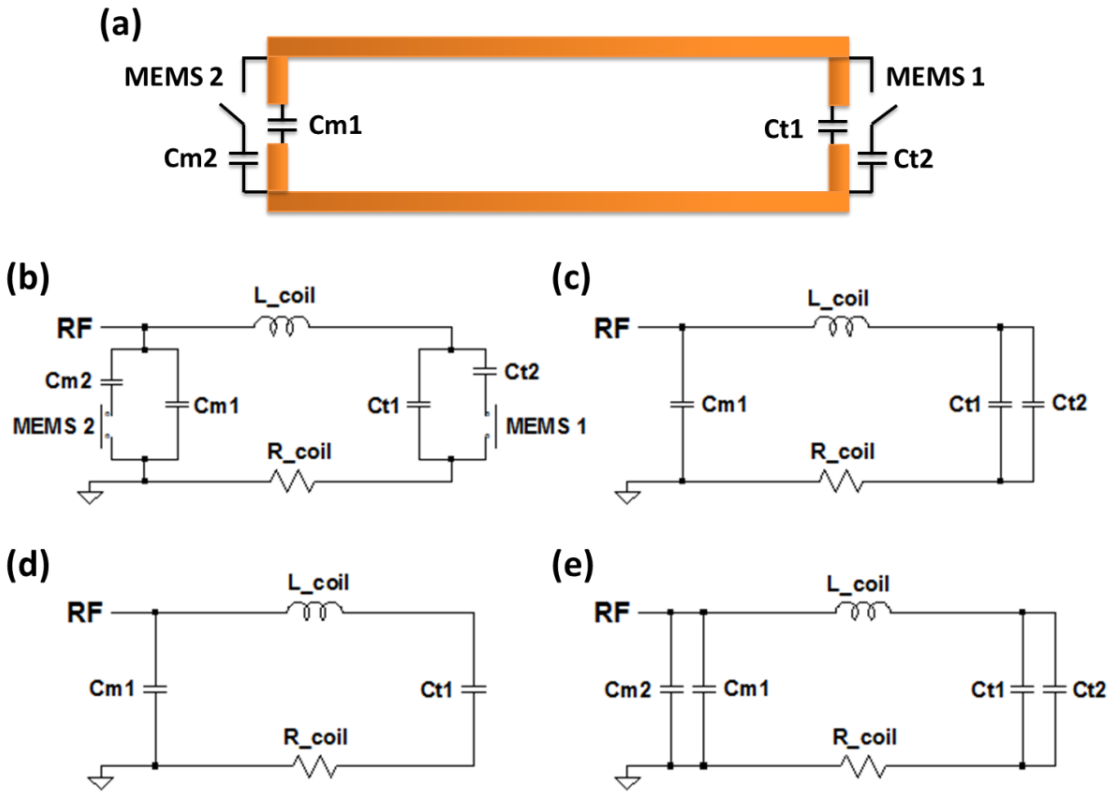


**Fig. 1.** Proposed (a) design and (b) electric circuit of endoluminal double tuned ($^{1}H/^{31}P$) loop coil based on two MEMS switches. Calculated capacitor values, Ct1, Ct2, Cm1 and Cm2 were 138.09 pF, 880.99 pF, 699.89pF and 1565.37pF, respectively. (c) The active detuning configuration of the loop during RF transmission. (d) Equivalents circuits for (d) $^{1}H$ and (e) $^{31}P$ frequencies.

### 3.2.3. Results

As shown in Fig. 2, simulated responses of the circuit show resonance frequencies ($F_0$) at 63.87 MHz and 25.87 MHz for $^{1}H$ and $^{31}P$ coil configurations, respectively. In coupled mode, $S_{11}$ values at $F_0$ were - 124 dB and -44 dB for $^{1}H$ and $^{31}P$ coil configurations, respectively. The simulated impedances were 50 Ω for both tuned coil configurations. The -3 dB bandwidth values were respectively equal to 1.32 MHz (63.2 MHz to 64.5 MHz range) for $^{1}H$ coil configuration and 0.84 MHz (25.5 MHz to 26.4 MHz range) for $^{31}P$ coil configuration. In the decoupled mode, $S_{11}$ values at $F_0$ were 0 dB for both configurations. Impedance values (Fig. 3a) and results on the Smith Abacus (Fig. 3b) were similar for both configurations. Simulated magnetic field ($H_{xy}$) at the center of the loop along the normal line were almost similar with a slightly higher $H_{xy}$ field values for the $^{31}P$ coil configuration at all given distances as can be seen in Fig. 4. Signal distributions displayed equivalent radial uniformity (Fig. 5).

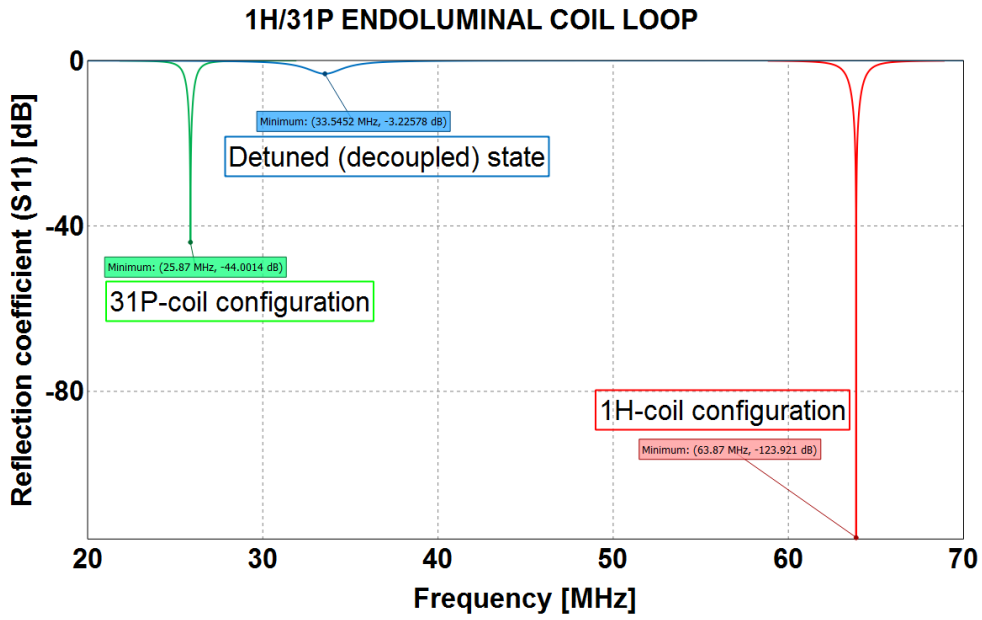


**Fig. 2.** Simulation of reflection coefficient ($S_{11}$) responses with the tuned $^{31}P$-coil configuration (in green), the tuned $^{1}H$-coil configuration (in red) and in detuned state (in blue).

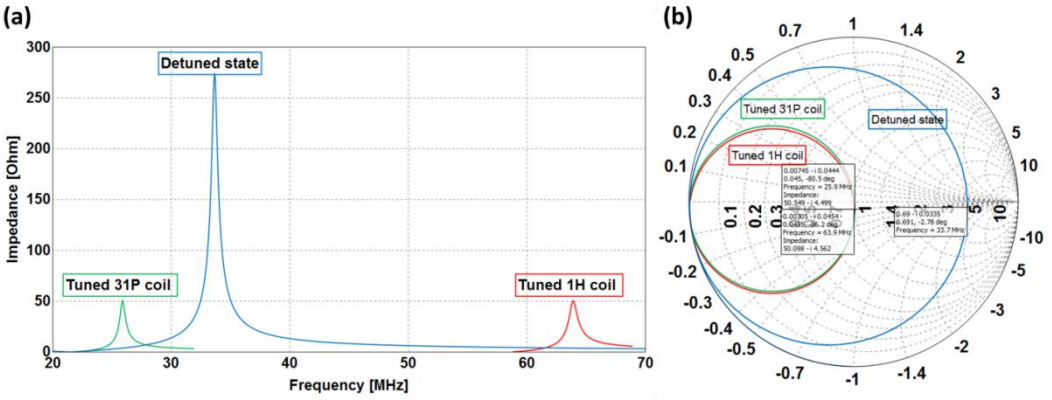


**Fig. 3.** Simulation results of (a) impedance and (b) smith abacus of the tuned $^{31}$P-coil configuration (in green), the tuned $^{1}$H-coil configuration (in red) and in the detuned state (in blue).

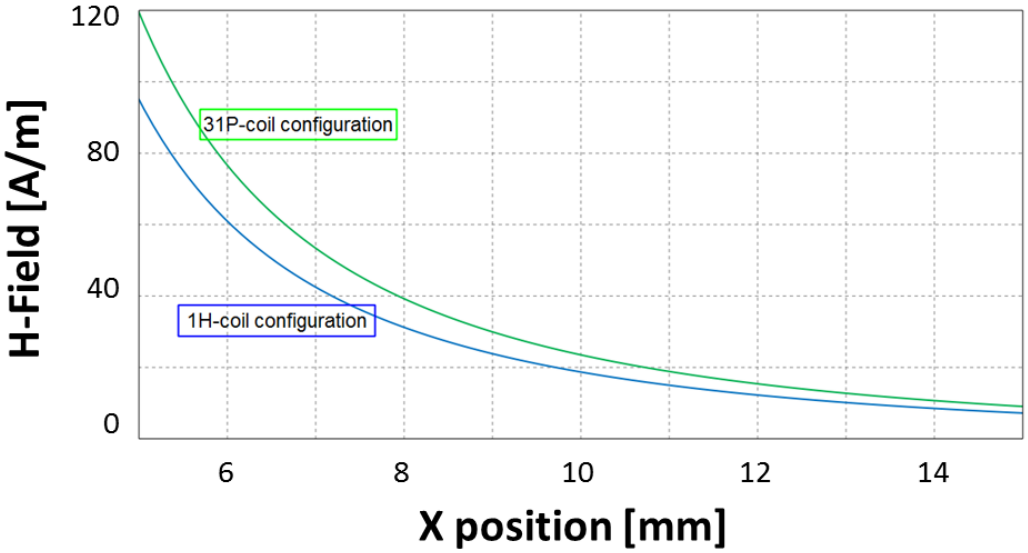


**Fig. 4.** Simulated magnitude field ($H_{xy}$) at the center of the loop along the normal line for both $^{1}$H and $^{31}$P coil configurations.

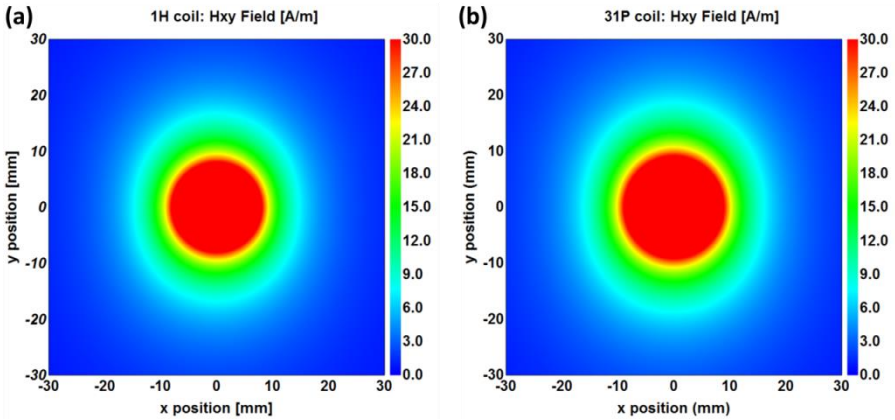


**Fig. 5.** Simulated magnitude field ($H_{xy}$) maps of (a) $^{1}$H-coil and (b) $^{31}$P-coil configurations.

### 3.2.4. Discussion

In the detuned mode, $S_{11}$ values at both $F_{0H}$ and $F_{0P}$ were 0 dB and the displayed resonance around 33 MHz is far from the -3 dB bandwidth of both resonance response (63.2 MHz to 64.5 MHz and 25.5 MHz to 26.3 MHz for $^{1}H$ and $^{31}P$ resonances respectively). This demonstrates an efficient detuning for both configurations. To obtain these results, we have supposed that the open MEMS 2 switch can be modeled by a very high impedance equivalent to an open circuit. This corresponds to removing the capacitor Cm2 in series with the opened MEMS switch (as illustrated in Fig. 1c). This hypothesis was experimentally confirmed by measurements in a recently published work [168]. Similarly, we considered that a closed MEMS 1 switch is an ideal conductor which is a simplifying hypothesis not very far from what was measured experimentally [168].

In coupling mode, $S_{11}$ values at both $F_{0H}$ and $F_{0P}$ were higher than -40 dB for both $^{1}H$ and $^{31}P$ configurations. This confirm a proper match to 50Ω when changing the loop-configuration (as seen in Fig. 3a,b). Again here the MEMS switch was considered as ideal.

The similar magnetic field profiles obtained for both configurations is mainly due to the use of the same dedicated rectangular loop geometry leading to nearly the same magnetic field decrease.

### 3.2.5. Conclusion

In conclusion, this work demonstrates the possibility of designing a single-channel rectangular endoluminal coil to explore the proton ($^{1}H$) and the phosphorous ($^{31}P$) nucleus through MR imaging or spectroscopy. This can be done by changing only the state of two MEMS switches; without the need of additional tuning, matching and detuning circuits. The main originality of this work is the use of the same coil loop design to image proton and phosphorous nuclei. It will require a routing circuit to connect the coil to depending on the configuration to the right nuclei receiver channel for proper pre-amplification and signal processing.

## Chapter conclusion

This chapter is the second part of the thesis which consists of studying the effect of coil-orientation (with respect to $B_0$ field) on the coil sensitivity of several loop geometries which were defined and simulated with FEKO software (Method of Moment solver). Complementary loop geometries were combined to design a single-channel reconfigurable endoluminal coil able to work with optimal sensitivity according to its orientation along the colon. The reconfiguration is ensured by using four MEMS switches.

The main originality of this part is to reconfigure miniature endoluminal coils by forming the dedicated loop design by only using four copper strips and not by simply switching between already existing loops.

In addition to that, another design of a reconfigurable single-channel rectangular loop able to operate as a $^{1}H$ then as a $^{31}P$ (successively) rectal coil-loop for MR spectroscopy and imaging was proposed and simulated with FEKO. This can provide additional diagnosis information which cannot be provided by the use of only proton ($^{1}H$ coils). The reconfiguration is ensured by using only two MEMS. This solution could also be used to image ascending and descending colon regions.

It should be noted that the originality of this latest part is the use of the same tuned and matched coil loop geometry to explore proton or phosphorous nuclei without the need of a circuit to retune or rematch the coil and without the need of additional active decoupling circuit (automatic tuning, matching and active decoupling).

# Manuscript conclusion

# Manuscript conclusion

The general objective of the thesis is the improvement of magnetic resonance imaging in the context of colon wall analysis which implies being able to image fine structures that lie far from the body surface. This means that external coils are not yet able to provide high enough SNRs to be able to attain sufficient resolutions to image properly the different colon layers. The use of endoluminal coils offers the advantage of being very close to the regions of interest and therefore provide very high SNRs although only locally. However using such coils implies that during colon navigation, the coil loop will have different orientations with respect to the main $B_0$ field inducing impaired signal distribution. Moreover using a receiver coil different from the transmit coil requires an active decoupling solution. In this thesis we try to address both issues using MEMS switches by first using them as decoupling element and then by proposing reconfigurable endoluminal designs using MEMS switches.

The first thesis axis is devoted to the evaluation of MEMS switches as active decoupling devices by studying their impact on both coil performance and NMR image quality. To this end, two MEMS coil prototypes based on serial or parallel active decoupling configurations were built. A third coil prototype based on the conventional circuit using PIN diode was also built to serve as a reference coil. The three prototypes were characterized on experimental benches then on a 1.5 T clinical MRI scanner using a colon-mimicking phantom. The results show that characteristics such as the quality factor, switching delays to couple/decouple the coil and signal-to-noise ratio (SNR) of MEMS coils are comparable to the reference coil. The SNR of all endoluminal coils were always superior to a commercial external array coil in the region of interest. The parallel configuration permits getting a high quality factor with a shift of coil resonance frequency while the serial configuration permits the total opening of the coil-loop. This study validates the feasibility of using MEMS switches for the design of endoluminal coils with optimal performances not only for active decoupling but also in terms of image quality.

It should be noted that the main originality of this part is the implementation of MEMS switches on the miniature single-channel endoluminal coils with optimal performances, which had never been reported in the literature before.

These encouraging results permit us to go ahead to develop the second thesis axis, which is the need to take into consideration the endoluminal navigation of the coil along the colon. This navigation induces different coil-orientations with respect to the static magnetic field $B_0$ and therefore leads to significant variations in detection sensitivity in

terms of signal intensity and uniformity (distribution), altering significantly the image quality. The goal is therefore to use MEMS switches to modify (reconfigure) the coil loop geometry according to its orientation. For this purpose, by first defining a general endoluminal outer volume, different geometries of single and double loops of endoluminal coils were defined and simulated in both unloaded and loaded cases using FEKO electromagnetic simulation software. The image sensitivity distributions (intensity and uniformity) were then evaluated for specific orientations (depending on the colon structure and regions) using Matlab software. In terms of results, each geometry has its strengths and weaknesses in terms of sensitivity intensity and uniformity. Thus, complementary geometries have been identified and combined to propose and design reconfigurable endoluminal coils based on MEMS technology and having a reduced dependency between the coil-sensitivity and its orientation inside the colon. Indeed, the reconfigurable endoluminal coil design is based on only four conductors (cooper strips) and two electronic units. The latter permits to switch between the four conductors by changing the opened or closed state of each MEMS switch, and thus to control the coil geometry. A particularity is to switch between two configurations (in function of the coil orientation): diagonal single loop (DSL) and rectangular double layer - opposite current (RDL-OC) loop-geometries. The switch between them could be achieved by opening some MEMS and closing others according to the coil-orientation inside the colon. During RF transmission, the active decoupling of the reconfigurable endoluminal coil is ensured by opening all MEMS and thus opening all coil-loops.

It should be noted that the main originality of this part is to reconfigure miniature single-channel endoluminal coils by forming the dedicated loop design (according to the coil-orientation) only by using four copper strips and it is not a simple switching between already existing loops.

Another design used for MR spectroscopy and imaging has been proposed and simulated. It enabled automatic tuning, matching and active detuning circuits at two different resonance frequencies ($^{1}$H and $^{31}$P at 1.5 T) with the use of only one rectangular single loop geometry. This study demonstrates the possibility of designing single-channel endoluminal tuned and matched coil to explore proton and then phosphorous by only changing the state of two MEMS switches; without the need of additional circuits. This solution could also be applied to ascending and descending colon regions.

It should be noted that the originality of this latest part is not only the use of the same coil loop geometry to explore proton or phosphorous nuclei without the need of a multiple-channel coil and but also without the need of additional circuits to retune or

rematch the coil and without the need of additional active decoupling circuit (automatic tuning, matching and active decoupling).

In this thesis, the use of a single-channel coil design allows to simplify the coil design and to avoid the electromagnetic coupling between loops, as in the case of multiple-channel coils.

Therefore, we have first demonstrated, through experimental benches and MRI experiments, the feasibility of using a MEMS switch on a single-channel endoluminal coil-loop with optimal performances. We have then demonstrated through electromagnetic simulations the interest of using MEMS switch technology to design endoluminal coils dedicated to the examination of colon and/or rectum organs thanks to the possibility offered by MEMS to reconfigure the coil-geometry while ensuring also the active decoupling of the endoluminal coil. We proposed the name of swiM RE-Coils (switches Mems for designing Reconfigurable Endoluminal Coils). The next step would then be to build and characterize the simulated designs on both experimental bench and images with the current size of MEMS switches. Then, the proposed reconfigurable coil-design can be further optimized against the coil orientations inside the colon. Since endoluminal imaging coils have miniature dimensions with low voltages, MEMS switch do not need the high standoff voltage (500 V) used currently for external coils which have a very large dimensions compared to the endoluminal coils. So, MEMS size can be easily reduced at least by a factor 2. If done, more MEMS switches could be used opening up new design perspectives better suited to the endoluminal application.

Despite the advantages for the use of endoluminal coils namely the very high SNR in the ROI very close to the coil, the use of coaxial cables (for RF and DC signals) still remains a technological challenge from a clinical point of view. These could be replaced by a safer technology such as optical transmission line. In the case of MEMS based endoluminal coil, it remains to be seen how to send the required DC signal through this transmission medium.

Finally, the focus on MEMS reconfigurable $^{1}H/^{31}P$ coils is an attractive way for spectroscopic imaging.

# Author’s publications and awards

# Author's publications

## Published journal article

**H. Raki** *et al*., 2020, "*Serial and Parallel Active Decoupling Characterization Using RF MEMS Switches for Receiver Endoluminal Coils at 1.5T*" in ***IEEE Sensors Journal***, doi: 10.1109/JSEN.2020.2995055

## Submitted journal articles

**H. Raki** *et al*., 2020, " *Optimization of signal distribution through simulation of various RF endoluminal loop-geometries with coil orientation: Reconfigurable loop coil using MEMS*" in journal of **Concepts in Magnetic Resonance Part B: Magnetic Resonance Engineering**.

## Conference communications

1. **H. Raki** *et al*, "*Human colon imaging: simulation of novel SwiM RE-coils*", MR engineering – RF Coils I, Virtual 28th **ISMRM** (International Society for Magnetic Resonance in Medicine) Congress, August 08-14, **2020**.
2. **H. Raki** *et al*, "*Endoluminal imaging with MEMS in series with the loop coil for active decoupling*", MR engineering – RF Coils III, Virtual 28th **ISMRM** Congress, August 08-14, **2020**.
3. **H. Raki** *et al,* "*Simulation de géométries de capteurs endoluminaux pour l'imagerie des parois du colon*", Recherche en imagerie, **JFR** (Journée Française de Radiologie) Congress, October 11-14, Paris, France, **2019**.
4. **H. Raki** *et al*, "*Design of a reconfigurable endoluminal coil using MEMS switches*", MR engineering – MRI Unplugged: Wireless, Portable & Flexible session, 27th **ISMRM** Congress, May 11-16, Montreal, QC, Canada, **2019**.
5. **H. Raki** *et al*, "*caractérisation du découplage actif d'un capteur IRM endoluminal à base de micro-commutateurs électroniques (MEMS)*", **SFRMBM** Conference, Mars 19-21, Strasbourg, France, **2019**.
6. **H. Raki** *et al*, "*Comparison of single-loop endoluminal receiver coils based on serial or parallel active decoupling circuits using controllable MEMS switches*", RF coils & arrays session, 26th **ISMRM/ESMRMB** Congress, June 16-21, Paris, France, **2018**.

7. **H. Raki** *et al*, "*Endoluminal coil-sensitivity degradation with coil-orientation effect with respect to $B_0$ field: preliminary results*", RF coils & Electronics session, 26th **ISMRM/ESMRMB** Congress, June 16-21, Paris, France, **2018**.

8. **H. Raki** *et al*, "*Endoluminal loop-sensitivity degradation with loop-orientation effect with respect to $B_0$ field: preliminary results*", Journee Scientifique **EDISS**, October 11, Villeurbanne, France, **2018**.

9. **H. Raki** *et al*, "*Endoluminal coils: Active decoupling and sensitivity dependence regarding coil orientation*", **SFR** (Structure Fédération de Recherche), December 5, Lyon, France, **2017**.

10. **H. Raki** *et al*, "*Comparison of endoluminal receiver coils based on PIN-diode, photodiodes and MEMS switches for active detuning circuits*", **ITMO TS** (Institut Thématique Multi-Organismes Technologies pour la Santé), November 21-22, Lyon, France, **2017**.

11. **H. Raki** *et al*, "*Characterization and comparison of RF MEMS switch for active detuning of endoluminal receiver coils*", MR hardware session, **ESMRMB** Congress (European Society for Magnetic Resonance in Medicine and Biology), October 19-21, Barcelona, Spain, **2017**.

# Awards

SFRMBM
SOCIÉTÉ FRANÇAISE DE RÉSONANCE MAGNÉTIQUE EN BIOLOGIE & MÉDECINE

Poster award (Methodology), **SFRMBM** Conference, Strasbourg, France, Mars 19-21, **2019**

GE Healthcare


Bronze award for "Customers determine our success", **GE Healthcare,** USA, December 21, 2017

# Appendix

## Appendix

### Appendix A

**Appendix A-2** Examples of MR coil technology.

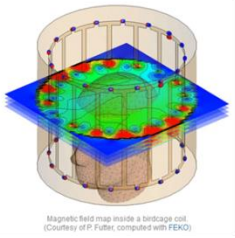


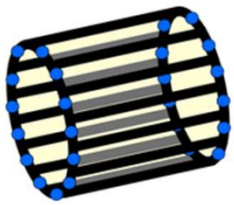

Birdcage coil design with two end rings, multiple legs/rungs, and double capacitors (blue dots).

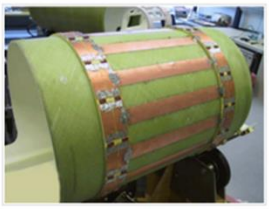

RF-body coil with birdcage design

Quadrature head coil with birdcage design

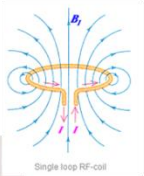


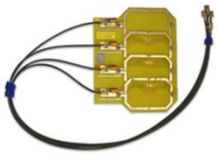

Four coil phased array showing overlapping coils

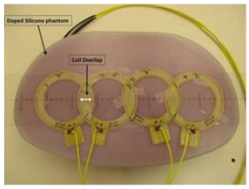


**Appendix A-3:** Examples of commercial external MR receiver coil used for medical diagnosis.

Arrays coil – GE Healthcare
(*GEM Flex Coil 16-S Array1.5T Receive Only, NeoCoil, USA*)

Body 18 long coils – Siemens Healthineers

Contour Coils – Siemens Healthineers

dStream Torso coils – Philips Healthcare

AIR Technology MRI Coils – GE Healthcare

**Appendix B**

**Appendix B-1:** Comparison of different decoupling methods for rectangular endoluminal coil (5.1 mm x 47 mm). Results obtained with PIN diode, MEMS and Optical solution (based on two photodiodes) at 3.0T MRI were comparable (H. Raki *et al.*, ESMRMB 2017).

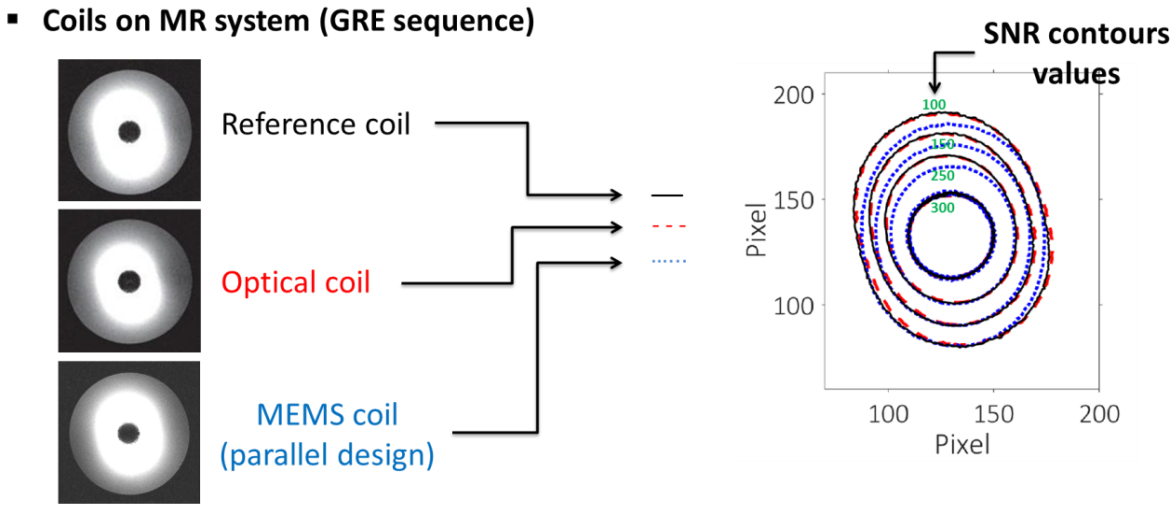


Clinical 3.0T Discovery MR-750 1.5T MRI scanner (GE Healthcare Inc.,)

**Appendix B-3:** DC Lines for MEMS with twisted wires

In the case of twisted wires used for DC lines for example, two conductors with equal impedance are twisted forming a balanced type. DC circuits (see Fig.A) can be designed to filter parasitic RF signals coupled with the DC line through two RF chokes in series and a capacitor between the DC line and the ground line [64].

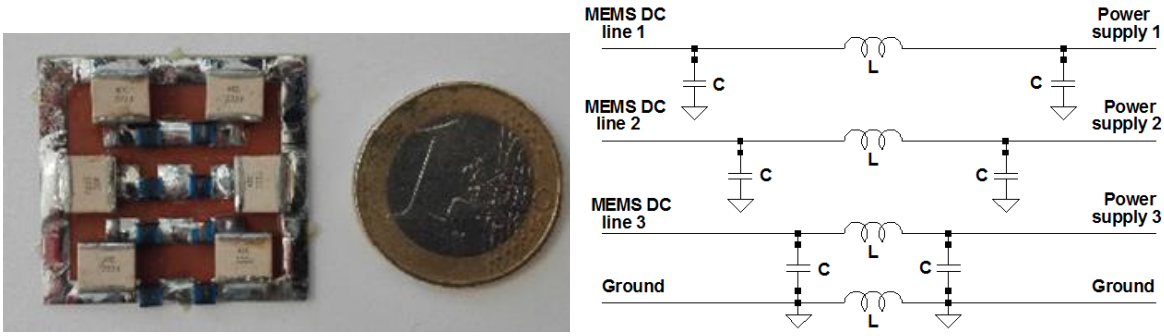


**Fig.A.** Picture (left) and schematic (right) of a DC circuit using to filter unwanted RF signals coupled with the different DC lines [64].

**Appendix B-6:** Comparison between sMEMS vs PIN diode at 1.5T, using GRE (Echo Gradient) & FSE (Echo Spin) sequences (related to the chapter 2). Similar results are obtained with GRE echo and a slight difference (but almost comparable) with FSE echo.

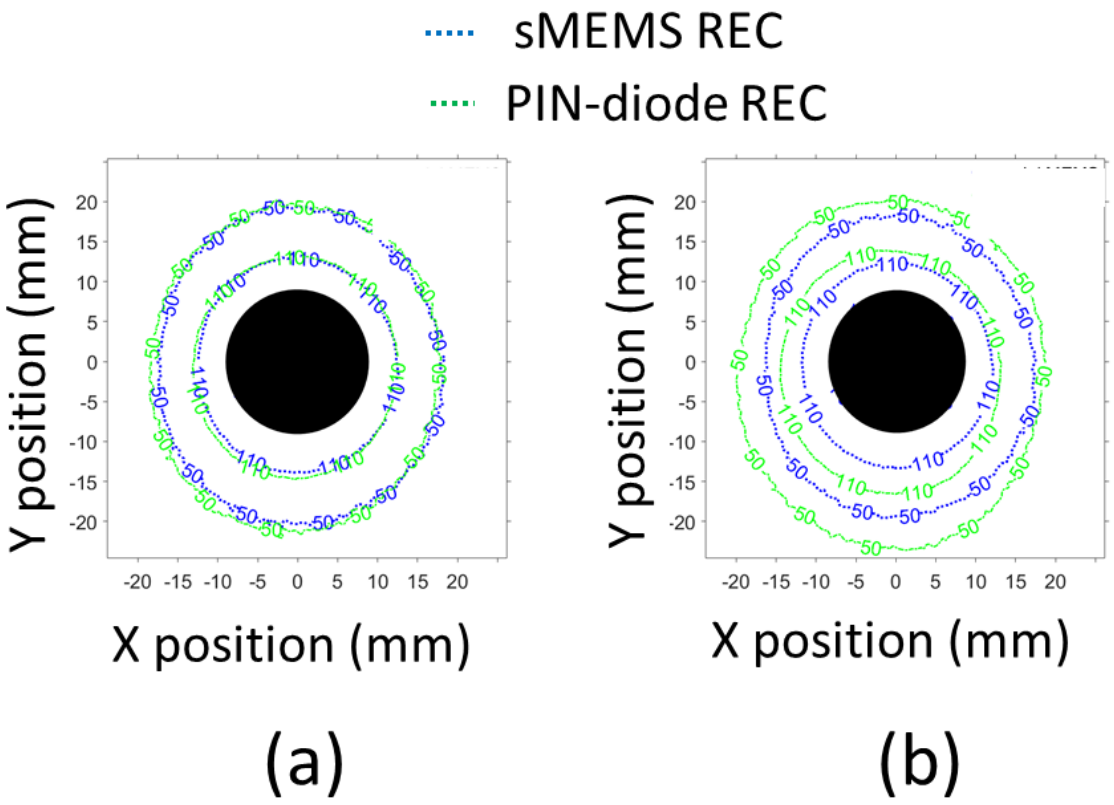


**Appendix B-7:** External MRI room and the cabling system for the external control of the MDC (Mems Driver Circuit), using a waveform generator (related to the MR experiments in Chapter 2).

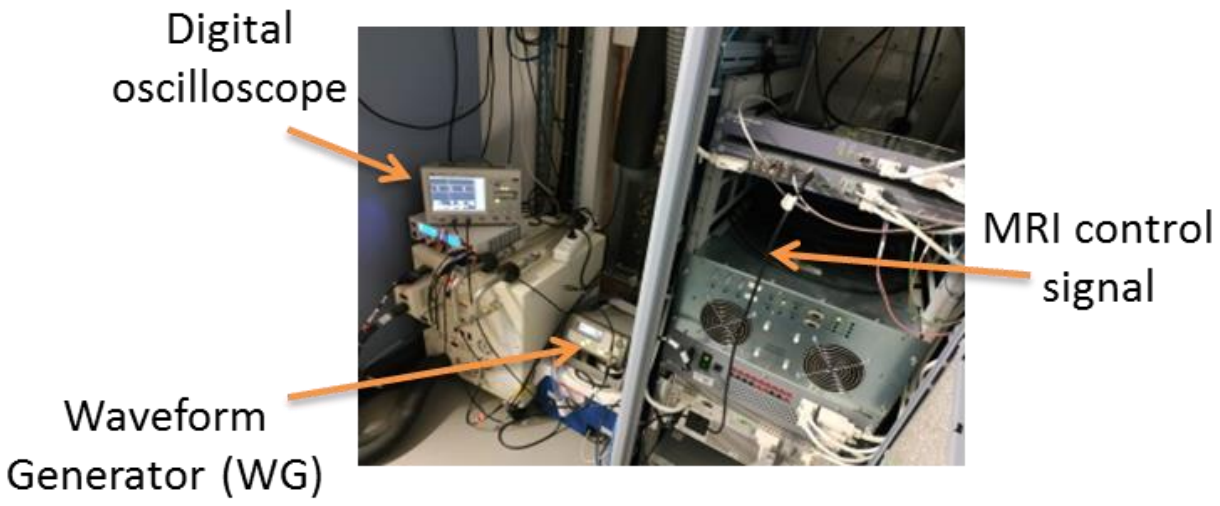


**Appendix B-8:** Waveform generator (WG) parameters for the different RECs and acquisitions.

| RECs | GRE sequence | | | | | FSE sequence | | | | |
|---|---|---|---|---|---|---|---|---|---|---|
| | Hi level (V) | Lo level (V) | Periode (ms) | Width* (ms) | Front …. | Hi level (V) | Lo level (V) | Periode (ms) | Width (ms) | Front …. |
| *p*PIN diode REC | 2.0 | - 5.0 | 30.6 | 3.6 | Negative | 2.0 | - 5.0 | 7.0 | 3.6 | Negative |
| *p*MEMS REC | 7.0 | - 5.0 | 30.6 | 27.0 | Positive | 7.0 | - 5.0 | 13.9 | 8.4 | Positive |
| *s*MEMS REC | 7.0 | - 5.0 | 30.6 | 3.6 | Negative | 7.0 | - 5.0 | 13.9 | 3.6 | Negative |

- * Width: duration of the pulse.

**Appendix B-9:** Example of possible chain between MEMS endoluminal coil and MRI system.

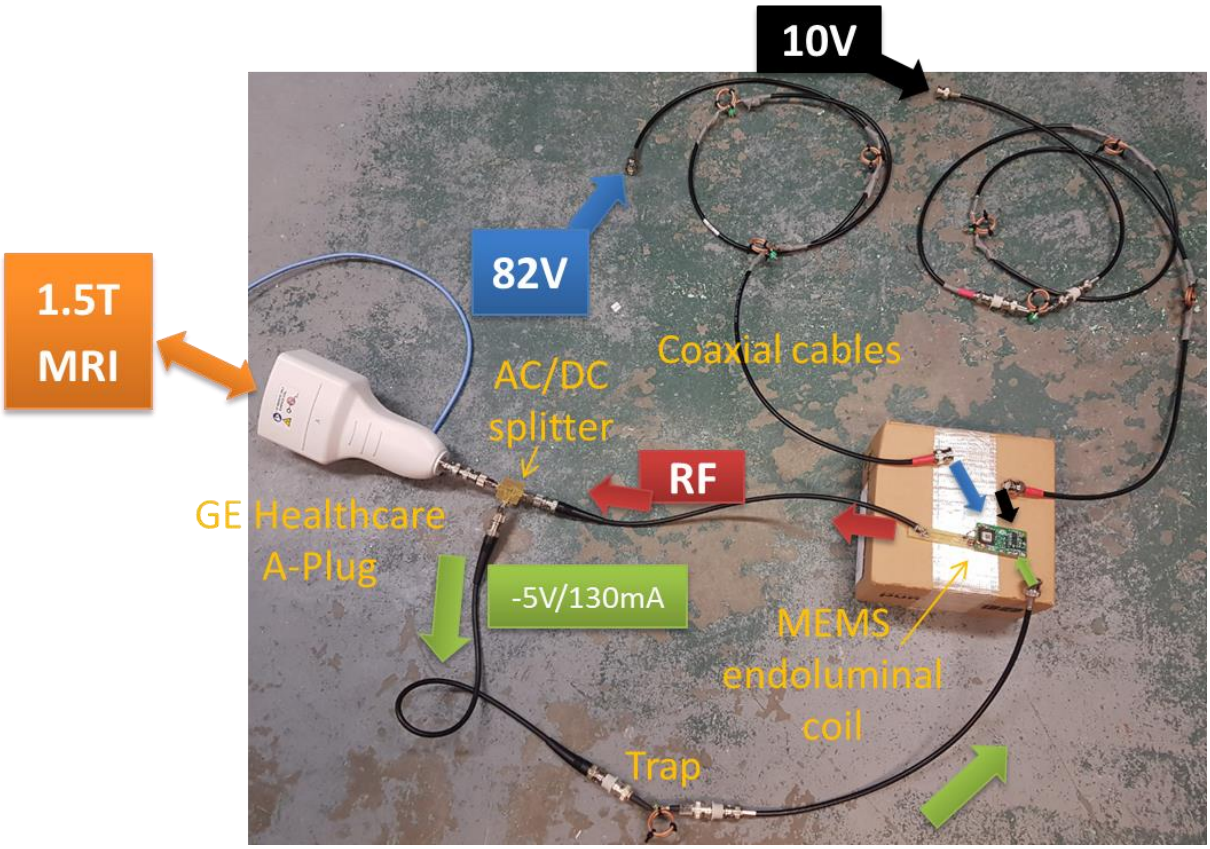


**Appendix C:** MEMS switch technology used to design novel MRI coils for colon-rectum diagnosis with respecting ergonomic aspect. The coil should be navigated or "SWIM" along the colon. This why we called: **SwiM RE-Coils.**

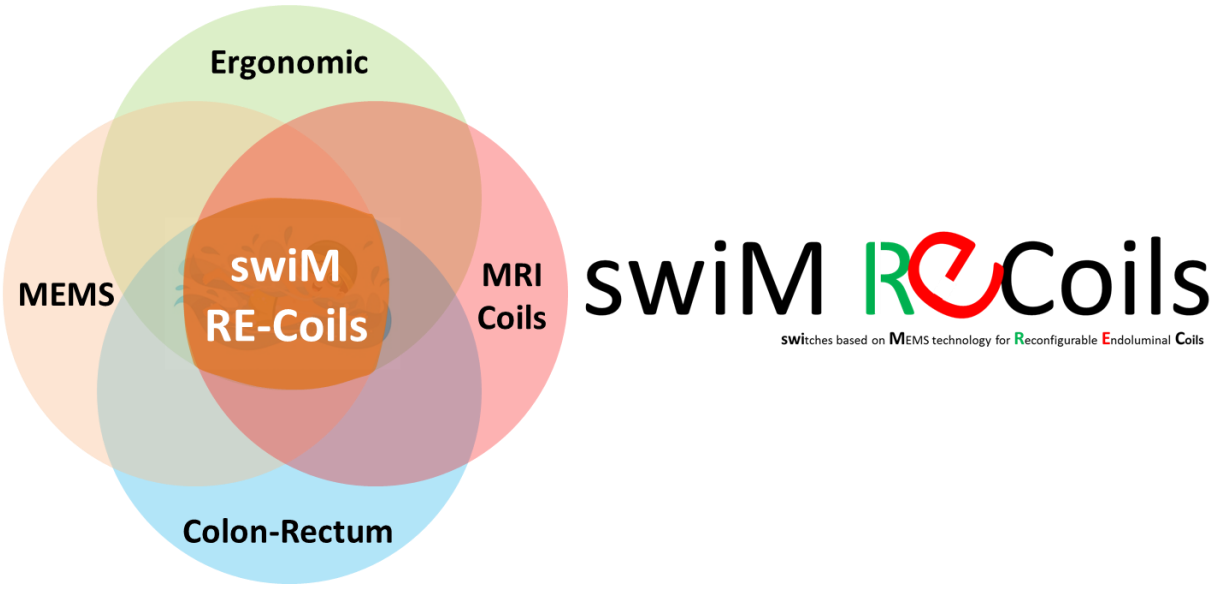

# References

# References


[1] Web1, “https://www.mayoclinic.org/diseases-conditions/colon-cancer/symptoms-causes/syc-20353669,” *Mayo Clinic*. .

[2] M. G. Gimeno *et al.*, “Diagnostic management of rectal cancer: MR vs EUS.,” *ECR 2012 PosterNG*, Mar. 03, 2012. https://posterng.netkey.at/esr/viewing/index.php?module=viewing_poster&task=&pi=108989 (accessed Apr. 22, 2020).

[3] R. L. Siegel *et al.*, “Colorectal cancer statistics, 2020,” *CA. Cancer J. Clin.*, vol. 70, no. 3, pp. 145–164, 2020, doi: 10.3322/caac.21601.

[4] Web_2, “https://www.cdc.gov/ibd/what-is-IBD.htm.” .

[5] Y. Komaki, F. Komaki, A. Yamada, D. Micic, A. Ido, and A. Sakuraba, “Risk of Cancers in Pediatric Inflammatory Bowel Diseases Patients: A Systematic Review and Meta-Analysis,” *J. Pediatr.*, Sep. 2020, doi: 10.1016/j.jpeds.2020.08.087.

[6] N. Ms, K. V, A.-A. Fa, K. Ma, and A. F, “Risk of colorectal cancer in inflammatory bowel diseases,” *Seminars in cancer biology*, Aug. 2020. https://pubmed.ncbi.nlm.nih.gov/31112753/ (accessed Oct. 03, 2020).

[7] P. Munkholm, “The incidence and prevalence of colorectal cancer in inflammatory bowel disease,” *Aliment. Pharmacol. Ther.*, vol. 18, pp. 1–5, 2003.

[8] C. C. Taylor, V. O. Millien, J. K. Hou, and N. N. Massarweh, “Association Between Inflammatory Bowel Disease and Colorectal Cancer Stage of Disease and Survival,” *J. Surg. Res.*, vol. 247, pp. 77–85, 2020, doi: 10.1016/j.jss.2019.10.040.

[9] Web4, “https://www.webmd.com/colorectal-cancer/ss/slideshow-colorectal-cancer-overview.” .

[10] L. A. Torre, F. Bray, R. L. Siegel, J. Ferlay, J. Lortet-Tieulent, and A. Jemal, “Global cancer statistics, 2012,” *CA. Cancer J. Clin.*, vol. 65, no. 2, pp. 87–108, 2015.

[11] C. Joachim *et al.*, “Trends in colorectal cancer in the Caribbean: A population-based study in Martinique, 1982–2011,” *Rev. Epidemiol. Sante Publique*, vol. 65, no. 3, pp. 181–188, 2017.

[12] R. Ahmed, K. Santhirakumar, H. Butt, and A. K. Yetisen, “Colonoscopy technologies for diagnostics and drug delivery,” *Med. DEVICES Sens.*, vol. 2, no. 3–4, p. e10041, 2019, doi: 10.1002/mds3.10041.

[13] S.-H. Lee, Y.-K. Park, D.-J. Lee, and K.-M. Kim, “Colonoscopy procedural skills and training for new beginners,” *World J. Gastroenterol. WJG*, vol. 20, no. 45, pp. 16984–16995, Dec. 2014, doi: 10.3748/wjg.v20.i45.16984.

[14] I. D. Nagtegaal, P. Quirke, and H.-J. Schmoll, “Has the new TNM classification for colorectal cancer improved care?,” *Nat. Rev. Clin. Oncol.*, vol. 9, no. 2, pp. 119–123, Feb. 2012, doi: 10.1038/nrclinonc.2011.157.

[15] C. Compton, D. Byrd, J. Garcia-Aguilar, S. Kurtzman, A. Olawaiye, and M. Washington, *AJCC Cancer Staging Atlas: A Companion to the Seventh Editions of the AJCC Cancer Staging Manual and Handbook*. 2012.

[16] J. B. O’Connell, M. A. Maggard, and C. Y. Ko, “Colon Cancer Survival Rates With the New American Joint Committee on Cancer Sixth Edition Staging,” *JNCI J. Natl. Cancer Inst.*, vol. 96, no. 19, pp. 1420–1425, Oct. 2004, doi: 10.1093/jnci/djh275.

[17] M. P. van der Paardt, F. M. Zijta, and J. Stoker, “MRI of the colon,” *Imaging Med.*, vol. 2, no. 2, pp. 195–209, Apr. 2010.

[18] Y. Mao *et al.*, “Diagnostic performance of magnetic resonance imaging for colorectal liver metastasis: A systematic review and meta-analysis,” *Sci. Rep.*, vol. 10, no. 1, p. 1969, Feb. 2020, doi: 10.1038/s41598-020-58855-1.

[19] N. Seo *et al.*, “Magnetic Resonance Imaging for Colorectal Cancer Metastasis to the Liver: Comparative Effectiveness Research for the Choice of Contrast Agents,” *Cancer Res. Treat. Off. J. Korean Cancer Assoc.*, vol. 50, no. 1, pp. 60–70, Jan. 2018, doi: 10.4143/crt.2016.533.

[20] P. A. Georgiou *et al.*, “Diagnostic accuracy and value of magnetic resonance imaging (MRI) in planning exenterative pelvic surgery for advanced colorectal cancer,” *Eur. J. Cancer Oxf. Engl. 1990*, vol. 49, no. 1, pp. 72–81, Jan. 2013, doi: 10.1016/j.ejca.2012.06.025.

[21] F. Bloch, “Nuclear Induction,” *Phys. Rev.*, vol. 70, no. 7–8, pp. 460–474, Oct. 1946, doi: 10.1103/PhysRev.70.460.

[22] E. M. Purcell, H. C. Torrey, and R. V. Pound, “Resonance Absorption by Nuclear Magnetic Moments in a Solid,” *Phys. Rev.*, vol. 69, no. 1–2, pp. 37–38, Jan. 1946, doi: 10.1103/PhysRev.69.37.

[23] M. A. Bernstein, K. F. King, and X. J. Zhou, *Handbook of MRI pulse sequences*. Elsevier, 2004.

[24] A. L. L. Kolkovsky, “1H and 31P NMR Spectroscopy for the study of brain metabolism at Ultra High Magnetic Field from Rodents to Men,” phdthesis, Université Paris Sud - Paris XI, 2015.

[25] J. Karkouri, “Exploiting sparse spectrum to accelerate spiral magnetic resonance spectroscopic imaging : method, simulation and applications to the functional exploration of skeletal muscle,” phdthesis, Université de Lyon, 2019.

[26] C. E. Hayes and L. Axel, “Noise performance of surface coils for magnetic resonance imaging at 1.5 T,” *Med. Phys.*, vol. 12, no. 5, pp. 604–607, Oct. 1985, doi: 10.1118/1.595682.

[27] J. Mispelter, M. Lupu, and A. Briguet, *NMR Probeheads for Biophysical and Biomedical Experiments: Theoretical Principles & Practical Guidelines*. Imperial College Press, 2006.

[28] M. Decorps, P. Blondet, H. Reutenauer, J. P. Albrand, and C. Remy, “An inductively coupled, series-tuned NMR probe,” *J. Magn. Reson. 1969*, vol. 65, no. 1, pp. 100–109, Oct. 1985, doi: 10.1016/0022-2364(85)90378-6.

[29] F. D. Doty, G. Entzminger, J. Kulkarni, K. Pamarthy, and J. P. Staab, “Radio frequency coil technology for small-animal MRI,” *NMR Biomed.*, vol. 20, no. 3, pp. 304–325, 2007, doi: 10.1002/nbm.1149.

[30] D. G. Gadian and F. N. H. Robinson, “Radiofrequency losses in NMR experiments on electrically conducting samples,” *J. Magn. Reson. 1969*, vol. 34, no. 2, pp. 449–455, May 1979, doi: 10.1016/0022-2364(79)90023-4.

[31] J. Murphy-Boesch and A. P. Koretsky, “An in Vivo NMR probe circuit for improved sensitivity,” *J. Magn. Reson. 1969*, vol. 54, no. 3, pp. 526–532, Oct. 1983, doi: 10.1016/0022-2364(83)90333-5.

[32] J.-M. Verret, “Apport d’un capteur endoluminal pour l’observation de la paroi colorectale par imagerie et spectrométrie de résonance magnétique,” These de doctorat, Lyon 1, 2014.

[33] D. M. Peterson, B. L. Beck, G. R. Duensing, and J. R. Fitzsimmons, “Common mode signal rejection methods for MRI: Reduction of cable shield currents for high static magnetic field systems,” *Concepts Magn. Reson. Part B Magn. Reson. Eng.*, vol. 19B, no. 1, pp. 1–8, 2003, doi: 10.1002/cmr.b.10090.
[34] B. M. Schaller, A. W. Magill, and R. Gruetter, “Common modes and cable traps,” in *Proc. Intl. Soc. Mag. Reson. Med*, 2011, vol. 19, p. 4660.
[35] C. Armenean, E. Perrin, M. Armenean, O. Beuf, F. Pilleul, and H. Saint-Jalmes, “RF-induced temperature elevation along metallic wires in clinical magnetic resonance imaging: influence of diameter and length,” *Magn. Reson. Med.*, vol. 52, no. 5, pp. 1200–1206, 2004.
[36] V. Detti, D. Grenier, E. Perrin, and O. Beuf, “Assessment of radiofrequency self-heating around a metallic wire with MR T1-based thermometry,” *Magn. Reson. Med.*, vol. 66, no. 2, pp. 448–455, Aug. 2011, doi: 10.1002/mrm.22834.
[37] R. Ayde *et al.*, “Potentialities of an Electro-Optic Crystal Fed by Nuclear Magnetic Resonant Coil for Remote and Low-Invasive Magnetic Field Characterization,” *IEEE Sens. J.*, vol. 13, no. 4, pp. 1274–1280, Apr. 2013, doi: 10.1109/JSEN.2012.2230623.
[38] N. Wr, O. A, R. W, M. C, L. M, and L. J, “On the heating of linear conductive structures as guide wires and catheters in interventional MRI.,” *J. Magn. Reson. Imaging Jmri*, vol. 13, no. 1, pp. 105–114, Jan. 2001, doi: 10.1002/1522-2586(200101)13:1<105::aid-jmri1016>3.0.co;2-0.
[39] M. Dempsey, B. Condon, and D. Hadley, “Investigation of the factors responsible for burns during MRI,” *J. Magn. Reson. Imaging*, vol. 13, pp. 627–631, Apr. 2001, doi: 10.1002/jmri.1088.
[40] M. E. Ladd and H. H. Quick, “Reduction of resonant RF heating in intravascular catheters using coaxial chokes,” *Magn. Reson. Med.*, vol. 43, no. 4, pp. 615–619, 2000, doi: 10.1002/(SICI)1522-2594(200004)43:4<615::AID-MRM19>3.0.CO;2-B.
[41] H. Barfuss *et al.*, “In vivo magnetic resonance imaging and spectroscopy of humans with a 4 T whole-body magnet,” *NMR Biomed.*, vol. 3, no. 1, pp. 31–45, Feb. 1990, doi: 10.1002/nbm.1940030106.
[42] B. L. Beck, D. M. Peterson, G. R. Duensing, and J. R. Fitzsimmons, “Implications of cable shield currents at 3.0 and 4.7 Tesla,” 2000.
[43] M. Meyerspeer, E. Serés Roig, R. Gruetter, and A. W. Magill, “An improved trap design for decoupling multinuclear RF coils,” *Magn. Reson. Med.*, vol. 72, no. 2, pp. 584–590, Aug. 2014, doi: 10.1002/mrm.24931.
[44] W. H. Harrison, M. Arakawa, and B. M. McCarten, “RF coil coupling for MRI with tuned RF rejection circuit using coax shield choke,” 1988, doi: 10.1016/0730-725X(88)90424-9.
[45] M. D. Schnall, R. E. Lenkinski, H. Y. Kressel, and H. M. Pollack, “Intracavity probe and interface device for MRI imaging and spectroscopy,” US5476095A, Dec. 19, 1995.
[46] K. Inui *et al.*, “Endoscopic MRI: preliminary results of a new technique for visualization and staging of gastrointestinal tumors,” *Endoscopy*, vol. 27, no. 7, pp. 480–485, Sep. 1995, doi: 10.1055/s-2007-1005752.
[47] M. Schnall, R. Lenkinski, H. Pollack, Y. Imai, and H. Kressel, “Prostate: MR Imaging with an endorectal surface coil,” *Radiology*, vol. 172, pp. 570–4, Sep. 1989, doi: 10.1148/radiology.172.2.2748842.
[48] M. D. Schnall and H. M. Pollack, “Magnetic resonance imaging of the prostate gland,” *Urol. Radiol.*, vol. 12, no. 1, pp. 109–114, Dec. 1990, doi: 10.1007/BF02923982.
[49] M. D. Schnall, Y. Imai, J. Tomaszewski, H. M. Pollack, R. E. Lenkinski, and H. Y. Kressel, “Prostate cancer: local staging with endorectal surface coil MR imaging,” *Radiology*, vol. 178, no. 3, pp. 797–802, Mar. 1991, doi: 10.1148/radiology.178.3.1994421.
[50] H. M. Pollack and M. D. Schnall, “Magnetic resonance imaging in carcinoma of the prostate,” *Prostate. Suppl.*, vol. 4, pp. 17–31, 1992, doi: 10.1002/pros.2990210505.
[51] M. Armenean, O. Beuf, F. Pilleul, and H. Saint-Jalmes, “Endoluminal loop radiofrequency coils for gastrointestinal wall imaging,” Feb. 2001, vol. 3, pp. 3052–3055 vol.3, doi: 10.1109/IEMBS.2001.1017444.
[52] C. Maldjian, R. Smith, A. Kilger, M. Schnall, G. Ginsberg, and M. Kochman, “Endorectal surface coil MR imaging as a staging technique for rectal carcinoma: a comparison study to rectal endosonography,” *Abdom. Imaging*, vol. 25, no. 1, pp. 75–80, Feb. 2000, doi: 10.1007/s002619910015.
[53] C. Meyenberger, R. A. Huch Böni, P. Bertschinger, G. F. Zala, H. P. Klotz, and G. P. Krestin, “Endoscopic ultrasound and endorectal magnetic resonance imaging: a prospective, comparative study for preoperative staging and follow-up of rectal cancer,” *Endoscopy*, vol. 27, no. 7, pp. 469–479, Sep. 1995, doi: 10.1055/s-2007-1005751.
[54] G. F. Gualdi, E. Casciani, A. Guadalaxara, C. d’Orta, E. Polettini, and G. Pappalardo, “Local staging of rectal cancer with transrectal ultrasound and endorectal magnetic resonance imaging: comparison with histologic findings,” *Dis. Colon Rectum*, vol. 43, no. 3, pp. 338–345, Mar. 2000, doi: 10.1007/bf02258299.
[55] P. Torricelli, S. Lo Russo, A. Pecchi, G. Luppi, A. M. Cesinaro, and R. Romagnoli, “Endorectal coil MRI in local staging of rectal cancer,” *Radiol. Med. (Torino)*, vol. 103, no. 1–2, pp. 74–83, Feb. 2002.
[56] D. J. Dinter, R.-D. Hofheinz, M. Hartel, G. F. A. B. Kaehler, W. Neff, and S. J. Diehl, “Preoperative staging of rectal tumors: comparison of endorectal ultrasound, hydro-CT, and high-resolution endorectal MRI,” *Onkologie*, vol. 31, no. 5, pp. 230–235, May 2008, doi: 10.1159/000121359.
[57] H. Kwok, I. P. Bissett, and G. L. Hill, “Preoperative staging of rectal cancer,” *Int. J. Colorectal Dis.*, vol. 15, no. 1, pp. 9–20, Feb. 2000, doi: 10.1007/s003840050002.
[58] J.-M. Verret *et al.*, “Characterization of a dedicated double loop, endoluminal coil for anal sphincter MR imaging at 1.5 T and 3 T,” *Concepts Magn. Reson. Part B Magn. Reson. Eng.*, vol. 44, no. 2, pp. 39–49, Apr. 2014, doi: 10.1002/cmr.b.21265.
[59] A. Ramgolam, R. Sablong, L. Lafarge, H. Saint-Jalmes, and O. Beuf, “Optical spectroscopy combined with high-resolution magnetic resonance imaging for digestive wall assessment: endoluminal bimodal probe conception and characterization in vitro, on organic sample and in vivo on a rabbit,” *J. Biomed. Opt.*, vol. 16, no. 11, p. 117005, Nov. 2011, doi: 10.1117/1.3646917.

[60] F. Pilleul *et al.*, “High-resolution MR imaging appearance of colonic tissue in rabbits using an endoluminal coil,” *Magn. Reson. Mater. Phys. Biol. Med.*, vol. 18, no. 5, pp. 238–244, Oct. 2005, doi: 10.1007/s10334-005-0008-9.
[61] H. H. Quick *et al.*, “Single-loop coil concepts for intravascular magnetic resonance imaging,” *Magn. Reson. Med.*, vol. 41, no. 4, pp. 751–758, Apr. 1999, doi: 10.1002/(sici)1522-2594(199904)41:4<751::aid-mrm14>3.0.co;2-v.
[62] H. H. Quick, M. E. Ladd, P. R. Hilfiker, G. G. Paul, S. W. Ha, and J. F. Debatin, “Autoperfused balloon catheter for intravascular MR imaging,” *J. Magn. Reson. Imaging JMRI*, vol. 9, no. 3, pp. 428–434, Mar. 1999, doi: 10.1002/(sici)1522-2586(199903)9:3<428::aid-jmri10>3.0.co;2-e.
[63] S. B. Bulumulla, K. J. Park, E. Fiveland, J. Iannotti, and F. Robb, “MEMS switch integrated radio frequency coils and arrays for magnetic resonance imaging,” *Rev. Sci. Instrum.*, vol. 88, no. 2, p. 025003, Feb. 2017, doi: 10.1063/1.4975181.
[64] F. Maggiorelli *et al.*, “Double-Tuned Surface 1H–23Na Radio Frequency Coils at 7 T: Comparison of Three Decoupling Methods,” *Appl. Magn. Reson.*, Feb. 2019, doi: 10.1007/s00723-019-01116-w.
[65] A. Maunder, M. Rao, F. Robb, and J. M. Wild, “Comparison of MEMS switches and PIN diodes for switched dual tuned RF coils,” *Magn. Reson. Med.*, vol. 80, no. 4, pp. 1746–1753, 2018, doi: 10.1002/mrm.27156.
[66] D. Darnell, Y. Ma, H. Wang, F. Robb, A. W. Song, and T.-K. Truong, “Adaptive integrated parallel reception, excitation, and shimming (iPRES-A) with microelectromechanical systems switches,” *Magn. Reson. Med.*, vol. 80, no. 1, pp. 371–379, 2018, doi: 10.1002/mrm.27007.
[67] K. Byron, S. A. Winkler, F. Robb, S. Vasanawala, J. Pauly, and G. Scott, “An MRI Compatible RF MEMs Controlled Wireless Power Transfer System,” *IEEE Trans. Microw. Theory Tech.*, vol. 67, no. 5, pp. 1717–1726, May 2019, doi: 10.1109/TMTT.2019.2902554.
[68] D. Spence and M. Aimi, “Custom MEMS switch for MR surface coil decoupling,” in *Proceedings of the 23rd Annual Meeting of ISMRM, Toronto, Canada*, 2015, p. 0704.
[69] C. Keimel, G. Claydon, B. Li, J. Park, and M. E. Valdes, “Micro-Electromechanical-System (MEMS) based switches for power applications,” in *2011 IEEE Industrial and Commercial Power Systems Technical Conference*, May 2011, pp. 1–8, doi: 10.1109/ICPS.2011.5890885.
[70] J. Libove and J. Singer, “Resolution and Signal-to-Noise Relationships in NMR Imaging in the Human Body,” *J. Phys. [E]*, vol. 13, pp. 38–44, Feb. 1980, doi: 10.1088/0022-3735/13/1/013.
[71] G. McGibney and M. R. Smith, “An unbiased signal-to-noise ratio measure for magnetic resonance images,” *Med. Phys.*, vol. 20, no. 4, pp. 1077–1078, Aug. 1993, doi: 10.1118/1.597004.
[72] B. W. Murphy, P. L. Carson, J. H. Ellis, Y. T. Zhang, R. J. Hyde, and T. L. Chenevert, “Signal-to-noise measures for magnetic resonance imagers,” *Magn. Reson. Imaging*, vol. 11, no. 3, pp. 425–428, 1993, doi: 10.1016/0730-725x(93)90076-p.
[73] D. I. Hoult and R. E. Richards, “The signal-to-noise ratio of the nuclear magnetic resonance experiment,” *J. Magn. Reson. 1969*, vol. 24, no. 1, pp. 71–85, Oct. 1976, doi: 10.1016/0022-2364(76)90233-X.
[74] G. Giovannetti, “Multiturn surface coil: Theoretical considerations on unloaded to loaded Q ratio and SNR,” *Concepts Magn. Reson. Part B Magn. Reson. Eng.*, vol. 44, no. 2, pp. 27–31, 2014, doi: 10.1002/cmr.b.21259.
[75] S. M. Wright and L. L. Wald, “Theory and application of array coils in MR spectroscopy,” *NMR Biomed.*, vol. 10, no. 8, pp. 394–410, Dec. 1997, doi: 10.1002/(SICI)1099-1492(199712)10:8<394::AID-NBM494>3.0.CO;2-0.
[76] D. I. Hoult and P. C. Lauterbur, “The sensitivity of the zeugmatographic experiment involving human samples,” *J. Magn. Reson. 1969*, vol. 34, no. 2, pp. 425–433, May 1979, doi: 10.1016/0022-2364(79)90019-2.
[77] G. C. Hurst, J. Hua, J. L. Duerk, and A. M. Cohen, “Intravascular (catheter) NMR receiver probe: Preliminary design analysis and application to canine iliofemoral imaging,” *Magn. Reson. Med.*, vol. 24, no. 2, pp. 343–357, 1992, doi: 10.1002/mrm.1910240215.
[78] J.-M. Jin, *The Finite Element Method in Electromagnetics*. John Wiley & Sons, 2015.
[79] A. Taflove and S. C. Hagness, “Computational electrodynamics : the finite-difference time-domain method,” *CERN Document Server*, 2005. https://cds.cern.ch/record/1698084 (accessed Jun. 29, 2020).
[80] Kane Yee, “Numerical solution of initial boundary value problems involving maxwell’s equations in isotropic media,” *IEEE Trans. Antennas Propag.*, vol. 14, no. 3, pp. 302–307, May 1966, doi: 10.1109/TAP.1966.1138693.
[81] R. F. Harrington, *Field Computation by Moment Methods*. Wiley-IEEE Press, 1993.
[82] W. C. Gibson, *The method of moments in electromagnetics*. Boca Raton: Chapman & Hall/CRC, 2008.
[83] B. K. Li, B. Xu, F. Liu, H. T. Hui, and S. Crozier, “High frequency electromagnetic analysis using hybrid MoM/FEM method,” in *Proceedings 14th Scientific Meeting, International Society for Magnetic Resonance in Medicine*, 2006, p. 699.
[84] B. K. Li, F. Liu, E. Weber, and S. Crozier, “Hybrid numerical techniques for the modelling of radiofrequency coils in MRI,” *NMR Biomed.*, vol. 22, no. 9, pp. 937–951, Nov. 2009, doi: 10.1002/nbm.1344.
[85] T. S. Ibrahim, R. Lee, B. A. Baertlein, Y. Yu, and P. M. Robitaille, “Computational analysis of the high pass birdcage resonator: finite difference time domain simulations for high-field MRI,” *Magn. Reson. Imaging*, vol. 18, no. 7, pp. 835–843, Sep. 2000, doi: 10.1016/s0730-725x(00)00161-2.
[86] A. Taflove, “Application of the Finite-Difference Time-Domain Method to Sinusoidal Steady-State Electromagnetic-Penetration Problems,” *IEEE Trans. Electromagn. Compat.*, vol. EMC-22, no. 3, pp. 191–202, Aug. 1980, doi: 10.1109/TEMC.1980.303879.
[87] A. Taflove and M. E. Brodwin, “Numerical Solution of Steady-State Electromagnetic Scattering Problems Using the Time-Dependent Maxwell’s Equations,” *IEEE Trans. Microw. Theory Tech.*, vol. 23, no. 8, pp. 623–630, Aug. 1975, doi: 10.1109/TMTT.1975.1128640.
[88] J. Vincent, “Modélisation d’antennes basses fréquences en présence de sol et d’environnements réalistes,” 2015.
[89] R. Stara *et al.*, “RF coil design for low and high field MRI: Numerical methods and measurements,” in *2011 IEEE Nuclear Science Symposium Conference Record*, Oct. 2011, pp. 3465–3469, doi: 10.1109/NSSMIC.2011.6152634.
[90] A. C. Polycarpou, *Introduction to the Finite Element Method in Electromagnetics*. Morgan & Claypool, 2006.

[91] C. Guclu, G. Kashmar, A. Hacinliyan, and O. Nalcioglu, “An FEM approach for the characterization of the RF field homogeneity at high field,” *Magn. Reson. Med.*, vol. 37, no. 1, pp. 76–83, Jan. 1997, doi: 10.1002/mrm.1910370112.
[92] “(2) (PDF) Fast Solvers For Integral-Equation Based Electromagnetic Simulations,” *ResearchGate*. https://www.researchgate.net/publication/326684162_Fast_Solvers_For_Integral-Equation_Based_Electromagnetic_Simulations (accessed Jun. 28, 2020).
[93] F. Liu, B. L. Beck, B. Xu, J. R. Fitzsimmons, S. J. Blackband, and S. Crozier, “Numerical modeling of 11.1T MRI of a human head using a MoM/FDTD method,” *Concepts Magn. Reson. Part B Magn. Reson. Eng.*, vol. 24B, no. 1, pp. 28–38, 2005, doi: 10.1002/cmr.b.20024.
[94] G. Chatterjee, A. Das, and D. Gope, “Learning-Based Fast Iterative Convergence of 3-D MoM via Eigen-AGMRES Method,” *IEEE Trans. Antennas Propag.*, vol. 63, no. 12, pp. 5889–5893, Dec. 2015, doi: 10.1109/TAP.2015.2481478.
[95] G. Chatterjee, A. Das, S. R. Vedicherla, and D. Gope, “Mesh Interpolated Krylov Recycling Method to Expedite 3-D Full-Wave MoM Solution for Design Variants,” *IEEE Trans. Microw. Theory Tech.*, vol. 65, no. 9, pp. 3159–3171, Sep. 2017, doi: 10.1109/TMTT.2017.2682059.
[96] A. Das, R. R. Nair, and D. Gope, “Efficient adaptive mesh refinement for MoM-based package-board 3D full-wave extraction,” in *2013 IEEE 22nd Conference on Electrical Performance of Electronic Packaging and Systems*, Oct. 2013, pp. 239–242, doi: 10.1109/EPEPS.2013.6703508.
[97] G. Chatterjee, A. Das, and D. Gope, “Fast convergence of MoM-based package-board extraction via incremental eigen-AGMRES method,” in *2014 IEEE 23rd Conference on Electrical Performance of Electronic Packaging and Systems*, Oct. 2014, pp. 151–154, doi: 10.1109/EPEPS.2014.7103620.
[98] G. Green, “An Essay on the Application of mathematical Analysis to the theories of Electricity and Magnetism,” *ArXiv08070088 Phys.*, Jul. 2008, Accessed: Jun. 29, 2020. [Online]. Available: http://arxiv.org/abs/0807.0088.
[99] J. Jin, *Electromagnetic analysis and design in magnetic resonance imaging*. Boca Raton, FL: CRC Press, 1999.
[100] F. Meyer, D. B. Davidson, U. Jakobus, and M. A. Stuchly, “Human exposure assessment in the near field of GSM base-station antennas using a hybrid finite element/method of moments technique,” *IEEE Trans. Biomed. Eng.*, vol. 50, no. 2, pp. 224–233, Feb. 2003, doi: 10.1109/TBME.2002.807639.
[101] M. W. Ali, T. H. Hubing, and J. L. Dreniak, “A hybrid FEM/MOM technique for electromagnetic scattering and radiation from dielectric objects with attached wires,” *IEEE Trans. Electromagn. Compat.*, vol. 39, no. 4, pp. 304–314, Nov. 1997, doi: 10.1109/15.649818.
[102] K. Minard and R. Wind, “Solenoidal microcoil design—Part II: Optimizing winding parameters for maximum signal-to-noise performance,” *Concepts Magn. Reson.*, vol. 13, pp. 190–210, Jan. 2001, doi: 10.1002/cmr.1008.
[103] O. Ocali and E. Atalar, “Ultimate intrinsic signal-to-noise ratio in MRI,” *Magn. Reson. Med.*, vol. 39, no. 3, pp. 462–473, Mar. 1998, doi: 10.1002/mrm.1910390317.
[104] T. L. Peck, R. L. Magin, and P. C. Lauterbur, “Design and Analysis of Microcoils for NMR Microscopy,” *J. Magn. Reson. B*, vol. 108, no. 2, pp. 114–124, Aug. 1995, doi: 10.1006/jmrb.1995.1112.
[105] M. Armenean, “Spectroscopie et imagerie de faibles volumes par RMN : conception et optimisation de capteurs radiofréquence implantables et endoluminaux,” These de doctorat, Lyon 1, 2002.
[106] M. Armenean, O. Beuf, F. Pilleul, and H. Saint-Jalmes, “Optimization of endoluminal loop radiofrequency coils for gastrointestinal wall MR imaging,” *IEEE Sens. J.*, vol. 4, no. 1, pp. 57–64, Feb. 2004, doi: 10.1109/JSEN.2003.820334.
[107] G. Giovannetti, V. Hartwig, L. Landini, and M. F. Santarelli, “Low-Field MR Coils: Comparison between Strip and Wire Conductors,” *Appl. Magn. Reson.*, vol. 39, no. 4, pp. 391–399, Dec. 2010, doi: 10.1007/s00723-010-0173-5.
[108] P. A. Bottomley, “A technique for the measurement of tissue impedance from 1 to 100 MHz using a vector impedance meter,” *J. Phys. [E]*, vol. 11, no. 5, pp. 413–414, May 1978, doi: 10.1088/0022-3735/11/5/012.
[109] L. Rusiniak, “Electric properties of water. New experimental data in the 5 HZ - 13 MHZ frequency range,” *Acta Geophys. Pol.*, vol. 52, Jan. 2004.
[110] Jianmin Wang, A. Reykowski, and J. Dickas, “Calculation of the signal-to-noise ratio for simple surface coils and arrays of coils [magnetic resonance imaging],” *IEEE Trans. Biomed. Eng.*, vol. 42, no. 9, pp. 908–917, Sep. 1995, doi: 10.1109/10.412657.
[111] P. Pimmel, “Les antennes en résonance magnétique nucléaire : fonctionnement et réalisation : résonateurs pour l’imagerie et pour la spectroscopie in vivo,” thesis, Lyon 1, 1990.
[112] R. A. Lemdiasov, A. A. Obi, and R. Ludwig, “A numerical postprocessing procedure for analyzing radio frequency MRI coils,” *Concepts Magn. Reson. Part A*, vol. 38A, no. 4, pp. 133–147, 2011, doi: 10.1002/cmr.a.20217.
[113] T. L. Peck, R. L. Magin, J. Kruse, and M. Feng, “NMR microspectroscopy using 100 microns planar RF coils fabricated on gallium arsenide substrates,” *IEEE Trans. Biomed. Eng.*, vol. 41, no. 7, pp. 706–709, Jul. 1994, doi: 10.1109/10.301740.
[114] A. C. Wright, H. K. Song, and F. W. Wehrli, “In vivo MR micro imaging with conventional radiofrequency coils cooled to 77 degrees K,” *Magn. Reson. Med.*, vol. 43, no. 2, pp. 163–169, Feb. 2000, doi: 10.1002/(sici)1522-2594(200002)43:2<163::aid-mrm1>3.0.co;2-k.
[115] J. Ferlay *et al.*, “Estimating the global cancer incidence and mortality in 2018: GLOBOCAN sources and methods,” *Int. J. Cancer*, vol. 144, no. 8, pp. 1941–1953, 2019, doi: 10.1002/ijc.31937.
[116] X. V. Qadir, M. Clyne, T. K. Lam, M. J. Khoury, and S. D. Schully, “Trends in published meta-analyses in cancer research, 2008–2013,” *Cancer Causes Control*, vol. 28, no. 1, pp. 5–12, 2017.
[117] A.-M. Bouvier, “Epidémiologie descriptive du cancer colorectal en France,” *BEH Thématique*, vol. 13, 2009.
[118] P. B. Roemer, W. A. Edelstein, C. E. Hayes, S. P. Souza, and O. M. Mueller, “The NMR phased array,” *Magn. Reson. Med.*, vol. 16, no. 2, pp. 192–225, Nov. 1990, doi: 10.1002/mrm.1910160203.

[119] A. Perrier *et al.*, “Design of a Four-Channel Surface Receiver Coil Array Without Preamplifiers for the Decoupling Between Elements: Validation for High-Resolution Rat Knee MR Imaging,” *IEEE Sens. J.*, vol. 13, no. 6, pp. 2450–2458, Jun. 2013, doi: 10.1109/JSEN.2013.2254894.
[120] A. Perrier *et al.*, “Design of a Two-Channel NMR Coil Using an Impedance Transformation Approach,” *IEEE Sens. J.*, vol. 12, no. 6, pp. 1801–1808, Jun. 2012, doi: 10.1109/JSEN.2011.2178237.
[121] D. J. Gilderdale *et al.*, “Design and use of internal receiver coils for magnetic resonance imaging.,” *Br. J. Radiol.*, vol. 72, no. 864, pp. 1141–1151, 1999.
[122] E. Atalar *et al.*, “High resolution intravascular MRI and MRS by using a catheter receiver coil,” *Magn. Reson. Med.*, vol. 36, no. 4, pp. 596–605, Oct. 1996, doi: 10.1002/mrm.1910360415.
[123] O. Beuf, F. Pilleul, M. Armenean, G. Hadour, and H. Saint-Jalmes, “In vivo colon wall imaging using endoluminal coils: Feasibility study on rabbits,” *J. Magn. Reson. Imaging JMRI*, vol. 20, pp. 90–6, Jul. 2004, doi: 10.1002/jmri.20059.
[124] H. Dorez *et al.*, “Endoluminal high-resolution MR imaging protocol for colon walls analysis in a mouse model of colitis,” *Magn. Reson. Mater. Phys. Biol. Med.*, vol. 29, no. 4, pp. 657–669, Aug. 2016, doi: 10.1007/s10334-016-0539-2.
[125] H. Dorez *et al.*, “In vivo MRS for the assessment of mouse colon using a dedicated endorectal coil: initial findings,” *NMR Biomed.*, vol. 30, no. 12, p. e3794, 2017.
[126] W. A. Edelstein, C. J. Hardy, and O. M. Mueller, “Electronic decoupling of surface-coil receivers for NMR imaging and spectroscopy,” *J. Magn. Reson. 1969*, vol. 67, no. 1, pp. 156–161, Mar. 1986, doi: 10.1016/0022-2364(86)90421-X.
[127] A. Reykowski, “Using memristor devices as switches for MRI RF coils,” US9417299B2, Aug. 16, 2016.
[128] E. Wong, Q. Zhang, J. Duerk, J. Lewin, and M. Wendt, “An optical system for wireless detuning of parallel resonant circuits,” *J. Magn. Reson. Imaging JMRI*, vol. 12, pp. 632–8, Nov. 2000, doi: 10.1002/1522-2586(200010)12:4<632::AID-JMRI17>3.0.CO;2-J.
[129] S. Weiss *et al.*, “In vivo safe catheter visualization and slice tracking using an optically detunable resonant marker,” *Magn. Reson. Med.*, vol. 52, no. 4, pp. 860–868, 2004, doi: 10.1002/mrm.20214.
[130] H. Eggers, S. Weiss, P. Boernert, and P. Boesiger, “Image-based tracking of optically detunable parallel resonant circuits,” *Magn. Reson. Med.*, vol. 49, no. 6, pp. 1163–1174, 2003, doi: 10.1002/mrm.10459.
[131] I. Saniour *et al.*, “Active optical-based detuning circuit for receiver endoluminal coil,” *Biomed. Phys. Eng. Express*, vol. 3, no. 2, p. 025002, 2017, doi: 10.1088/2057-1976/aa5db0.
[132] S. Rescia and S. Smith, “RECEIVE-ONLY SURFACE COIL ‘WITH IMPROVED DETUNTNG FOR PRE-CLINICAL MR1 STUDIES,” Brookhaven National Laboratory (BNL), 2013.
[133] P.-J. Nacher, S. Kumaragamage, G. Tastevin, and C. P. Bidinosti, “A fast MOSFET rf switch for low-field NMR and MRI,” *J. Magn. Reson.*, vol. 310, p. 106638, Jan. 2020, doi: 10.1016/j.jmr.2019.106638.
[134] H. Fujita, T. Zheng, X. Yang, M. J. Finnerty, and S. Handa, “RF Surface Receive Array Coils: The Art of an LC Circuit,” *J. Magn. Reson. Imaging*, vol. 38, no. 1, pp. 12–25, 2013, doi: 10.1002/jmri.24159.
[135] V. Taracila, K. Shet, and F. Robb, “Preamp decoupling-eigenvalue solution approach,” *channels*, vol. 1, p. 1, 2008.
[136] C. C. Guclu, E. Boskamp, T. Zheng, R. Becerra, and L. Blawat, “A method for preamplifier-decoupling improvement in quadrature phased-array coils,” *J. Magn. Reson. Imaging*, vol. 19, no. 2, pp. 255–258, 2004, doi: 10.1002/jmri.10449.
[137] H. Raki, K. Tse-Ve-Koon, H. Souchay, F. Robb, S. Lambert, and O. Beuf, “Design of a reconfigurable endoluminal coil using MEMS switches,” Montréal, Canada, May 2019, Accessed: Sep. 17, 2019. [Online]. Available: https://hal.archives-ouvertes.fr/hal-02266838.
[138] C. Keimel, G. Claydon, B. Li, J. N. Park, and M. E. Valdes, “Microelectromechanical-Systems-Based Switches for Power Applications,” *IEEE Trans. Ind. Appl.*, vol. 48, no. 4, pp. 1163–1169, Jul. 2012, doi: 10.1109/TIA.2012.2199949.
[139] D. Kajfez, “Q factor measurements, analog and digital,” *Univ. Miss. Dept Electr. Eng. Www Ee Olemiss Eduldarkorfqmeas2b Pdf*, 1999.
[140] W. P. Wheless and D. Kajfez, “Experimental Characterization of Multimode Microwave Resonators Using Automated Network Analyzer,” *IEEE Trans. Microw. Theory Tech.*, vol. 35, no. 12, pp. 1263–1270, Dec. 1987, doi: 10.1109/TMTT.1987.1133846.
[141] D. Kajfez and E. J. Hwan, “Q-Factor Measurement with Network Analyzer,” *IEEE Trans. Microw. Theory Tech.*, vol. 32, no. 7, pp. 666–670, Jul. 1984, doi: 10.1109/TMTT.1984.1132751.
[142] M. A. Griswold, “Characterization of Multichannel Coil Arrays on the Benchtop,” in *eMagRes*, American Cancer Society, 2012.
[143] E. Der, V. Volotovskyy, H. Sun, B. Tomanek, and J. C. Sharp, “Design of a high power PIN-diode controlled switchable RF transmit array for TRASE RF imaging,” *Concepts Magn. Reson. Part B Magn. Reson. Eng.*, vol. 48B, no. 1, Feb. 2018, doi: 10.1002/cmr.b.21365.
[144] G. Giovannetti, V. Hartwig, L. Landini, and M. F. Santarelli, “Sample-Induced Resistance Estimation in Magnetic Resonance Experiments: Simulation and Comparison of Two Methods,” *Appl. Magn. Reson.*, vol. 40, no. 3, pp. 351–361, May 2011, doi: 10.1007/s00723-011-0210-z.
[145] R. W. Geenen, S. M. Hussain, P. D. Siersema, and J.-W. Poley, “Current status of MRI in patients with inflammatory bowel disease colitis,” *Appl. Radiol.*, vol. 36, no. 2, p. 10, 2007.
[146] L. Quettier *et al.*, “Expected magnetic field quality from the preliminary measurements performed during the manufacturing of the Iseult/INUMAC whole-body 11.7-T MRI magnet,” *IEEE Trans. Appl. Supercond.*, vol. 26, no. 4, pp. 1–4, 2016.
[147] H. E. Adamek, H. Breer, T. Karschkes, J. Albert, and J. F. Riemann, “Magnetic resonance imaging in gastroenterology: time to say good-bye to all that endoscopy?,” *Endoscopy*, vol. 32, no. 05, pp. 406–410, 2000.
[148] M. V. Kulkarni, J. A. Patton, and R. R. Price, “Technical considerations for the use of surface coils in MRI,” *Am. J. Roentgenol.*, vol. 147, no. 2, pp. 373–378, 1986.

[149] R. Gabbay-Benziv *et al.*, “A step-wise approach for analysis of the mouse embryonic heart using 17.6 Tesla MRI,” *Magn. Reson. Imaging*, vol. 35, pp. 46–53, 2017.
[150] D. Nespor, K. Bartusek, and Z. Dokoupil, “Comparing Saddle, Slotted-tube and Parallel-plate Coils for Magnetic Resonance Imaging,” *Meas. Sci. Rev.*, vol. 14, Jun. 2014, doi: 10.2478/msr-2014-0023.
[151] “96-Channel receive-only head coil for 3 Tesla: Design optimization and evaluation - Wiggins - 2009 - Magnetic Resonance in Medicine - Wiley Online Library.” https://onlinelibrary.wiley.com/doi/abs/10.1002/mrm.22028 (accessed Sep. 10, 2018).
[152] G. J. Metzger *et al.*, “Performance of external and internal coil configurations for prostate investigations at 7 T,” *Magn. Reson. Med.*, vol. 64, no. 6, pp. 1625–1639, 2010.
[153] S. Giusti *et al.*, “Preoperative rectal cancer staging with phased-array MR,” *Radiat. Oncol.*, vol. 7, no. 1, p. 29, 2012.
[154] I. Saniour, J.-M. Verret, C. Rabrait-Lerman, F. Pilleul, and O. Beuf, “Feasibility and characterization of a safe susceptibility-matched endorectal coil for MR spectroscopy,” *NMR Biomed.*, vol. 33, no. 11, p. e4384, 2020, doi: 10.1002/nbm.4384.
[155] E. Atalar *et al.*, “High resolution intravascular MRI and MRS by using a catheter receiver coil,” *Magn. Reson. Med.*, vol. 36, no. 4, pp. 596–605, 1996.
[156] R. W. Jones and R. J. Witte, “Signal intensity artifacts in clinical MR imaging,” *Radiogr. Rev. Publ. Radiol. Soc. N. Am. Inc*, vol. 20, no. 3, pp. 893–901, Jun. 2000, doi: 10.1148/radiographics.20.3.g00ma19893.
[157] B. R. Condon, J. Patterson, D. Wyper, A. Jenkins, and D. M. Hadley, “Image non-uniformity in magnetic resonance imaging: its magnitude and methods for its correction,” *Br. J. Radiol.*, vol. 60, no. 709, pp. 83–87, 1987.
[158] O. Beuf, F. Pilleul, M. Armenean, G. Hadour, and H. Saint-Jalmes, “In vivo colon wall imaging using endoluminal coils: Feasibility study on rabbits,” *J. Magn. Reson. Imaging*, vol. 20, no. 1, pp. 90–96, Jul. 2004, doi: 10.1002/jmri.20059.
[159] A. Simmons, P. S. Tofts, G. J. Barker, and S. R. Arridge, “Sources of intensity nonuniformity in spin echo images at 1.5 T,” *Magn. Reson. Med.*, vol. 32, no. 1, pp. 121–128, 1994.
[160] S. E. Moyher, D. B. Vigneron, and S. J. Nelson, “Surface coil MR imaging of the human brain with an analytic reception profile correction,” *J. Magn. Reson. Imaging JMRI*, vol. 5, no. 2, pp. 139–144, Apr. 1995.
[161] U. Vovk, F. Pernus, and B. Likar, “A Review of Methods for Correction of Intensity Inhomogeneity in MRI,” *IEEE Trans. Med. Imaging*, vol. 26, no. 3, pp. 405–421, Mar. 2007, doi: 10.1109/TMI.2006.891486.
[162] T. Kuehne, R. Fahrig, and K. Butts, “Pair of resonant fiducial markers for localization of endovascular catheters at all catheter orientations,” *J. Magn. Reson. Imaging Off. J. Int. Soc. Magn. Reson. Med.*, vol. 17, no. 5, pp. 620–624, 2003.
[163] M. Fuentes, E. Weber, S. Wilson, B. Li, and S. Crozier, “Micro-Electromechanical Systems (MEMS) based RF-switches in MRI–a performance study,” 2010.
[164] H. Raki *et al.*, “Serial and Parallel Active Decoupling Characterization Using RF MEMS Switches for Receiver Endoluminal Coils at 1.5T,” *IEEE Sens. J.*, pp. 1–1, 2020, doi: 10.1109/JSEN.2020.2995055.
[165] Feko software, “Electromagnetic Simulation Software | Altair Feko.” https://altairhyperworks.com/product/FEKO (accessed Jun. 24, 2020).
[166] J.-J. Chung, R. C. Semelka, D. R. Martin, and H. B. Marcos, “Colon diseases: MR evaluation using combined T2-weighted single-shot echo train spin-echo and gadolinium-enhanced spoiled gradient-echo sequences,” *J. Magn. Reson. Imaging*, vol. 12, no. 2, pp. 297–305, Aug. 2000, doi: 10.1002/1522-2586(200008)12:2<297::AID-JMRI12>3.0.CO;2-Q.
[167] colon:, “Dielectric Properties of Body Tissues: Home page.” http://niremf.ifac.cnr.it/tissprop/ (accessed Jun. 25, 2020).
[168] H. Raki *et al.*, “Serial and Parallel Active Decoupling Characterization Using RF MEMS Switches for Receiver Endoluminal Coils at 1.5 T,” *IEEE Sens. J.*, vol. 20, no. 18, pp. 10511–10520, Sep. 2020, doi: 10.1109/JSEN.2020.2995055.
[169] C. Andrade, M. Otaduy, E. Park, and C. Leite, “Phosphorus-31 MR spectroscopy of the human brain: Technical aspects and biomedical applications,” *Int. J. Curr. Res. Rev.*, vol. 6, pp. 41–57, May 2014.
[170] C. Menuel *et al.*, “[Phosphorus magnetic resonance spectroscopy: Brain pathologies applications],” *J. Neuroradiol. J. Neuroradiol.*, vol. 37, no. 2, pp. 73–82, May 2010, doi: 10.1016/j.neurad.2009.07.001.